TECHNISCHE UNIVERSITÄT MÜNCHEN
Max-Planck-Institut für extraterrestrische Physik

Applying the Fireball Model to Short Gamma-Ray Burst Afterglows: Methods, Jet Opening Angles and Plateau Phases

Fabian Knust

Vollständiger Abdruck der von der Fakultät für Physik der Technischen Universität München zur Erlangung des akademischen Grades eines

Doktors der Naturwissenschaften (Dr. rer. nat.)

genehmigten Dissertation.

Vorsitzender: Univ.-Prof. Dr. Alejandro Ibarra

Prüfer der Dissertation: 1. Priv.-Doz. Dr. Jochen Greiner
2. Univ.-Prof. Dr. Lothar Oberauer

Die Dissertation wurde am 13.04.17 bei der Technischen Universität München eingereicht und durch die Fakultät für Physik am 30.05.17 angenommen.

CONTENTS

ABSTRACT

Gamma Ray Bursts (GRBs) are among the most luminous explosions in the Universe. They are named after their second-long prompt γ-ray emission, which is followed by a long lasting broad-band emission called afterglow. There are at least two distinct classes of GRBs, separated by the length and spectral hardness of their prompt emission: short hard GRBs and long soft GRBs. Short GRBs are believed to be the result of a two merging neutron stars, or a merger between a neutron star and a black hole. Long GRBs are the result of the collapse of a massive star. GRBs have been observed up to very high redshifts, and serve as an excellent probe of the early Universe. Moreover, GRBs allow us to test our understanding of physics under extreme conditions.

The basic observational features of GRB afterglows seem to be the same for long and short GRBs, and are very successfully explained by the *fireball model*. The model describes the afterglow as synchrotron emission from the shock that occurs when an ultra-relativistic jetted outflow hits the circum-burst medium. There are multiple ways to implement the fireball model; The different implementations are based on different physical assumptions, e.g. the exact structure of the jet, or the temporal profile of the energy that is injected into the outflow. Also different approximations are used e.g. treating the fireball expansion as an adiabatic process, or assuming that despite the deceleration of the blast wave one always stays in an ultra-relativistic regime. Additionally to the numerous analytical models, numerical simulations became feasible during the last decade. As a results of this manifold of implementations, the exact values of the model parameters are uncertain.

In this thesis, I will apply the fireball model to GRB afterglows. First, I compare different analysis methods and implementations of the model, using data of the "textbook" afterglow of GRB 081121A. Afterwards, I apply a model based on hydro-dynamical simulations to a sample of short-duration GRB afterglows. Finally, I analyze data of the particularly interesting GRB 150424A, a short GRB

with extended emission and a long optical plateau phase.

My results can be summarized as follows: 1.) Applying different approaches to GRB 081121A shows how strongly the result of an analysis depends on the exact implementation of the fireball model and the completeness of the data. It also shows the advantage of exploring the complete parameter space, since some of the fireball parameters are highly degenerate. 2.) The short γ-ray burst (GRB) sample reveals that off-axis effects play an important role, when estimating the jet opening angle. I found that short GRBs have a median opening angle $\theta_0 = 0.12^{+0.07}_{-0.06}$ rad and a median observer angle $\theta_{\mathrm{obs,short}}/\theta_0 = 0.6^{+0.1}_{-0.4}$. The angles do not differ significantly from the corresponding angles of long GRBs. 3.) The plateau phase of GRB 150424A can be explained by prolonged energy injection into the jet. The energy injection profile, and the total amount of energy radiated during the prompt and afterglow phase of this GRB is consistent with a magnetar progenitor.

ZUSAMMENFASSUNG

Gammastrahlenausbrüche (Englisch: Gamma-Ray Burst, GRB) gehören zu den leuchtstärksten Explosionen im Universum. Sie sind nach ihrer anfänglichen γ-Strahlung benannt, die Sekunden dauert. Dieser folgt ein lange andauerndes breitbandiges Nachglühen. Man unterscheidet mindestens zwei Arten von GRBs: kurze harte GRBs und lange weiche GRBs. Die zwei Arten unterscheiden sich in zeitlicher Länge der anfänglichen γ-Strahlung und der Härte des γ-Spektrums. Kurze GRBs entstehen aus zwei kollidierenden Neutronensternen oder aus der Kollision eines Neutronensterns mit einem Schwarzen Loch. Lange GRBs entstehen, wenn ein sehr massereicher Stern kollabiert. GRBs wurden bei sehr hohen Rotverschiebungen beobachtet, und sind exzellente Proben für das frühe Universum. Darüber hinaus können wir mit GRBs unser Verständnis von Physik unter extremen Bedingungen testen.

Die beobachteten Eigenschaften von langen und kurzen GRBs scheinen grundsätzlich ähnlich zu sein. GRBs können sehr erfolgreich mit dem *Feuerballmodel* erklärt werden. Das Model beschreibt das Nachglühen als Synchrotronstrahlung eines Schocks, der auftritt, wenn ein ultra-relativistischer gerichteter Materiefluss auf das umgebende Medium trifft. Es gibt jedoch mehrere Wege das Feuerballmodell umzusetzen: Die verschiedenen Umsetzungen basieren auf unterschiedlichen physikalischen Annahmen, z.B. über die genaue räumliche Struktur des gerichteten Materieflusses, oder das zeitliche Profil mit dem Energie in den Fluss injiziert wird. Es werden auch unterschiedliche Näherungen gemacht, z.B. dass die Expansion des Feuerballes ein adiabatischer Prozess ist, oder dass die Schockwelle immer ultra-relativistische Geschwindigkeit hat, obwohl sie langsamer wird. Zusätzlich zu den zahlreichen analytischen Umsetzungen wurden in den letzten Jahren Modelle realisiert, welche auf numerischen Simulationen beruhen. Eine Folge dieser Mannigfaltigkeit an Variationen des Feuerballmodels ist, dass die exakten Werte der Modelparameter ungewiss sind.

In dieser Arbeit werde ich das Feurballmodell für das Nachglühen von GRBs anwenden. Als erstes vergleiche ich verschiedene Analysemethoden und Umsetzungen des Models, indem ich Daten des „Lehrbuch" Nachglühens von GRB 081121A verwende. Danach wende ich ein Model, welches auf hydro-dynamischen Simulationen basiert, auf eine Sammlung an Nachglühen von kurzen GRBs an. Schlussendlich analysiere ich Daten des besonders interessanten GRB 150424A, ein kurzer GRB mit lange anhaltender schwacher γ-Strahlung und einem Plateau in der Lichtkurve des optischen Nachglühens.

Meine Ergebnisse lassen sich wie folgt zusammenfassen: 1.) Die Anwendung verschiedener Analyseansätze auf GRB 081121A zeigt, wie stark das Ergebnis einer Analyse von der verwendeten Umsetzung des Feuerballmodels und der Vollständigkeit der Daten abhängt. Es zeigt ebenfalls, dass es von Vorteil ist, den gesamten Parameterraum zu erkunden, da einige Feuerballparameter stark korrelieren. 2.) Die Sammlung von kurzen GRBs offenbart, dass Effekte, die auftreten, wenn der Beobachter sich nicht auf der Achse des gerichteten Materieflusses befindet, eine wichtige Rolle spielen, wenn es darum geht den Öffnungswinkel zu bestimmen. Ich finde heraus, dass der Öffnungswinkel $\theta_0 = 0.12^{+0.07}_{-0.06}$ rad und der Beobachterwinkel $\theta_{\mathrm{obs,short}}/\theta_0 = 0.6^{+0.1}_{-0.4}$ ist. Die Verteilung der Winkel unterscheidet sich nicht zwischen kurzen und langen GRBs. 3.) Das Plateau in der Lichtkurve von GRB 150424A kann durch Energieinjektion in den Materiefluss erklärt werden. Das zeitliche Profil mit dem Energie in den Materiefluss injiziert wird, und die gesamte Energie die von diesem GRB emittiert wird, ist konsistent mit einem Magnetar als Vorläuferobjekt.

CHAPTER 1

INTRODUCTION

1.1. A Short History of Gamma-Ray-Bursts

With a record breaking isotropic energy equivalent in the γ-band of $E_{\gamma,\mathrm{iso}} = 8.8 \cdot 10^{54}$erg (Abdo et al. 2009) GRBs are among the most luminous events in the Universe. They have been observed in our direct neighborhood (redshift $z \approx 0.0085$ (Iwamoto et al. 1998)) and up to a $z \approx 9.4$ (Cucchiara et al. 2011). GRBs are named after their second-long prompt γ emission. The prompt phase is followed by a broad-band afterglow seen in the X-ray to the NIR regime for days, up to months in the sub-mm and radio regime.

The first GRB was detected by the Vela satellite network (1963-1984) on 2nd July 1967. The Vela satellites (from Spanish "Velador "for "watchman ") were designed to monitor the earth for γ and X-ray photons produced by atomic bombs. 6 years later 16 GRB detections were published as extraterrestrial event (Klebesadel et al. 1973). GRB science was born!

Thanks to many sophisticated instruments and observational programs, astronomers and astrophysicists were able to uncover the secrets of those fascinating objects step by step. Early data from space based observatories like Konus and the Burst and Transient Source Experiment (BATSE) showed an isotropic distribution of GRBs over the sky (Mazets et al. 1981; Atteia et al. 1987; Meegan et al. 1993; Paciesas et al. 1999; review: Preece et al. 2000; also see Fig. 1.1), supporting the idea of GRBs as extra-galactic sources.

BeppoSax (1996-2002) (Beppo in honor of Giuseppe "Beppo" Occhialini and SAX as acronym for 'Satellite per Astronomia X'; Scarsi 1997) had the capability to produce high resolution X-ray images (Costa et al. 1997), which made ground-based follow-up observations possible. Although broad-band afterglows have been predicted (Mészáros & Rees 1997a) their first detection certainly was a breakthrough
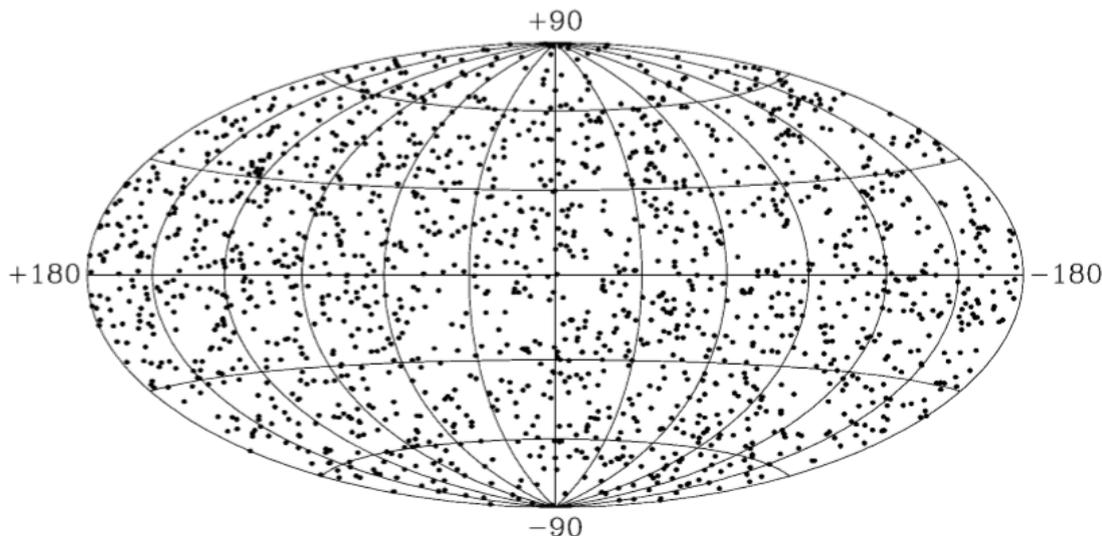
Figure 1.1.: Coordinates of the BATSE 4th GRB data sample release, including the position of 1637 GRBs (Paciesas et al. 1999). The distribution over the sky is isotropic, which is a strong indicator that GRBs do not origin in the Milky Way.

(GRB 970228, van Paradijs et al. 1997). Shortly after, the first photometric redshift measurements proved GRBs to be at cosmological distances and of extraordinary luminosity (GRB 970508 with $z = 0.835$, Metzger et al. 1997; GRB 971214 with $z = 3.42$ Kulkarni et al. 1998).

In astronomical sources, time-scales of processes that are shorter than the light crossing time of the object will be smeared out from a measured signal. Therefore, the size of a the emitting region R of a GRB is roughly constrained by the time-scale of its variability δt over

$$R < c\delta t \tag{1.1}$$

with the speed of light c. The time-scale of the GRB prompt emission variability implies a $R \sim 10^7$cm (Vedrenne 2009), which is smaller than an Active Galactic Nucleus (AGN), and even smaller than a solar radius $R_\odot = 7 \times 10^{10}$cm.

There are at least two different classes of GRBs: short hard GRBs and long soft GRBs. They form a bi-modal distribution in the parameters space of the time in which they emit 90% of their prompt γ energy T_{90}, and the hardness of their emission spectrum (Kouveliotou et al. 1993; Fishman et al. 1994) (see Fig. 1.2). Classically the two classes are separated by a $T_{90} \approx 2$s, but in the last years additional sub-classes of GRBs have been proposed: ultra long GRBs and short GRBs with Extended Emission (EE).

The EE occurs in the γ-band, after the short prompt γ flash (e.g. Mazets et al. (2002); Norris & Bonnell (2006); Norris et al. (2010)). EE short GRBs can have a significantly longer T_{90} than the short GRBs typical $T_{90} < 2$s. Since EE also is
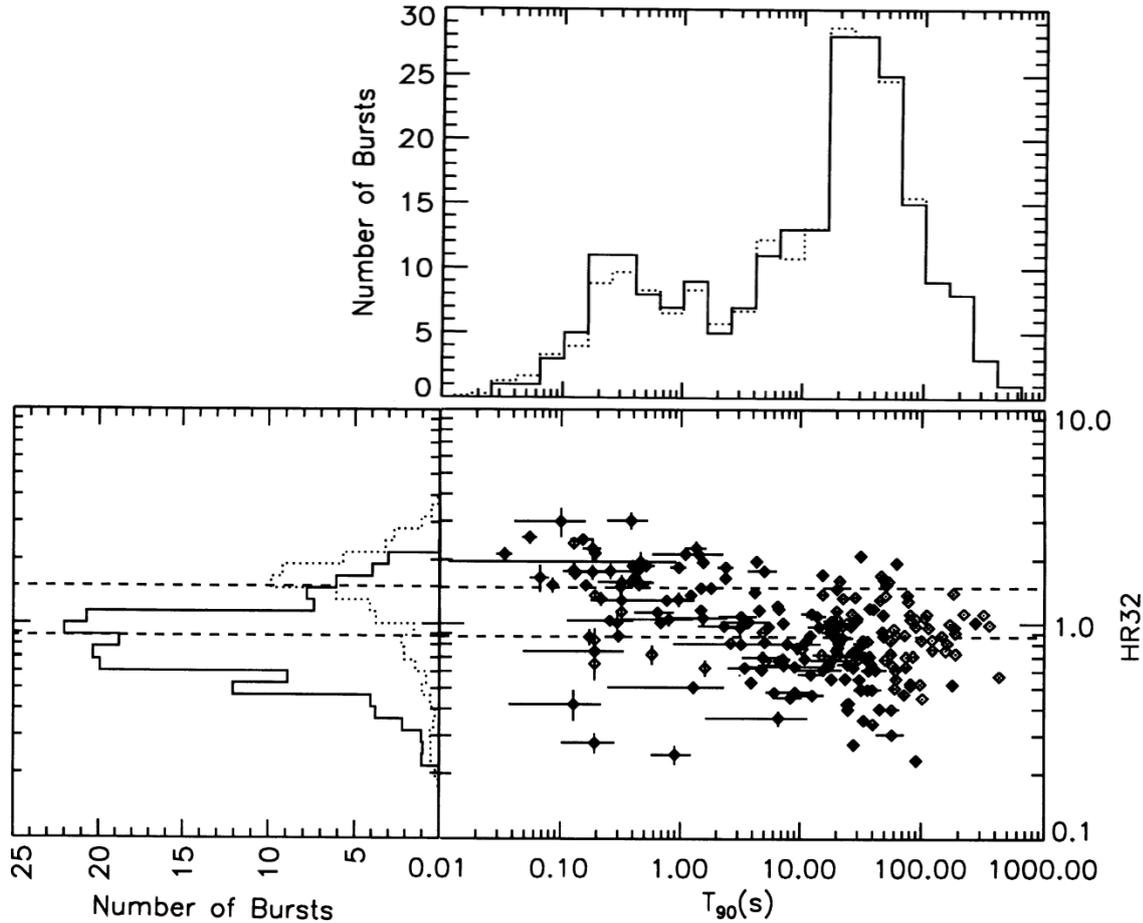
Figure 1.2.: Distribution of GRBs of the first BATSE catalog in the T_{90} / hardness-ratio plane (Kouveliotou et al. 1993). Two different populations are distinguishable: long soft and short hard GRBs. The solid hardness ratio histogram is for long soft GRBs, the dotted histogram for short hard GRBs. The dashed horizontal lines are the mean hardness ratios for both classes. The solid histogram of T_{90} is the raw data, the dotted line the error-convolved histogram.

spectrally softer, the classification according to the T_{90} is debated.

Multiple classes of GRBs imply, that there are different progenitors for each class. Long GRBs are thought to be the results of the collapse of a massive star (Woosley 1993; Paczyński 1998), which is observationally confirmed routinely for closer events (first: GRB 970228 by van Paradijs et al. (1997), later by e.g. Stanek et al. (2003); Greiner et al. (2015) and many others).

Short GRBs are thought to be the result of a compact binary merger (CBM) (Eichler et al. 1989; Meszaros & Rees 1992; Narayan et al. 1992; Mészáros & Rees 1997b). So far there is just vague direct observational evidence for the CBM scenario. Tanvir et al. (2013) and Berger (2014) claim the detection of a thermal transient driven by a neutron star merger, a kilonova. A CBM generally serves as an excellent example of a source for gravitational waves (Cutler et al. 1993), therefore facilities like Advanced LIGO (Aasi et al. 2015) and Advanced VIRGO (Acernese et al. 2015)

will bring new insights. There is a passionate discussion going on, if one of the first 3 gravitational wave events, GW150914, is connected to the detection of a short GRB Connaughton et al. (2016). The short GRB rate also is consistent with the expected CBM rate (Fong et al. 2012; Wanderman & Piran 2015). The offsets of short GRBs to the center of their host galaxies corresponds with the theoretical predictions for the kick a compact binary receives when formed (Berger 2010). Short GRBs are believed to originate from older stellar populations (reviews e.g. Fong et al. (2013); Berger (2014)), and often occur at a relative offset to the host galaxies center (Belczynski et al. 2006; Fong et al. 2010; Church et al. 2011; Fong & Berger 2013; Behroozi et al. 2014). Moreover, unlike for long GRBs, core collapse supernova are ruled out due to a lack of observational associations (Hjorth et al. 2005a).

Today the community has access to data from multiple satellite missions, like the Swift satellite (2004-today), Fermi (2008-today) and INTEGRAL (International Gamma-Ray Astrophysics Laboratory) (2002-today), as well as from Earth bound facilities like the Gamma-Ray Optical Near-infra-red Detector (GROND) (Greiner et al. 2008), RATIR and others. All the data is helping to form the most successful explanation of the physical processes behind a GRB: The fireball model.

1.2. The Fireball Model

Within the fireball model a GRB is described as an ultra-relativistic outflow. Internal shocks in this outflow are believed to produce the prompt γ radiation (Rees & Meszaros 1992; Meszaros & Rees 1993; Meszaros et al. 1993; Sari & Piran 1995; Rees & Meszaros 1994), an external shock forms the broad-band afterglow (see Fig. 1.3). Both classes of GRBs, short and long, are linked to the progenitor physics just over the energy injected to the outflow, and can therefore be described in the same manner, while being agnostic about the progenitor itself.

Prompt emission

According to the fireball model, the large energy output in a small volume, during the short time-scales of a GRB produces a fireball, that consists of an $e^{\pm}$-photon plasma. Since a dampening of the flux above 1MeV (the energy of $e^{\pm}$ creation) is not observed (Matz et al. 1985), the fireball has to be opaque to pair creation (Cavallo & Rees 1978; Paczynski 1986; Goodman 1986). That is the case when the outflow moves with a high bulk Lorentz-factor Γ, that

1. Blue-shifts the photons and shortens their time-scales

2. Increase the co-moving size of the fireball by Γ^2, therefore decreases the co-moving density
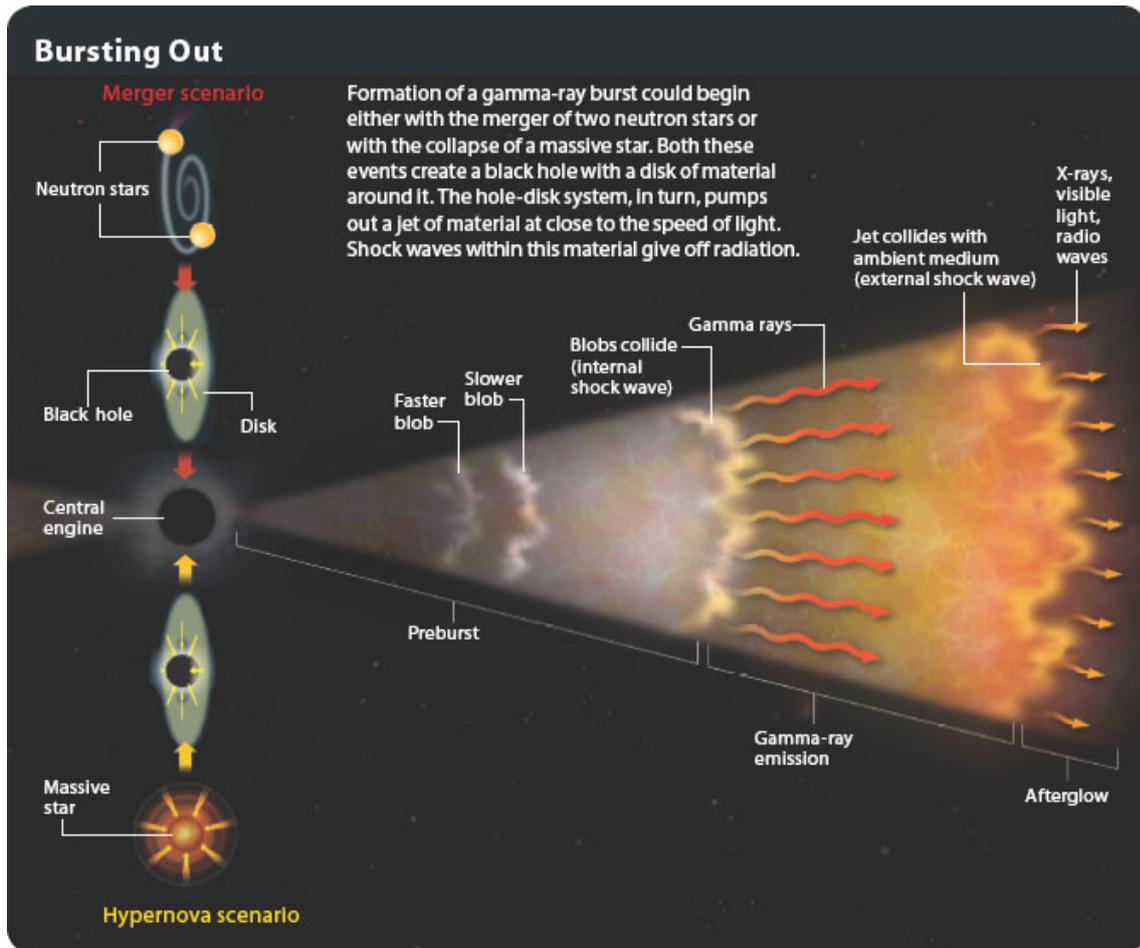
Figure 1.3.: Visualisation of the fireball model (from Gehrels et al. (2002), credit Juan Velasco).

A $\Gamma \gtrsim 100$ would be needed Piran (1999); Lithwick & Sari (2001); Mészáros et al. (2002), but only can be reached if the baryon load is low (Paczynski & Proszynski 1986; Paczynski 1990).

The majority of the matter swept up by the fireball would be concentrated in a thin shell, where the $e^\pm$ and photons are in a quasi-equilibrium, therefore would emit quasi-thermally. However, a quasi-thermal spectrum is not observed.

Instead, the majority of the fireball energy has to be carried by kinetic energy of the baryons. Different shells with different Γ overtake each other and produce internal shocks. Those relativistic shocks in the outflow accelerate electrons via the Fermi process (Fermi (1949), review of acceleration processes by Blandford & Eichler 1987). The electrons then emit a non-thermal spectrum with a smoothly-joining broken power-law shape with the break at $\sim 0.1 - 1\mathrm{MeV}$ (Band et al. 1993) via synchrotron radiation. However, recent studies showed that a majority of the prompt emission spectra is to sharp to be explained by synchrotron emission (Yu et al. 2015).

Afterglow

The afterglow is described as synchrotron radiation from electrons, Fermi-accelerated
in an external shock. By modeling afterglow data it is possible to derive global prop-
erties of GRBs, like opening angle and their micro-physics, sample properties like
the distribution of the observer angle, and it is possible to put constraints on the
progenitor of the GRB.

   In this thesis I will exclusively work with afterglow data and models. Therefore
I dedicate Chapter 2 to a more quantitative introduction of afterglows within the
fireball model.

Alternative models

The fireball model is very successful since it can explain the prompt and afterglow
emission with just few assumptions and a limited amount of parameters. However, a
number of alternative models are found in the literature to describe GRBs generally
or certain features of it:

- To explain the prompt emission e.g. Drenkhahn & Spruit (2002) suggested a
  pointing flux model, in which magnetic dissipation through magnetic recon-
  nection accelerates the electrons. One-dimensional steady relativistic MHD
  calculations showed, however, that mainly X-ray photons instead of γ pho-
  tons are produced. Kagan et al. (2015) also showed that the spectral shape
  produced by the model does not describe the observations.

- The fast variability in the prompt γ emission can be explained by *minijets*.
  Minijets are compact active regions in the jet which experience relativistic mo-
  tions relative to the co-moving frame (Barniol Duran et al. 2016, and references
  therein).

- Dermer et al. (1999) claimed the prompt emission to be the result of external
  shocks, when a thin relativistic blast wave interacts with a clumpy circumburst
  medium.

- During the prompt phase, thermal emission from a photosphere also con-
  tributes (e.g. Goodman 1986; Bégué & Burgess 2016). A photosphere could
  explain the origin of X-ray flares (e.g. Beniamini & Kumar 2016).

- The cannonball model (e.g. Dado et al. 2002, 2003) explains afterglows by jets
  of highly relativistic "cannonballs" that pierce through the supernova shell,
  while heating up. The resulting cannonball surface radiation, Doppler-shifted
  in energy and forward-collimated by its relativistic velocity is seen as prompt

emission. The afterglow is explained as mixture of emission from the cannon-ball, the accompanying supernova and the host galaxy.

1.3. Content of This Thesis

In this thesis I will apply the fireball model for GRB afterglows, using data from GROND, the Swift/XRT, the Swift/UVOT, the Hubble Space Telescope (HST) and additional data from the literature and the Gamma-ray Coordinates Network (GCN).

In Chapter 2, I will introduce the fireball model for GRB afterglows in more detail. I will show the basic assumptions, capabilities and limitations of the model. I will define all fireball parameters and observables and show the reader how to transform the basic concepts of the fireball model to quantitative statements. I will give a summary of the open questions concerning the fireball model itself, and different implementations that can be found in the literature.

In Chapter 3, I will write about the "textbook" GRB 081121A. I will describe my methods to correct for non GRB related physics, extinction and absorption. Additionally I will describe the technical implementation of two distinct models and the use of Monte Carlo Markov Chain (MCMC) methods to fit the data. For the first time I will apply the SCALEFIT software to broad-band data of a GRB afterglow. I will compare the results of SCALEFITS with a classical approach using the so called *closure relations*. I will discuss the limitations and capabilities of the two distinct models and the two different analysis schemes. Moreover, I find general limitations of the fireball model for afterglows: depending on the data coverage, the fireball parameters can be strongly degenerate, and the interpretation of ϵ_e needs to be reconsidered.

In Chapter 4, I will apply SCALEFIT to a sample of short GRBs (Fong et al. 2015). I will compare my analysis to a classical approach, that depends on a clear jet-break in the light curve. I derive 12 jet opening angles, where the classical approach is capable of deriving 4. Additionally I derive 14 observer angles, while the classical approach assumes an on-axis observation. Finally, I compare the distribution of jet opening angles of short GRBs to the distribution of jet opening angles of long GRBs.

In Chapter 5, I will show data of an EE short GRBs with a shallow decay phase in the afterglow: GRB 150424A. The presented high-quality data-set so far is unique in temporal and spectral coverage. I will perform a phenomenological analysis and interpret the results in the context of energy injection. The injected energy is consistent with a strongly magnetized and rapidly rotating neutron star, a magnetar, as progenitor.

CHAPTER 2

THE AFTERGLOW

In this chapter I will introduce the fundamental concept of the fireball model for afterglows. I will present one specific implementation, which will help the reader to understand the fireball model in a quantitative way. Afterwards I will summarize limitations of this specific model and summarize other approaches found in the literature. Finally I will introduce the so called *closure relations*.

2.1. Basic Concept and Capabilities

In the fireball model the afterglow emission is assumed to be synchrotron radiation from shock accelerated electrons when an ultra-relativistic jetted outflow hits the circum-burst medium. The model is capable to describe a GRB afterglow with just a limited amount of parameters $\Theta = (E_{\mathrm{iso}}, n, \theta_0, \theta_{\mathrm{obs}}, p, \epsilon_e, \epsilon_B, \xi_N, z, d_L(z))$:

$$
\text{Dynamics} \begin{cases} E_{\mathrm{iso}} & \text{kinetic isotropic energy equivalent} \\ n_0 & \text{circumburst medium number density} \\ \theta_0 & \text{jet opening angle} \end{cases}
$$

$$
\text{Radiation} \begin{cases} \epsilon_e & \text{fraction of energy in electrons} \\ \epsilon_B & \text{fraction of energy in magnetic field} \\ p & \text{energy distribution index} \\ \xi_N & \text{fraction of accelerated electrons (number density)} \end{cases}
$$

$$
\text{Observer} \begin{cases} \theta_{\mathrm{obs}} & \text{observer angle} \\ d_L & \text{observer luminosity distance} \\ z & \text{redshift} \end{cases}
$$

E_{iso}, n_0 and θ_0 define the dynamics of the relativistic outflow. The circum-burst

medium can have a radial density profile $n_0 = n_{0,\text{ref}} \left(\frac{r}{r_{\text{ref}}} \right)^{-k}$. There are two special cases: The *stellar wind case* $k = 2$, and the *inter stellar medium (ISM) case* $k = 0$ with a homogeneous medium.

ϵ_e, ϵ_B, p and ξ_N parameterize the microphysics of the synchrotron emission. A synchrotron spectrum is conveniently easy characterized by the injection break frequency $\nu_m(t, \Theta)$ which corresponds to the peak of the electron energy distribution, and the cooling frequency $\nu_c(t, \Theta)$ which corresponds to the frequency above which the electrons loose a significant amount of energy due to synchrotron cooling. $\nu_m < \nu_c$ is called the *slow cooling case*, $\nu_c < \nu_m$ is called *fast cooling case*. Together with the peak flux of the spectrum $F_{\text{peak}}(t, \Theta)$ the spectral energy distribution (SED) of the afterglow is defined.

θ_{obs}, d_L and z define the position of the observer to the afterglow. Hereby d_L is a function of z and depends on the cosmology.

2.2. A Toy Model

In this section an analytical model to describe the main features of an afterglow is presented. This section is not meant as a complete reference, but shall give a basic understanding of the underlying physics. I will show how to model an isotropic ultra-relativistic blast wave in a homogeneous medium (ISM case). The synchrotron emission comes from the forward shock, that travels into the medium. An adiabatic case, where the blast wave does not loose a significant amount of energy due to the emitted radiation, is assumed.

2.2.1. A Relativistic Blast Wave

The art of afterglow modeling is to calculate the Lorentz factor γ of the external shock. In an ultra-relativistic case (velocity $\approx$ speed of light c) and with the initial mass M_0 of the outflow, the kinetic energy of the blast wave is

$$E = M_0 c^2 \gamma^2 \tag{2.1}$$

$$= \frac{4}{3} \pi R_0^3 n m_p c^2 \gamma^2 \tag{2.2}$$

The radius is $R_0 \approx ct$. It follows

$$\gamma = \left(\frac{3}{4} \frac{E}{\pi m_p c^5 n t^3} \right)^{1/8} \tag{2.3}$$

The radius of the blast wave evolves as

$$R = tc\gamma^2 \tag{2.4}$$

with the γ from above it follows

$$R = \left(\frac{3}{4} \frac{Et}{\pi m_0 cn} \right)^{1/4} \tag{2.5}$$

For the energy density and particle density one has $U_{\text{shock}} = \gamma^2 n m_p c^2$ and respectively $N = \gamma n$

(Blandford & McKee 1976) gave a self similar solution for a fluid dynamical treatment of an ultra-relativistic blast wave enclosed by a strong shock (Blandford McKee (BM) solution from now), which leads to slightly different pre-factors of the quantities:

$$U_{\text{shock}} = 4\gamma^2 n m_P c^2 \tag{2.6}$$

$$N = 4\gamma n \tag{2.7}$$

$$\gamma = \left(\frac{17}{1024} \frac{E}{\pi m_p c^5 nt^3} \right)^{1/8} \tag{2.8}$$

$$R = \left(\frac{17}{4} \frac{Et}{\pi m_0 cn} \right)^{1/4} \tag{2.9}$$

Analogous to Sari et al. (1998) I will adapt those more precise expressions from now.

2.2.2. Emission

In electrodynamics (see e.g. (B. Rybicki & P. Lightman 1979; Ghisellini 2013)) the synchrotron frequency is

$$\nu_{\text{synch}} = B \frac{3q_e}{2\pi m_e c} \gamma \gamma_e^2 \tag{2.10}$$

and the emitted power per electron is

$$P_\nu(\gamma) = \frac{4}{3} \sigma_T c \frac{B^2}{8\pi} \gamma^2 \gamma_e^2 \tag{2.11}$$

with the Lorentz factor of the electrons (in the shock wave frame) γ_e, the electron charge q_e, mass m_e and Thomson cross section σ_T, the magnetic field B and the speed of light c. The Lorentz factor of the shock γ is needed to translate from the shock frame to the rest frame.

Parameterize B

The assumption is that a constant fraction ϵ_B of the shock energy density U_{shock} goes into the magnetic field energy density $U_{\text{MagField}} = \frac{1}{8\pi} B^2$. So from $\epsilon_B U_{\text{shock}} = U_{\text{MagField}}$ follows

$$B = \sqrt{32\pi m_p \epsilon_B n}\gamma c \tag{2.12}$$

The electron energy distribution

In the model the electrons in the shock are accelerated into a power law distribution

$$N(\gamma) = K_0 * \gamma^{-p} \tag{2.13}$$

with a sharp lower energy cutoff γ_m that naturally also is the maximum of the distribution. When $p > 1$ one can normalize it

$$N_p \xi_N = \int_{\gamma_m}^{\gamma_{\text{max}}} d\gamma \ N(\gamma, p) \tag{2.14}$$

$$= K_0 \frac{1}{1-p} \left[\gamma^{1-p}\right]_{\gamma_m}^{\gamma_{\text{max}}} \tag{2.15}$$

$$\overset{p \geq 1}{=} \frac{K_0}{1-p} \left(\underbrace{\frac{1}{\gamma_{\text{max}}^{p-1}}}_{=0 \ for \ \gamma_{\text{max}} \to \infty} - \frac{1}{\gamma_m^{p-1}} \right) \tag{2.16}$$

$$= \frac{K_0}{p-1} \gamma_m^{1-p} \tag{2.17}$$

$$\to K_0 = N_p \xi_N (p-1) \gamma_m^{p-1} \tag{2.18}$$

The main frequency

Under the assumption, that the outflow is a neutral plasma (same number of protons N_p and electrons) one can calculate the total kinetic energy of the electrons

$$N_p \gamma m_p c^2 \epsilon_e = \int_{\gamma_m}^{\gamma_{\text{max}}} d\gamma \ N(\gamma, p)\gamma m_e c^2 \tag{2.19}$$

$$\tag{2.20}$$

For $\gamma_{max} \to \infty$, $p > 2$ and using K_0 as calculated above the Lorentz factor of the peak of the electron distribution is

$$\gamma_m = \frac{\epsilon_e}{\xi_N} \frac{m_p}{m_e} \frac{p-2}{p-1} \gamma \tag{2.21}$$

with Eq. 2.10 and the bulk Lorentz factor follows the main frequency (also called injection break)

$$\nu_m = 1.32519 * 10^{-3} \frac{s^{3/2}}{g^{1/2}cm} \times \left(\frac{p-2}{p-1}\right)^2 \epsilon_B^{1/2} \epsilon_e^2 E^{1/2} t^{-3/2} \qquad (2.22)$$

The cooling frequency

Above a critical value γ_c the electrons loose a significant amount of energy due to cooling over radiation. It is given by

$$\gamma \gamma_c m_e c^2 = P(\gamma_c)t \qquad (2.23)$$

all ingredients are given above and it follows

$$\gamma_c = \frac{3}{16} \frac{m_e}{m_p} (\sigma_T \epsilon_B n t)^{-1} \frac{1}{\gamma^3} \qquad (2.24)$$

with Eq. 2.10 the cooling frequency is found to be

$$\nu_c = 7.89848 * 10^{40} \frac{g^{1/2}}{cm^2 s^{3/2}} \times E^{-1/2} n^{-1} \epsilon_B^{-3/2} t^{-1/2} \qquad (2.25)$$

The peak flux

In the model all the emission comes from the electrons in the shock front. With the total number of emitting electrons $N_e := \frac{4\pi}{3} R^3 n$ one can calculate the flux at the peak of the SED [1]

$$F_{\nu,\max} = \frac{N_e}{4\pi d_L^2} \frac{P(\gamma_e)}{\nu(\gamma_e)} \qquad (2.26)$$

$$= 1.10192 * 10^{-20} cm^{3/2} \times \epsilon_B^{1/2} E n^{1/2} d_L^{-2} \qquad (2.27)$$

The spectral shape

The evolution of the Lorentz factor for a single electron is described by

$$\frac{d\gamma_e}{dt} = -\underbrace{\frac{\sigma_T B^2}{6\pi m_e c} \gamma_e^2}_{\text{radiative loss}} + \underbrace{\frac{\gamma_e}{3n} \frac{dn}{dt}}_{\text{adiabatic cooling}} \qquad (2.28)$$

Granot & Sari (2002) give a complete solution for the spectral shapes for different orders of the characteristic frequencies (see Fig. 2.1).

A more simplistic description can be found in Sari et al. (1998):

---

[1]This formula give the Flux in $\frac{g}{s^2}$ one can use the conversion $1 Jy = 10^{-23} \frac{erg}{cm^2 sHz} = 10^{-23} \frac{g}{s^2}$. All other units and constants are in the Centimetre Gram Second (CGS) system (Sec. C.1).
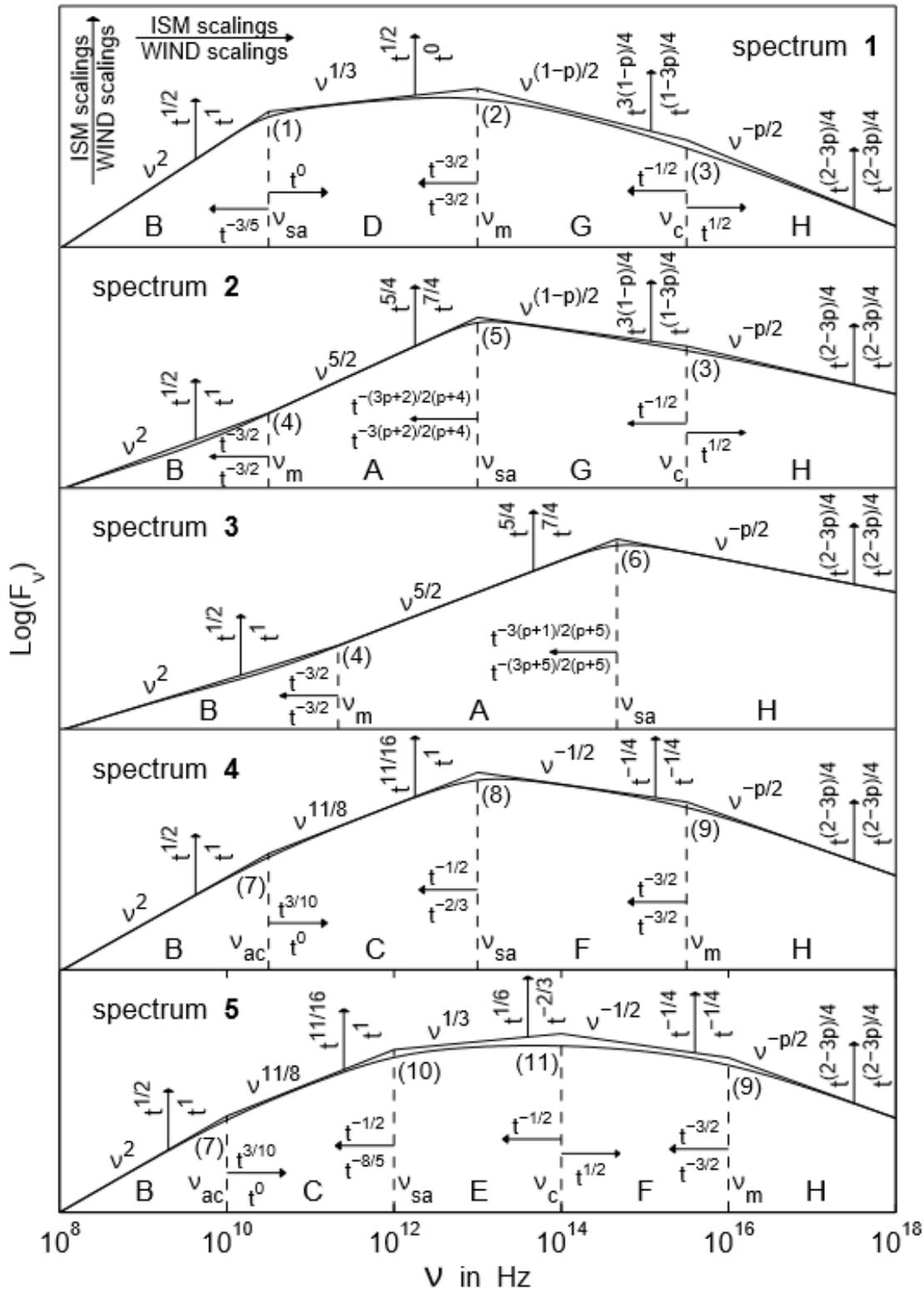
Figure 2.1.: Spectral shapes of GRB afterglows from Granot & Sari (2002). The spectral slopes β and the smoothness depend on the ordering of the characteristic frequencies.

$$F_\nu = \begin{cases} (\nu/\nu_c)^{1/3} F_{\nu,\max}, & ,\nu_c > \nu \\ (\nu/\nu_c)^{-1/2} F_{\nu,\max}, & ,\nu_m > \nu > \nu_c \\ (\nu_m/\nu_c)^{-1/2}(\nu/\nu_m)^{-p/2} F_{\nu,\max}, & ,\nu > \nu_m \end{cases} \qquad (2.29)$$

$$F_\nu = \begin{cases} (\nu/\nu_m)^{1/3} F_{\nu,\max}, & ,\nu_m > \nu \\ (\nu/\nu_m)^{-(p-1)/2} F_{\nu,\max}, & ,\nu_c > \nu > \nu_m \\ (\nu_c/\nu_m)^{-(p-1)/2}(\nu/\nu_c)^{-p/2} F_{\nu,\max}, & ,\nu > \nu_c \end{cases} \qquad (2.30)$$

2.3. Limitations and Other Approaches

2.3.1. The Jetted Nature of the Outflow

Models that assume an isotropic outflow already give a good quantitative approximation to an afterglow. Reasoning concerning the total energy budget of GRBs, however, implies a jetted outflow (reviews e.g. Berger et al. (2004)).

Rhoads (1997, 1999a,b); Sari et al. (1999); Frail et al. (2001) derived a jet signature: the jet break. A jet break occurs, when the outflow starts sidewards spreading at the jet break time

$$t_{\mathrm{obs,break}} \propto \begin{cases} \left(\dfrac{E}{n_0}\right)^{1/3} \theta_0^{8/3} & ,\mathrm{ISM} \\ \left(\dfrac{E}{n_0}\right) \theta_0^4 & ,\mathrm{wind} \end{cases} \qquad (2.31)$$

After the jet break, the light curve will steepen. Depending on the structure of the jet $t_{\mathrm{obs},break}$ has an observer angle dependency and can be used to constrain it (e.g. Ryan et al. 2015).

From a non-spreading jet, a break in the light curve is also expected. The relativistic beaming angle of the emission of the individual electrons

$$\theta_{\mathrm{beam}} \propto \gamma^{-1} \qquad (2.32)$$

is decreasing with a decreasing bulk Lorentz factor γ. So after more time, more emission from the shock front that is not directly in the line of sight of the observer becomes visible. The decreasing emitted flux is partly compensated by the increasing flux that becomes visible to the observer. After the beaming is low enough that the whole jet front is visible, and the decreasing emitted flux is not compensated any more, so the light curve steepens.

Not all GRBs show a jet break (Kocevski & Butler 2008; Racusin et al. 2009). And some of the afterglows that have a break, do not show a sudden break as originally suggested. The two effects from above overlap and smear out the jet break. Moreover, numerical studies showed that there is a regime of sideways spreading

right from the beginning instead of a sudden runaway behaviour at the jet break time van Eerten & MacFadyen (2012b).

2.3.2. Further Complications

The real afterglow phenomenology is complex (see Fig. 2.3 and Fig. 2.2). To explain all different features of a "typical" light curve, there are dozens of models in literature, with different approximations and assumptions. One should be aware that the outcome of the analysis always is model depended! Some things to keep in mind:

- Is synchrotron emission from a power law electron population the only emission component? If not all electrons are accelerated to a power law energy distribution ($\xi_N < 1$), how can one detect the rest? Eichler & Waxman (2005) give a signature for synchrotron emission from a thermal electron population.

- Is the parametrisation of the electron energy distribution accurate? Warren et al. (2017) perform simulation of the Fermi-acceleration process and find that a substantial fraction of the electrons does not enter the process at all, and that the electron population is at no time well fitted by a single power law. The consequences are a hard–soft–hard spectral evolution at X-ray energies, as well as an uncoupled X-ray and optical light curve. Additionally, emission from thermal particles increases the observed flux at optical and GeV energies by factors of 100 and 30, respectively.

- Are the micro-physical parameters constant in time? Filgas et al. (2011) suggested that ϵ_B follows a time evolution.

- Models with ultra-relativistic solutions for the outflow (all models, building on the BM solution) loose their validity as soon as the outflow decelerates. For the non-relativistic regime another self similar solution exists, given by Sedov (1959) and Taylor (1950). The transition from one regime to another is not trivial and numerical approaches have to be used (van Eerten et al. 2010b; Leventis et al. 2012).

- The blast wave does not expands adiabatically. If the radiative losses during the expansion is not negligible, some adjustments to the dynamics have to be made (Sari 1997; Sari et al. 1998; Mészáros et al. 1998; Panaitescu & Mészáros 1998).

- The ISM and stellar wind cases may be oversimplified. The real radial density profile may be more complex. In some models the circumburst density distribution parameter k is a free fitting parameter (Leventis et al. 2012). Also

more exotic scenarios, like a sudden density jump in the circum-burst medium can be found in the literature (Dai & Lu 2002; Gat et al. 2013).

- Besides a forward shock, propagating into the circum-burst medium, there is a reverse shock, traveling into the ejecta. The resulting SED is an overlap of two synchrotron components (Meszaros & Rees 1993; van Eerten 2014) Reverse shocks have been well observed in the radio regime (e.g. Laskar et al. 2016)

- Numerical studies show that (in long GRBs) the jet is probably surrounded by a second jet with a lower Lorentz factor, a cocoon (Piro et al. 2014; Nakar & Piran 2017). A cocoon is expected to evolve, when the jet breaks out of the envelope of the progenitor star.

- At late times even a counter jet, pointing away from the observer may be seen.

- Most stars are bound in a binary system. I am not aware of any studies about the influence of a companion star of the long GRB's progenitor.

- A typical afterglow follows a strictly decaying power-law, which is easily explained by an impulsive energy injection into the outflow. Some GRBs show a shallow decay phase in the afterglow light curve with a temporal slope $\alpha \lesssim 1/4$ [2], where the standard model predicts a temporal slope $\alpha \sim 1$. Such a "plateau phase" can be explained by a prolonged energy injection. (Rees & Meszaros 1994; Zhang & Mészáros 2001; Kumar & Barniol Duran 2010; van Eerten 2014; Laskar et al. 2015). A magnetar as provider for energy injection will be discussed in Chapter 5.

2.4. The Closure Relations

An afterglow can be described over the empirical flux equation

$$F(\nu, t) \propto t^{-\alpha} \nu^{-\beta} \tag{2.33}$$

with the time after the burst t and the observer frequency ν,

- the temporal slope α

- the energy index or spectral slope $\beta = \Gamma - 1$

- the photon index Γ is often used in the high-energy community

---

[2]The sign of the slope is convention. I follow Eq. 2.33, where a positive number means a decaying light curve.

In a dynamical afterglow model one can link the temporal and spectral behaviour of an afterglow over a set of so called closure relations α and β. Depending on the observed frequency and the dynamical state of the outflow (e.g. isotropic outflow, spreading jet, non-spreading jet..) a model gives different α and β pairs. A collection of closure relations of different models is given by Racusin et al. (2009) (see Tab. 2.1).

Table 2.1.: Closure relations collected and expanded by Racusin et al. (2009). They are collected from Zhang & Mészáros (2004); Zhang et al. (2006); Dai & Cheng (2001); Panaitescu et al. (2006); Panaitescu (2005).

		β	a No Energy Injection $\alpha(\beta)$ $(p>2)$	b $\alpha(\beta)$ $(1<p<2)$	c Energy Injection $\alpha(\beta)$ $(p>2)$
			ISM, Slow Cooling		
1	$\nu_m < \nu < \nu_c$	$\frac{p-1}{2}$	$\alpha = \frac{3\beta}{2}$	$\alpha = \frac{3(2\beta+3)}{16}$	$\alpha = (q-1) + \frac{(2+q)\beta}{2}$
2	$\nu > \nu_c$	$\frac{p}{2}$	$\alpha = \frac{3\beta-1}{2}$	$\alpha = \frac{3\beta+5}{8}$	$\alpha = \frac{q-2}{2} + \frac{(2+q)\beta}{2}$
			ISM, Fast Cooling		
3	$\nu_c < \nu < \nu_m$	$\frac{1}{2}$	$\alpha = \frac{\beta}{2}$	$\alpha = \frac{\beta}{2}$	$\alpha = (q-1) + \frac{(2-q)\beta}{2}$
4	$\nu > \nu_m$	$\frac{p}{2}$	$\alpha = \frac{3\beta-1}{2}$	$\alpha = \frac{3\beta+5}{8}$	$\alpha = \frac{q-2}{2} + \frac{(2+q)\beta}{2}$
			Wind, Slow Cooling		
5	$\nu_m < \nu < \nu_c$	$\frac{p-1}{2}$	$\alpha = \frac{3\beta+1}{2}$	$\alpha = \frac{2\beta+9}{8}$	$\alpha = \frac{q}{2} + \frac{(2+q)\beta}{2}$
6	$\nu > \nu_c$	$\frac{p}{2}$	$\alpha = \frac{3\beta-1}{2}$	$\alpha = \frac{\beta+3}{4}$	$\alpha = \frac{q-2}{2} + \frac{(2+q)\beta}{2}$
			Wind, Fast Cooling		
7	$\nu_c < \nu < \nu_m$	$\frac{1}{2}$	$\alpha = \frac{1-\beta}{2}$	$\alpha = \frac{1-\beta}{2}$	$\alpha = \frac{q}{2} - \frac{(2-q)\beta}{2}$
8	$\nu > \nu_m$	$\frac{p}{2}$	$\alpha = \frac{3\beta-1}{2}$	$\alpha = \frac{\beta+3}{4}$	$\alpha = \frac{q-2}{2} + \frac{(2+q)\beta}{2}$
			Uniform Jet (spreading), Slow Cooling		
9	$\nu_m < \nu < \nu_c$	$\frac{p-1}{2}$	$\alpha = 2\beta + 1$	$\alpha = \frac{2\beta+7}{4}$	$\alpha = 2\beta + 1 - \frac{2(1-q)(\beta+2)}{3}$
10	$\nu > \nu_c$	$\frac{p}{2}$	$\alpha = 2\beta$	$\alpha = \frac{\beta+3}{2}$	$\alpha = 2\beta - \frac{2(1-q)(\beta+1)}{3}$
			ISM, Uniform Jet (nonspreading)		
11	$\nu_m < \nu < \nu_c$	$\frac{p-1}{2}$	$\alpha = \frac{6\beta+3}{4}$	$\alpha = \frac{6\beta+21}{16}$	$\alpha = \frac{6\beta+3}{4} - \frac{(1-q)(2\beta+5)}{4}$
12	$\nu > \nu_c$	$\frac{p}{2}$	$\alpha = \frac{6\beta+1}{4}$	$\alpha = \frac{3\beta+11}{8}$	$\alpha = \frac{6\beta+1}{4} - \frac{(1-q)(2\beta+3)}{4}$
			Wind, Uniform Jet (nonspreading)		
13	$\nu_m < \nu < \nu_c$	$\frac{p-1}{2}$	$\alpha = \frac{3\beta+2}{2}$	$\alpha = \frac{2\beta+13}{8}$	$\alpha = \frac{3\beta+2}{2} - \frac{(1-q)(\beta+2)}{2}$
14	$\nu > \nu_c$	$\frac{p}{2}$	$\alpha = \frac{3\beta}{2}$	$\alpha = \frac{\beta+5}{4}$	$\alpha = \frac{3\beta}{2} - \frac{(1-q)(\beta+2)}{2}$
			ISM, Structured Jet		
15	$\nu_m < \nu < \nu_c$	$\frac{p-1}{2}$	$\alpha = \frac{3k+12\beta}{8-k}$		
16	$\nu > \nu_c$	$\frac{p}{2}$	$\alpha = \frac{12\beta+2k-4}{8-k}$		
			Wind, Structured Jet		
17	$\nu_m < \nu < \nu_c$	$\frac{p-1}{2}$	$\alpha = \frac{6\beta+k\beta+2}{4-k}$		
18	$\nu > \nu_c$	$\frac{p}{2}$	$\alpha = \frac{6\beta+k-k\beta-2}{4-k}$		

Figure 2.2.: Schematic X-ray light curve from Zhang et al. (2006). The normal decay phase (III) is expected to be followed by a post jet break phase (IV). Before that a shallow decay phase (II) is observed regularly. It may be coincide with flares (V). *Swift* revealed a prompt emission phase (0), followed by a steep decay (I).
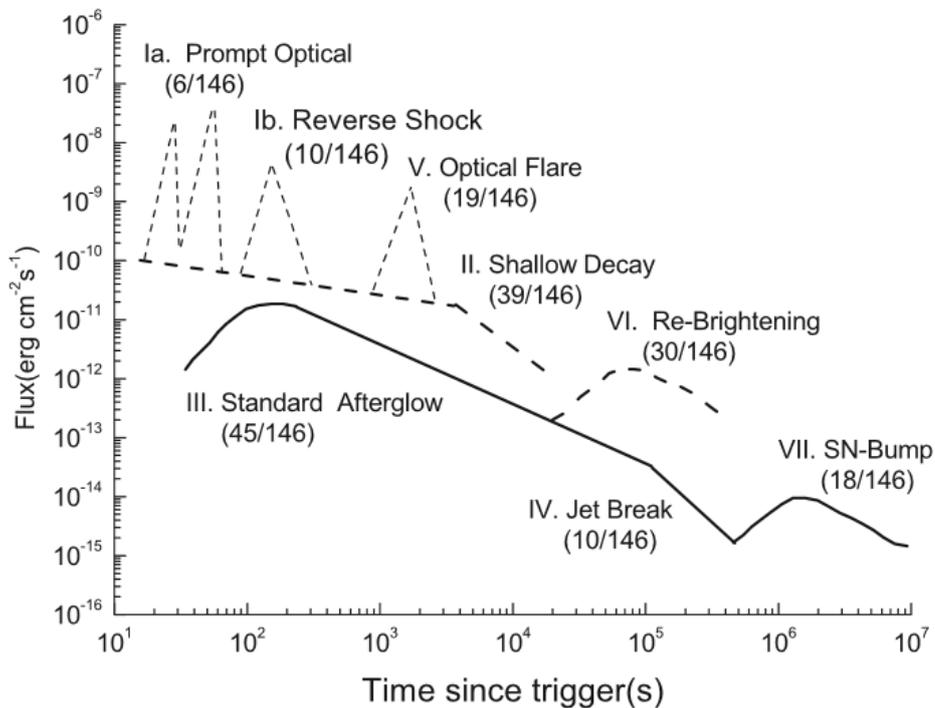
Figure 2.3.: Schematic optical light curve from Li et al. (2012). The standard afterglow (III) in some cases shows a jet break (IV) and for long GRBs the accompanying supernova may be detectable (VII). A rebrightening was observed (VI). Like the X-ray, the optical afterglow shows a shallow afterglow component (Ia) with optical flares (V), followed by a shallow decay (II). A feature so far not observed in the X-ray is the reverse shock (Ib) from a shock wave traveling into the ejecta.

CHAPTER 3

THE TEXTBOOK AFTERGLOW OF GRB 081121A

In this chapter I compare an analytical afterglow model to a model with templates, based in hydro-dynamical simulations. I also compare a classical 'snap-shot' analysis with a Bayesian approach, modelling SED evolutions. This chapter was summarized in my first paper draft, but the submission is pending until the release paper of the SCALEFIT (Van Eerten in prep., Ryan et al. 2015) software package.

3.1. GRB Details

GRB 081121A has high quality multi-band data from GROND (g', r', i', z', J, H and K_s band), Swift/UVOT (u, b and v band) and Swift/XRT (X-ray spectra), with a high temporal coverage. GRB 081121A has a relatively simple light curve, making it an an excellent "textbook" case to apply different implementations of the fireball model. I can test the decay phase of an afterglow within the fireball model without any further complications, like flares or re-brightening in the light curve, a super nova component, or a shallow decay phases.

I also can compare a classical snap-shot analysis to a new fitting approach based on SED evolutions and Bayesian methods. The Bayesian approach already was successfully applied to XRT single band data (Ryan et al. 2015). This approach makes it possible to explore the whole parameters space. Instead of just looking for the most probable parameter set $\Theta = (E_{\mathrm{iso}}, n, \theta_0, \theta_{\mathrm{obs}}, p, \epsilon_e, \epsilon_B, \xi_N, z, d_L(z))$, I can see degeneracies between parameters and multi-modal behaviour of the parameter distribution.

Sec. 3.2 gives an overview over the GRB 081121A data I use. In Sec. 3.3.1 I first perform a phenomenological analysis, followed by an introduction of the physical models and their limitations in Sec. 3.3.2. Afterwards I go one step further and fit complete SED evolutions using a Bayesian approach with SCALEFIT in Sec. 3.3.3.

In Sec. 3.4 I discuss both methods, followed by my conclusions in Sec. 3.5.

3.2. Data

On November the 21st 2008 at 20:35UT, the Burst Alert Monitor (BAT) triggered on GRB081121A (Oates et al. 2008) and the XRT began observing 2800 seconds thereafter (Goad et al. 2008; Godet & Oates 2008). GROND (Greiner et al. 2008) began its follow up observations on 22nd November 2008 at 00:29UT, 3.9 hrs after the trigger (Loew et al. 2008), for a total of 57 observations, distributed over 6 nights. Golenetskii et al. (2008) reported an $E_{\gamma,\mathrm{iso}} = 2.7 \times 10^{53}$ erg The redshift $z = 2.512$ (Berger & Rauch 2008) leads to a luminosity distance $d_L = 6.49 \times 10^{28}$ cm with a ΛCDM cosmology ($H_0 = 67.3\,\mathrm{km\,s^{-1}Mpc^{-1}}$, $\Omega_m = 0.315$, $\Omega_\Lambda = 0.685$ (Planck Collaboration 2014).

In order to reduce the GROND data, I used a IRAF/PyRAF (Tody 1993) based pipeline (Yoldaş et al. 2008; Krühler et al. 2008). The error bars include the statistical error of the photometry, and the statistical and systematic error of the calibration.

UVOT photometry was carried out on pipeline processed sky images downloaded from the Swift data center [1] following the standard UVOT procedure (Poole et al. 2008). Source photometric measurements were extracted from the UVOT early-time event data and later imaging data files using the tool UVOTMAGHIST (v1.1) [2].

Before fitting, GROND and UVOT magnitudes were corrected for galactic foreground extinction with an $E(B - V) = 0.04$ mag towards the direction of the burst (Schlegel et al. 1998), and using the Cardelli-Clayton-Mathis (CCM) law (Cardelli et al. 1989) with $R_V = 3.08$. For this individual GRB the GROND SED does not indicate significant host extinction nor host flux contribution ((Greiner et al. 2011; Schady et al. 2012) and Sec. 3.3.1).

The Swift/XRT spectra (level 2 data products) were downloaded from the online repository (Evans et al. 2009) and were processed as I will later describe in Sec. 3.3.1 and Sec. 3.3.6.

---

[1] www.swift.ac.uk/swift_portal

[2] The reduced UVOT data was provided by Patricia Shady, who acknowledges support through the Sofja Kovalevskaja Award from the Alexander von Humboldt Foundation of Germany.

3.3. Analysis

3.3.1. Phenomenological Analysis

I describe the afterglow by Eq. 2.33

$$F(\nu, t) \propto t^{-\alpha}\nu^{-\beta}$$

The XRT light curve does not show any flares, breaks or phases with a shallow decay $\alpha \lesssim 1/4$ (plateau phase). All the models I include in my analysis assume single strictly decelerating adiabatic blast waves, thus would not be capable of reproducing such plateau phases. The light curve is best fitted by a single power law with $\alpha_{xrt} = 1.43 \pm 0.01$ and a reduced $\chi^2 = 1.33$. Using a smoothly broken power law does not improve the fit.

The optical/NIR band light curves from GROND do not show any flares either, but have a slight curvature. I fit them with a smoothly broken power law. The 7 light curves share their slopes $\alpha_{1,\text{GROND}} = 0.57 \pm 0.03$ and $\alpha_{2,\text{GROND}} = 1.39 \pm 0.02$, the break time $t_{\text{break}} = 28 \pm 1\,\text{ks}$ and the smoothness $s = 2.4 \pm 0.3$ with a reduced $\chi^2 = 0.38$.

In order to find the optical and X-ray spectral slopes I pick fixed intervals in time and fit the combined GROND (already corrected for galactic extinction) and XRT data in these intervals.

For the XRT spectra, I integrate all counts over a time range $2.8 \times 10^3\,\text{s}$ to $9.8 \times 10^4\,\text{s}$ after the trigger. A constant hardness ratio of the XRT data (Evans et al. 2009) justifies the assumption that the shape of the spectrum does not change in time. To make sure this assumption is correct, I fitted the spectrum of each XRT pointing with a single power law + galactic absorption + host absorption, and found the slope of that power law β to be constant (see Tab. 3.3).

Afterwards I re-normalize the flux of the integrated spectrum to the flux of the XRT light curve at the time of the individual GROND observation.

Finally, I use Xspec (Arnaud 1996) and fit a broken power-law + galactic absorption + host absorption + host extinction to each individual SED.

Extinction and absorption

For the extinction I use the zdust model, which describes the extinction as

$$A(V) = E(B - V) \times R_V \tag{3.1}$$

with

- Extinction $A(V)$
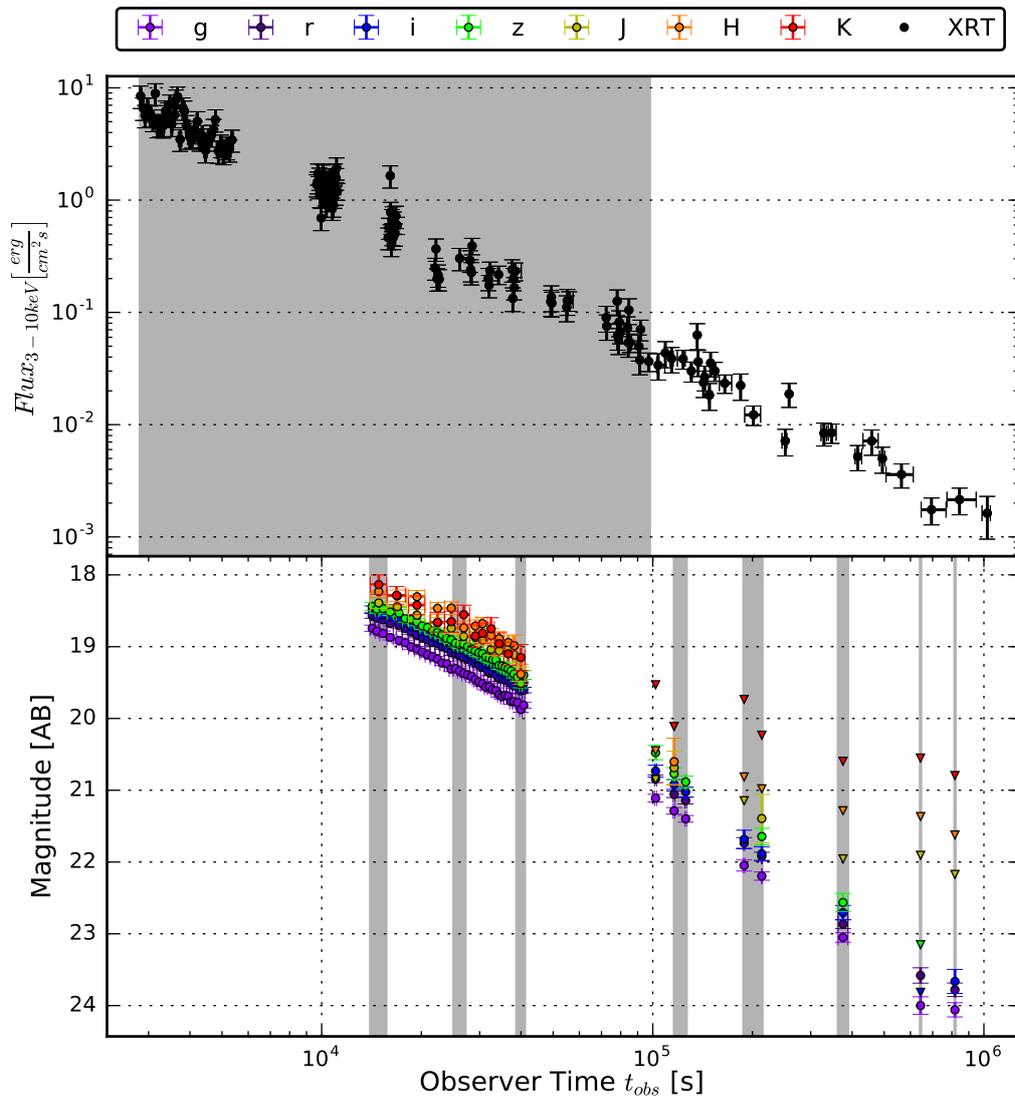
Figure 3.1.: XRT light curve (top) and GROND light curve (bottom). The shaded areas correspond to the time slices of the snap-shot analysis.

- Color excess $E(B - V)$

- Ratio of total to selective extinction R_V, which depends if a Milky Way (MW), Small Magellanic Cloud (SMC) or Large Magellanic Cloud (LMC) profile is assumed.

The ZDUST model is based on the tables given in Pei (1992).

The absorption is modeled by the PHABS respectively ZPHABS model

$$M(E) = exp(-n_{\mathrm{H}}\sigma(E \times (1 + z)))$$ (3.2)

with

- The equivalent hydrogen column density $-n_{\mathrm{H}}$

- The photoelectric cross section σ

- The redshift z

Under the assumption that the electron distribution index p is constant during the fireball expansion, I link the spectral slopes β of all SEDs but allow the break and the normalization of the broken power law to differ between the individual SEDs. I only allow a $\Delta\beta = 0.5$ between the two spectral power law slopes (Sari et al. 1998).

I find $\beta_{\mathrm{GROND}} = 0.43^{+0.03}_{-0.01}$ and $\beta_{\mathrm{XRT}} = 0.93^{+0.03}_{-0.01}$ with a reduced $\chi^2 = 0.8$.

In Fig. 3.2 one can see the SED snapshots including the fitted power laws, in Tab. 3.1 the times of the GROND temporal slices and the position of the spectral break are shown. I tried to fit the temporal evolution with a power law $\nu \propto t^{v_\nu}$, but it clearly does not follow a strict power law as predicted by some of the models I discuss later (see Fig. 3.3).

3.3.2. Physical Implications of the Closure Relations

In this section I test the models described by closure relations collected by Racusin et al. (2009) (not accounting for energy injection) and an analytical model for a fully adiabatic ultra-relativistic spherical fireball in an ISM (Model A, see Tab.3.2).

I can not make a statement whether the spectral break seen in Fig. 3.2 is the cooling break ν_c or the main break ν_m. While Model A predicts a $\nu_c \propto t^{-1/2}$ and a $\nu_m \propto t^{-3/2}$, the temporal evolution of the observed break frequency does not follow a power law (see Fig. 3.3).

From the theoretical spectral shape (see Tab. 3.2) and the β values from Sec. 3.3.1, I can examine values for p. Assuming a slow cooling case, I get a $p = 1.86^{+0.02}_{-0.06}$ from the optical slope and the X-ray slope. Assuming a fast cooling case the optical slope
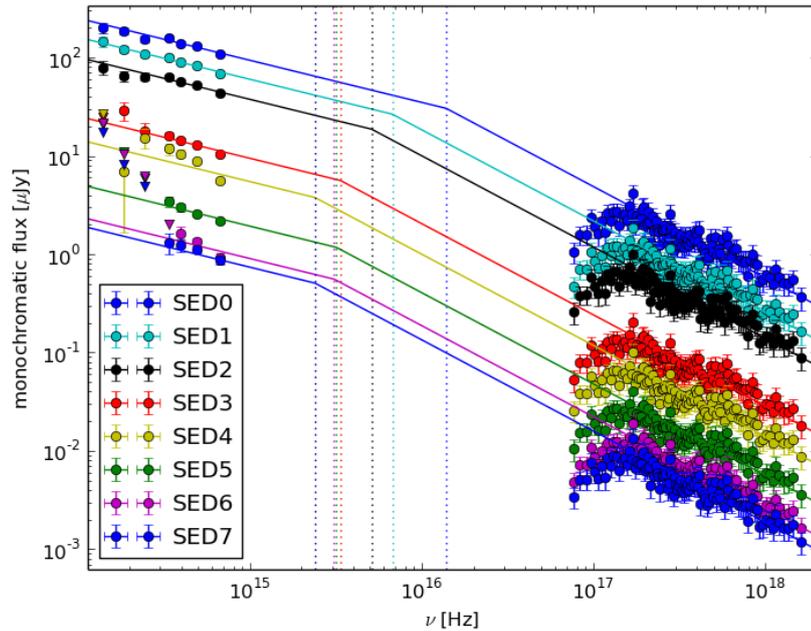
Figure 3.2.: Power law fits to SED snap shots: The power laws share their slopes, but have an individual normalization and break frequency.

is slightly smaller than the theoretical value of $\beta = -0.5$ and from the X-ray slope follows also $p = 1.86^{+0.02}_{-0.06}$.

In Fig. 3.4 I show the closure relations collected by Racusin et al. (2009) (just with impulsive energy injection). Before the temporal break (where $\alpha_{\text{GROND}} = 0.57$) two closure relation are consistent with the measured values for the optical and X-ray regimes

- CR1: ISM, slow cooling, isotropic outflow, with observed frequencies ν is between ν_m and ν_c and

- CR14: wind, uniform spreading jet, with observed frequency $\nu > \nu_c$,

After the break (where $\alpha_{\text{GROND}} = 1.39$) I find one closure relation that is consistent, but just for the optical regime

- CR11: ISM, uniform jet, non-spreading, observed frequency ν between ν_m and ν_c

For the optical the transition $CR1 \rightarrow CR11$ seems plausible, since the jet behavior of the jet just becomes apparent at late times. The transition $CR14 \rightarrow CR11$, however, is unlikely. I also see that there is no consistent picture for both spectral regimes, optical and X-ray, together.

Table 3.1.: Summary of the snap shot analysis. The break is moving towards the low energy part of the spectrum. As a result of a degeneracy between the spectral slopes and the break position not all break frequencies have good constraints.

SED id	time [ks]	break [Hz]
SED0	14	$2^{+2}_{-2} \times 10^{16}$
SED1	26	$8.9^{+8.9}_{-0.5} \times 10^{15}$
SED2	39	$6.2^{+1.9}_{-0.9} \times 10^{15}$
SED3	121	$3.6^{+1.0}_{-0.5} \times 10^{15}$
SED4	201	$2^{+2}_{-2} \times 10^{15}$
SED5	375	$3.3^{+0.3}_{-0.3} \times 10^{15}$
SED6	643	$3.2^{+0.3}_{-0.3} \times 10^{15}$
SED7	817	$2^{+2}_{-2} \times 10^{15}$

Table 3.2.: Model A: Outline of an afterglow model with a fully adiabatic ultra-relativistic spherical fireball in an ISM (Sari et al. 1998).

	spectral regime	β	α	$\alpha(\beta)$
	Slow cooling			
1	$\nu < \nu_m$	1/3		
2	$\nu_m < \nu < \nu_c$	-(p-1)/2	3(1-p)/4	$\frac{3}{2}\beta$
3	$\nu_c < \nu$	-p/2	(2-3p)/4	$\frac{1+3\beta}{2}$
	fast cooling			
4	$\nu < \nu_c$	1/3		
5	$\nu_c < \nu < \nu_m$	-1/2	-1/4	-1/4
6	$\nu_m < \nu$	-p/2	(2-3p)/4	$\frac{1+3\beta}{2}$
ν_c	$= 2.7 \times 10^{12} \epsilon_B^{-3/2} E_{52}^{-1/2} n_1^{-1} t_d^{-1/2} \mathrm{Hz}$			
ν_m	$= 5.7 \times 10^{14} \epsilon_B^{1/2} \epsilon_e^2 E_{52}^{1/2} t_d^{-3/2} \mathrm{Hz}$			
F_{peak}	$= 1.1 \times 10^5 \epsilon_B^{1/2} E_{52} n_1^{1/2} D_{28}^{-2} \mu Jy$			
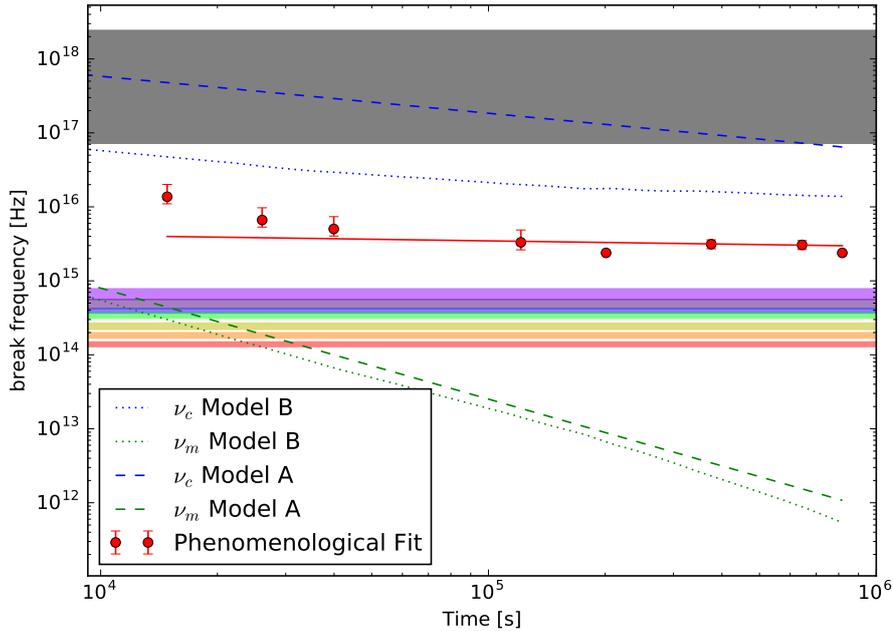
Figure 3.3.: Comparison of the speed of the break movement in the phenomenological fit (red data points + fitted power law). The dotted and dashed lines are ν_c and ν_m from the best fitting models of the Bayesian approach. The horizontal bars correspond to the GROND and XRT bands.

3.3.3. Fitting Hydrodynamical Templates

This afterglow model (Model B) is based directly on hydrodynamical simulations (van Eerten et al. 2010a,b) that cover the jet dynamics in more detail than the standard asymptotic analytical approaches, opening the new possibility to constrain the observer angle (Ryan et al. 2015). The BM solution for the fluid dynamical treatment of an ultra-relativistic spherical blast wave is used as initial condition, the evolution to the late self-similar non-relativistic stage is modeled with numerical hydro-dynamical 2D-simulations of the outflow. For a given jet opening angle θ_0, isotropic kinetic equivalent energy $E_{\rm iso}$ and circumburst medium density n_0 a simulation run takes days to weeks.

Based on the output of the hydrodynamical simulations, a radiative transfer code calculates the emission characteristics under an observer angle $\theta_{\rm obs}$ with luminosity distance d_L (respectively redshift z) for a given set of micro-physical parameters (electron power law distribution slope p, fraction of energy in the magnetic field ϵ_B, fraction of energy in electrons ϵ_e, and fraction of accelerated electrons ξ_N).

The crucial part of fitting simulations to data is to pre-calculate the whole process for a given set of parameters $\Theta = \{E_{\rm iso}, n_0, \theta_0, \theta_{\rm obs}, p, \epsilon_e, \epsilon_B, d_L, z\}$ and compress the data in a way that the results are accessible from every iteration step of the fitting process, within milli-seconds. The results are stored in tables $\mathfrak{f}_*(\tau, \theta_0, \theta_{\rm obs})$ of the
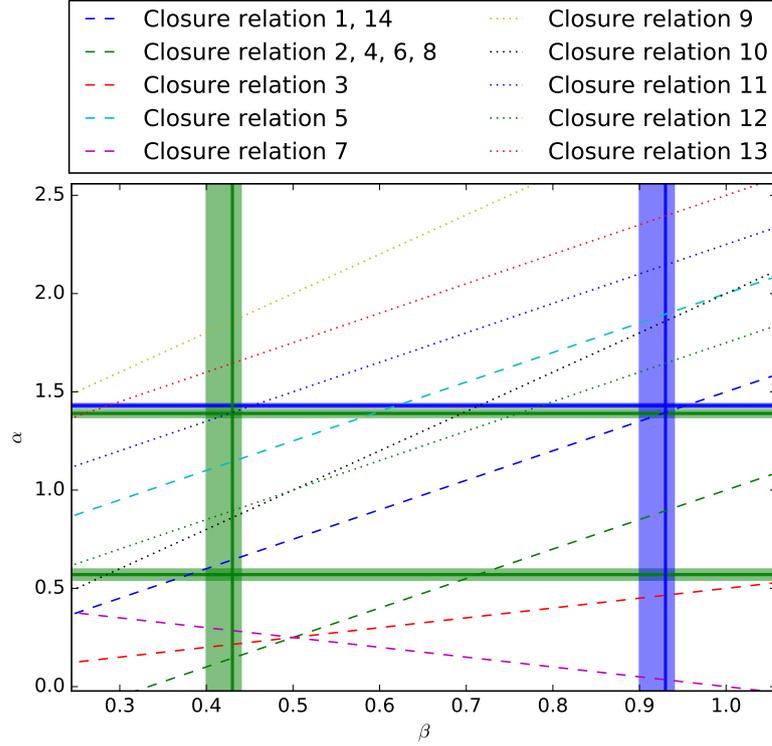
Figure 3.4.: Test of the closure relations collected by Racusin et al. (2009). The dotted lines are the theoretically expected dependencies $\alpha(\beta)$ for different scenarios and spectral regimes. The horizontal bars are the temporal slopes α of the afterglow (green for GROND, blue for XRT). The vertical bars are the spectral slopes β.

time evolution for characteristic quantities for the afterglow SED: cooling frequency ν_c, main frequency ν_m and peak flux F_{peak}. These quantities are stored in arbitrary units, then can be re-scaled using scaling relations (van Eerten & MacFadyen 2012a).

$$F_{\text{peak}} = \frac{1+z}{d_L^2} \frac{p-1}{3p-1} E_{\text{iso}} n_0^{1/2} \epsilon_B^{1/2} \xi_N \qquad \times \mathfrak{f}_{\text{peak}}(\tau, \theta_0, \theta_{\text{obs}}) \qquad (3.3)$$

$$\nu_m = \frac{1}{1+z} \left(\frac{p-2}{p-1}\right)^2 n_0^{1/2} \epsilon_e^2 \epsilon_B^{1/2} \xi_N^{-2} \qquad \times \mathfrak{f}_m(\tau, \theta_0, \theta_{\text{obs}}) \qquad (3.4)$$

$$\nu_c = \frac{1}{1+z} E_{\text{iso}}^{-2/3} n_0^{-5/6} \epsilon_B^{-3/2} \qquad \times \mathfrak{f}_c(\tau, \theta_0, \theta_{\text{obs}}) \qquad (3.5)$$

where $\mathfrak{f}_{\text{peak}}$, $\mathfrak{f}_m$ and $\mathfrak{f}_c$ are the tables and $\tau = \left(\frac{n_0}{E_{\text{iso}}}\right)^{1/3} \frac{t_{\text{obs}}}{1+z}$ is the scaled time after trigger.

Since the model assumes synchrotron radiation as the emission process, the SED is just a series of connected power laws, separated by the characteristic frequencies ν_m and ν_c, with slopes also following the relations Tab. 3.2.

Modelling the whole time evolution of the SED (starting with the BM solution, respectively at the deceleration phase) means, that I can use data from every spectral

regime at every point in time. There is no need for synchronous data from different instruments or interpolations. I can use the not time synchronous photometric data from Swift/UVOT and GROND, and mix it with spectral data from Swift/XRT. Moreover, I do not have to make a guess which spectral regimes are covered by the data.

On the other hand I have to assume a specific scenario beforehand, since the evolution of ν_c, ν_m and F_{peak} depends on the assumptions about e.g. the circumburst density profile and the structure of the jet. Choosing a certain evolution of the characteristic quantities corresponds to fitting a specific set α and β of closure relations.

3.3.4. Parallel Tempered Markov Chains

The goal of any MCMC algorithm is to sample the Posterior Probability Distribution (PDF) $P(\Theta|D)$ (the probability of the parameter set Θ given the data D), defined over the Bayes theorem

$$P(\Theta|D) = \frac{P(D|\Theta)P(\Theta)}{P(D)} \tag{3.6}$$

In the *prior* $P(\Theta)$ the knowledge about the parameter distribution is encoded. Not knowing anything beforehand, I use a flat prior. The *model evidence* $P(D)$ corresponds to a normalization of the PDF, which I set to unity. $P(D|\Theta) = \mathcal{L}$ is the *likelihood*. I assume Gaussian, independent errors in my data and therefore the log-likelihood is

$$ln(\mathcal{L}) = -0.5\chi^2 = -0.5 \sum \left(\frac{x_{\text{Data}} - X_{\text{Model}}}{\sigma_{\text{Data}}} \right)^2 \tag{3.7}$$

with the data points x_{Data}, its uncertainties σ_{Data} and the model X_{Model}.

An instance that explores the parameter space is called a *walker*. For each *step* a new position, drawn from a transition distribution, is proposed to the walker. The probability to accept that new position depends on the likelihood. The sampling speed will increase with the number of walkers in an ensemble. I use *parallel tempering*, meaning that the walker can swap between different modes, corresponding to a *temperature T*. Each mode has its own modified likelihood $P(D|\Theta)^{1/T}$, respectively its own posterior. $T \to \infty$ represents the prior, $T = 1$ represents the true posterior and is the only one used later in the analysis. The higher temperatures allow higher mobility of the walkers and prevent them from getting stuck in local minima. All steps performed during the *burn-in phase* are ignored, so the initial position of the walkers does not bias the sampled PDF (see Fig. 3.5).

3.3.5. My contributions to SCALEFIT

The loading of the hydro-dynamical templates and the MCMC sampling is implemented in the SCALEFIT package (Van Eerten, in prep.; Ryan et al. 2015). The package uses the EMCEE sampler (Foreman-Mackey et al. 2013) to create parallel tempered Markov Chains. It was already successfully applied to single band XRT light curves by Ryan et al. (2015).

I use SCALEFIT for the first time with broad-band data. The package is a provided as a PYTHON class, and I wrote an interface to load multi-band data (especially from GROND) in a convenient and reproducible way: GRONDFIT.PY. The user gives all parameters for the sampling process, the location of the data, and the physical prior as an ASCII file. GRONDFIT.PY then takes care of loading the data, the sampling/fitting, and presentation of the results.

Moreover I expanded SCALEFIT with an additional model (Model A), and a modified likelihood to include upper limits [3].

Additional functionality to interactively plot the fitting results, and extrapolate them to later times is implemented in the script GRONDPREDICT.PY.

3.3.6. Fitting SED Evolutions

Unlike in Sec. 3.3.2 I now use SCALEFIT to fit physical models, instead of describing the data phenomenologically and interpret them afterwards. While the fitted values α and β have to be interpreted in terms of closure relations, and do not have to be necessarily consistent or physically meaningful, I now fit physical parameters directly and limit the fitting space by a physically meaningful prior. Moreover, I fit SED evolutions instead of snap-shots, which means I do not depend on time-synchronous data, but can use data from every point in time, at every point in spectral space.

Instead of re-scaling the whole XRT spectra I create one spectrum for each XRT pointing and correct them for host absorption in the following manner. I fetch the spectra (time integrated according to Tab. 3.3) from the Swift online repository (Evans et al. 2009). Then I re-bin each spectrum with the GRPPHA task from the FTOOLS[4] package using minimum 20 counts per spectral bin. Afterwards I use XSPEC (Arnaud 1996).

Under the assumption that no characteristic frequency crosses the XRT band (see Sec. 3.3.1: constant hardness ratio and consistent spectral slope β for each individual

---

[3]I also included a model using energy injection and another model including an analytical jet-break. Those two models are not properly tested and will not be used in this thesis. Moreover, I included an additional likelihood to weight different spectral regimes by the number of data points in that regime. This modified likelihood did produce inconsistent results and was therefore omitted.

[4]http://heasarc.gsfc.nasa.gov/ftools/ (Blackburn 1995)
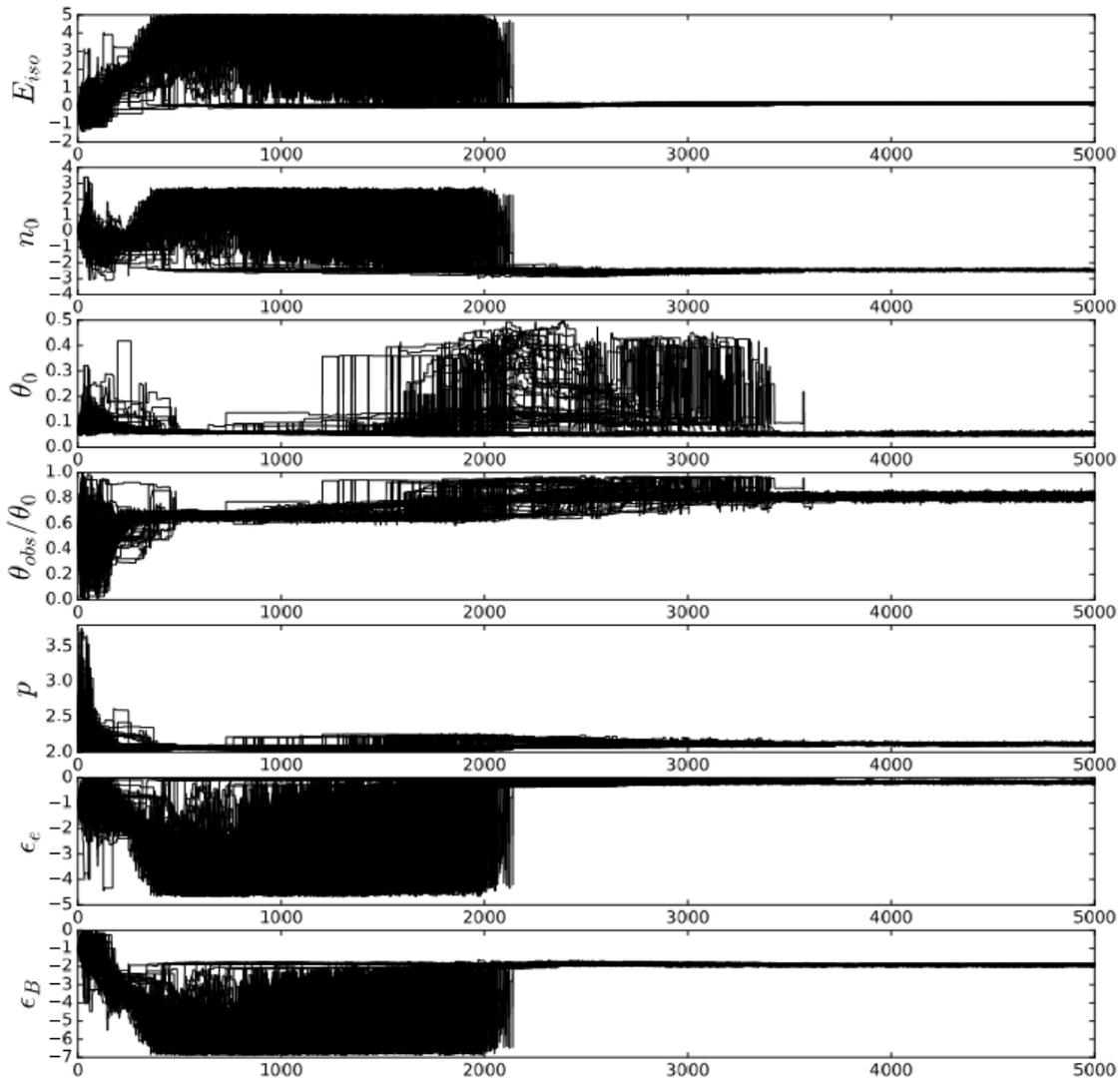
Figure 3.5.: Typical Walker history. The horizontal axis is the step number, the vertical axis is the position of the walker in the direction of the fitting parameter. One can see, that the walkers start at a initial position, then spread out to explore the parameter space. After a certain number of steps, the walkers have converged in the minima of the parameter space (e.g. 2000 steps for ϵ_e, or 3500 steps for θ_0). In this specific case one should pick a burn-in phase of 4000 steps, to make sure the walkers have converged before the sampling phase begins.

Table 3.3.: Time slices of the individual XRT spectra. I subdivided the first two pointings in two time slices, all other spectra correspond to one single XRT pointing. All spectra are in XRT photon counting mode.

Pointing	$t_{\mathrm{start}}[\mathrm{s}]$	$t_{\mathrm{end}}[\mathrm{s}]$	β
00335105000a	2823	6000	$0.78^{+0.11}_{-0.11}$
00335105000b	6000	15700	$0.88^{+0.12}_{-0.12}$
00335105001a	15700	20000	$0.92^{+0.17}_{-0.16}$
00335105001b	20000	40078	$0.89^{+0.17}_{-0.16}$
00335105002	49062	90287	$0.85^{+0.18}_{-0.17}$
00335105003	90430	154632	$0.80^{+0.17}_{-0.16}$
00335105004	158883	173051	na
00335105005	183470	211616	$0.42^{+0.56}_{0.56}$
00335105006	245576	258998	na
00335105007	322114	357846	$0.10^{+0.71}_{-0.78}$
00335105008	408162	530663	$1.24^{+0.72}_{-0.74}$
00335105009	552830	699008	na
00335105010	704555	785700	na
00335105011	791315	872408	na
00335105012	877171	947543	na
00335105013	986972	1045817	na

pointing), I fit a single power law + host absorption + galactic absorption to all spectra at the same time.

With a fixed galactic $N_{H,\mathrm{tot}} = 4.75 \times 10^{20} \mathrm{cm}^{-2}$ (Dickey & Lockman 1990) [5] and a redshift $z = 2.512$ (Berger & Rauch 2008) my fit gives no evidence for host-intrinsic absorption $N_H = (13^{+20}_{-13}) \times 10^{20} \mathrm{cm}^{-2}$, and a power-law slope $\beta_{\mathrm{XRT}} = 0.83^{+0.08}_{-0.08}$. The normalization is fitted to each spectrum individually. Afterwards I correct for absorption effects by distributing the residuals of the fit around the power-law, respectively the un-absorbed spectrum (see Fig. 3.6).

I perform four fits: I fit the Model A given in Sec. 3.2 (free parameters E_{iso}, n_0, p, ϵ_e and ϵ_B), and 4 variants of Model B given in Sec. 3.3.6 (free parameters: E_{iso}, n_0, θ_0, θ_{obs}, p, ϵ_e and ϵ_B) one time with an on-axis observer angle $\theta_{\mathrm{obs}} = 0\,\mathrm{rad}$ and a fixed $\xi_N = 1$, one time with a free θ_{obs} and a fixed $\xi_N = 1$, one time with a free θ_{obs} and ξ_N, one time with a free θ_{obs}, a fixed $\xi_N = 1$, and a fixed $E_{\mathrm{iso}} = 2.7 \times 10^{53}$ erg (Golenetskii et al. 2008), where I used the isotropic energy release in the γ band as a approximation for E_{iso} (Granot et al. 2006).

For the first 4 fits, I find all walkers to be converged after a burn in phase of 5000. A sampling phase of 5000 is more than adequate to sample the posterior distribution function (PDF). A temperature ladder of 20 and 100 walkers have been shown to be reasonable (Ryan et al. 2015). For the fit with the fixed energy I use the same MCMC parameters, but note that the PDF shows fragments and multi-modal

---

[5]http://www.swift.ac.uk/analysis/nhtot/index.php
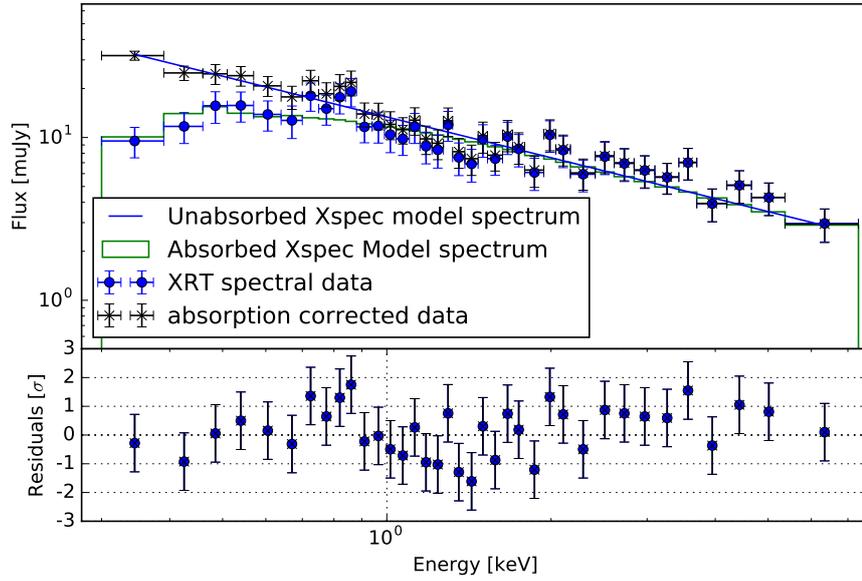
Figure 3.6.: Correction of an XRT pointing for absorption. Top plot: I fit the XRT spectral data (blue dots) with a power law + absorption model (green histogram), using XSPEC. Afterwards I distribute the residuals around the fitted power law (blue line). The absorption corrected data (black crosses) is used to fit SED evolution. Bottom plot: The blue points are the residuals between the measured XRT spectrum and the power-law + absorption model, the crosses are the residuals between the corrected spectrum and that power-law.

behaviour. All fitting results and the prior can be seen in Tab. 3.4. The PDFs are shown in Fig. 3.7, Fig. 3.8, Fig. 3.9, Fig. 3.10 and Fig. 3.11. The light curve of the best walker (the parameter set with the highest likelihood) from the simulation based model with a free ξ_N and a free E_{iso} is shown in Fig.3.12.

Table 3.4.: Summary of the fitting results. The parameters without error bars are not constrained, therefore the uncertainties can not be quantified and the shown value is position of the best walker. The parameters with a given error are constrained. The given values are the marginalized median of the parameter, the errors are the 0.84 quantiles, corresponding to the 68% confidence intervals. The PDF of all fits can be seen in Fig. 3.7, Fig. 3.8, Fig. 3.9, 3.10 and 3.11

Parameter	Model A	Model B	Model B	Model B	Model B	prior
PDF	Fig. 3.7	Fig. 3.8	Fig. 3.9	Fig. 3.10	Fig. 3.11	
$E_{\mathrm{iso}}[10^{53}erg]$	1.0	$9.5^{+0.3}_{-0.3} \times 10^{-1}$	$1.34^{+0.06}_{-0.05}$	3.0×10^{4}	2.7 (fixed)	$[10^{-5}, 10^{5}]$
$n_0[cm^{-3}]$	2.462×10^{-3}	$3.5^{+0.5}_{-0.3} \times 10^{-3}$	$3.5^{+0.3}_{-0.2} \times 10^{-3}$	8.0×10^{1}	6.2×10^{-3}	$[10^{-5}, 10^{5}]$
$\theta_0[rad]$	-	$4.6^{+0.2}_{-0.2} \times 10^{-1}$	$5.0^{+0.3}_{-0.2} \times 10^{-2}$	$5.0^{+0.3}_{-0.2} \times 10^{-2}$	4.5×10^{-2}	$[0.045, 0.5]$
$\theta_{\mathrm{obs}}/\theta_0$	-	0 (fixed)	$8.1^{+0.1}_{-0.1} \times 10^{-1}$	$8.1^{+0.1}_{-0.1} \times 10^{-1}$	9.4×10^{-1}	$[0,1]$
p	$2.508^{+0.006}_{-0.005}$	$2.30^{+0.01}_{-0.01}$	$2.12^{+0.01}_{-0.01}$	$2.11^{+0.01}_{-0.01}$	2.23	$[2,4]$
ϵ_e	3.751×10^{-1}	$4.6^{+0.1}_{-0.1} \times 10^{-1}$	$6.6^{+0.5}_{-0.4} \times 10^{-1}$	3.0×10^{-5}	3.9×10^{-1}	$[10^{-10}, 0]$
ϵ_B	1.446×10^{-2}	$7.4^{+0.5}_{-0.5} \times 10^{-3}$	$1.20^{+0.08}_{-0.08} \times 10^{-2}$	5.4×10^{-7}	4.1×10^{-3}	$[10^{-10}, 0]$
ξ_N	-	1(fixed)	1 (fixed)	4.5×10^{-5}	1 (fixed)	$[10^{-9}, 0]$
χ^2/dof	7.5	4.0	2.8	2.8	3.3	
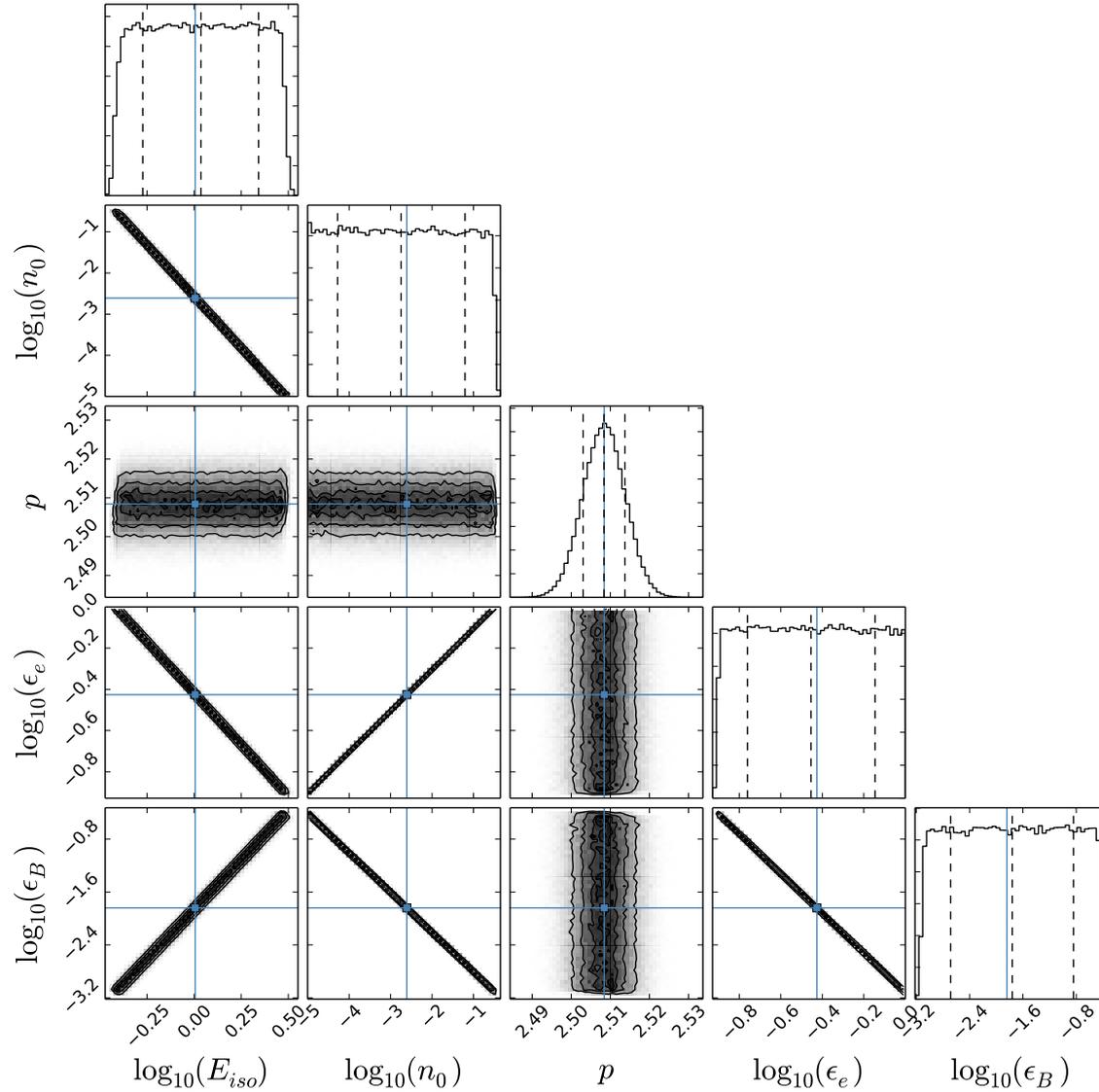
Figure 3.7.: PDF of the MCMC for Model A: E_{iso} is given in units of 10^{53} erg, n_0 is given in cm^{-3}, θ_0 in radians. All other parameters are dimensionless. (The PDF was visualized with TRIANGLE_PLOT by Foreman-Mackey et al. (2014)). ϵ_e, ϵ_B, n and E_{iso} are degenerate. I can constrain p.

3.4. Discussion

3.4.1. Snap Shot Analysis

I have measured the temporal and spectral slopes of the afterglow and tried to interpret it using closure relations. The X-ray data is consistent with closure relation (CR from now) 1 (ISM, slow cooling, isotropic outflow, with observed frequencies ν is between ν_m and ν_c) and CR14 (wind, uniform spreading jet, with observed frequency $\nu > \nu_c$). The optical data has a break in the light curve, therefore I have two different values for α. The optical also is consistent with CR1 and CR14 before
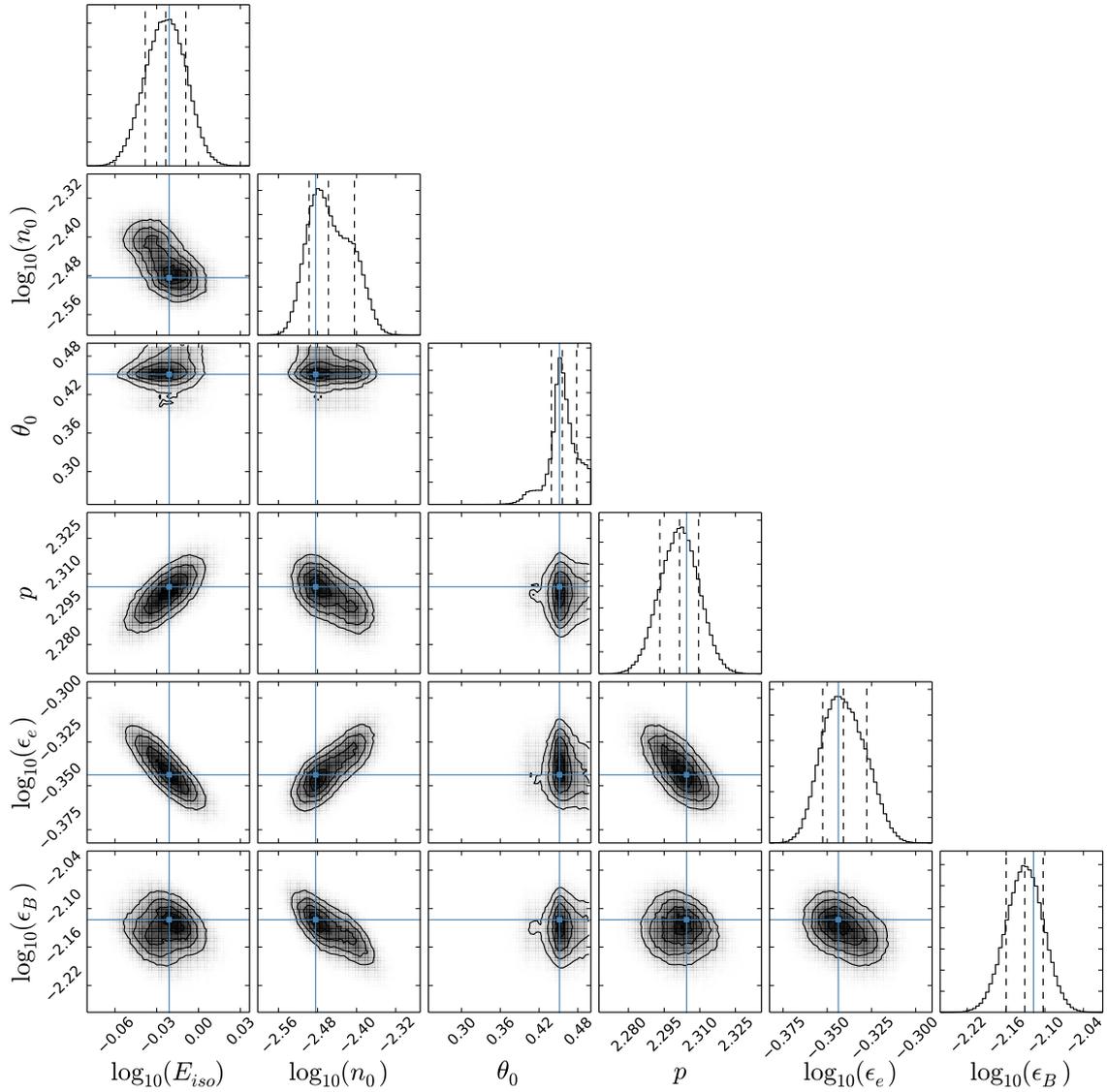
Figure 3.8.: PDF of the MCMC for Model B with a $\xi_N = 1$: $E_{\rm iso}$ is given in units of 10^{53} erg, n_0 is given in cm^{-3}, θ_0 in radians. All other parameters are dimensionless. All fireball parameters are constrained.

the temporal break in the light curve. Afterwards it is consistent with CR11 (ISM, uniform jet, non-spreading, observed frequency ν between ν_m and ν_c).

Having a look at the optical alone, a transition from CR1 $\rightarrow$ CR11 seems a plausible scenario, since the jet character of the relativistic outflow becomes apparent just at late times, while it decelerates. However, this transition is not seen in the X-rays. The transition CR14 $\rightarrow$ CR11 does not make any physical sense. I do not observe the indicated frequency crossing, and such a discrete transition from wind to ISM is somewhat doubtful.

While the closure relations are easily applicable to single snap shots or single optical regimes, I am not able to form a consistent picture of the whole SED evolution of the burst. The limitations of this kind of analysis are obvious: For a less richer data
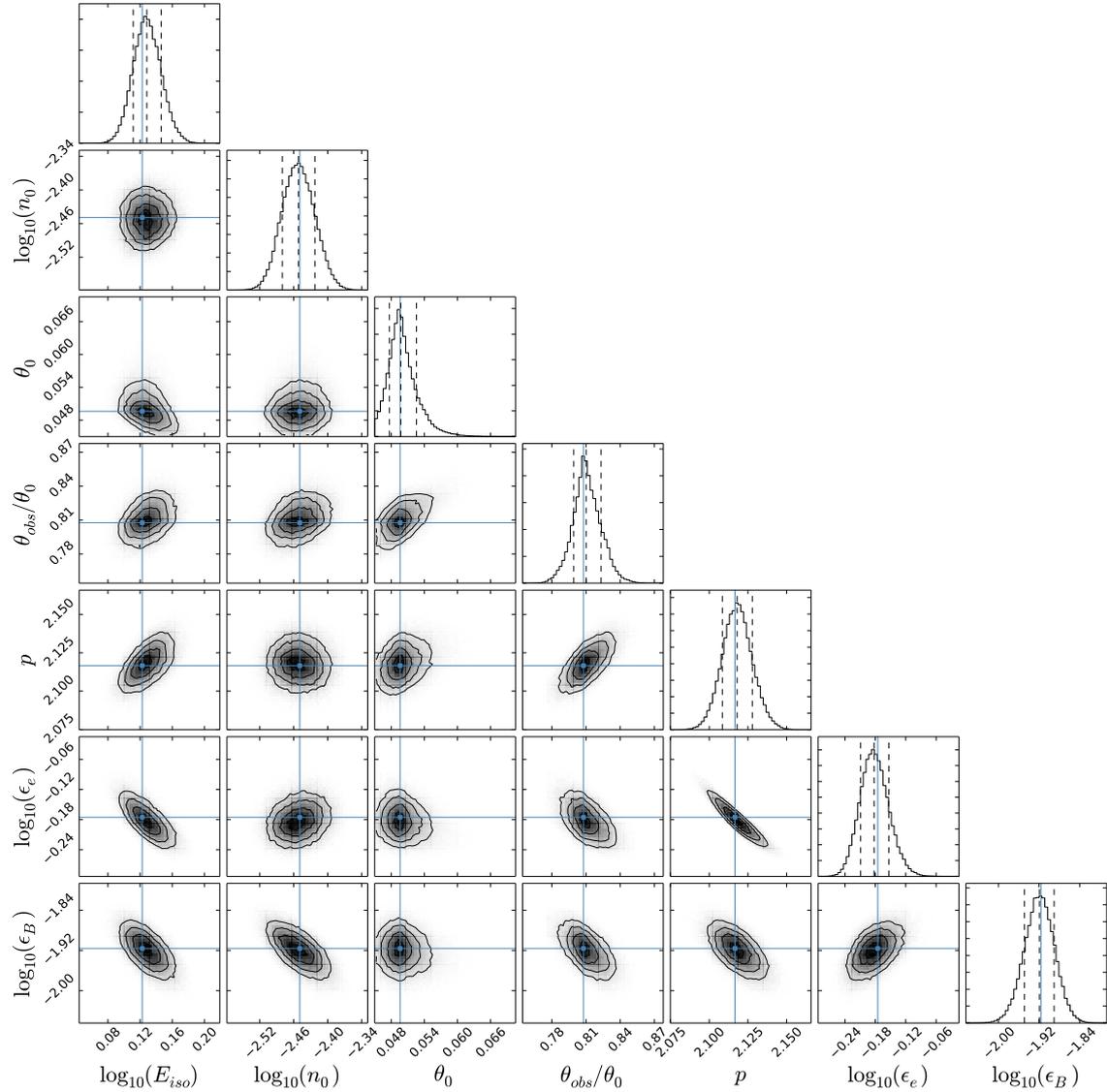
Figure 3.9.: PDF of the MCMC for Model B with a $\xi_N = 1$: E_{iso} is given in units of 10^{53} erg, n_0 is given in cm^{-3}, θ_0 in radians. All other parameters are dimensionless. All fireball parameters are constrained.

set, with just single band observations or single snap-shots, there would be a clear danger of over-interpreting the reliability of the results of this method. Moreover, with a snap shot analysis I am not even able to determine the fireball parameters. I only can put constrains on p over the spectral shape of the afterglow.

3.4.2. SED Evolution Fitting

With the Bayesian approach and SED evolution fitting I am able to have a closer insight into the PDF of all parameters. The price I pay is that I have to choose a certain scenario (a specific set of closure relations) beforehand. Model A and Model B assume an ISM case, which is in agreement with closure relation 1 and 11 from the test above. While Model A is just asymptotically valid for an ultra-
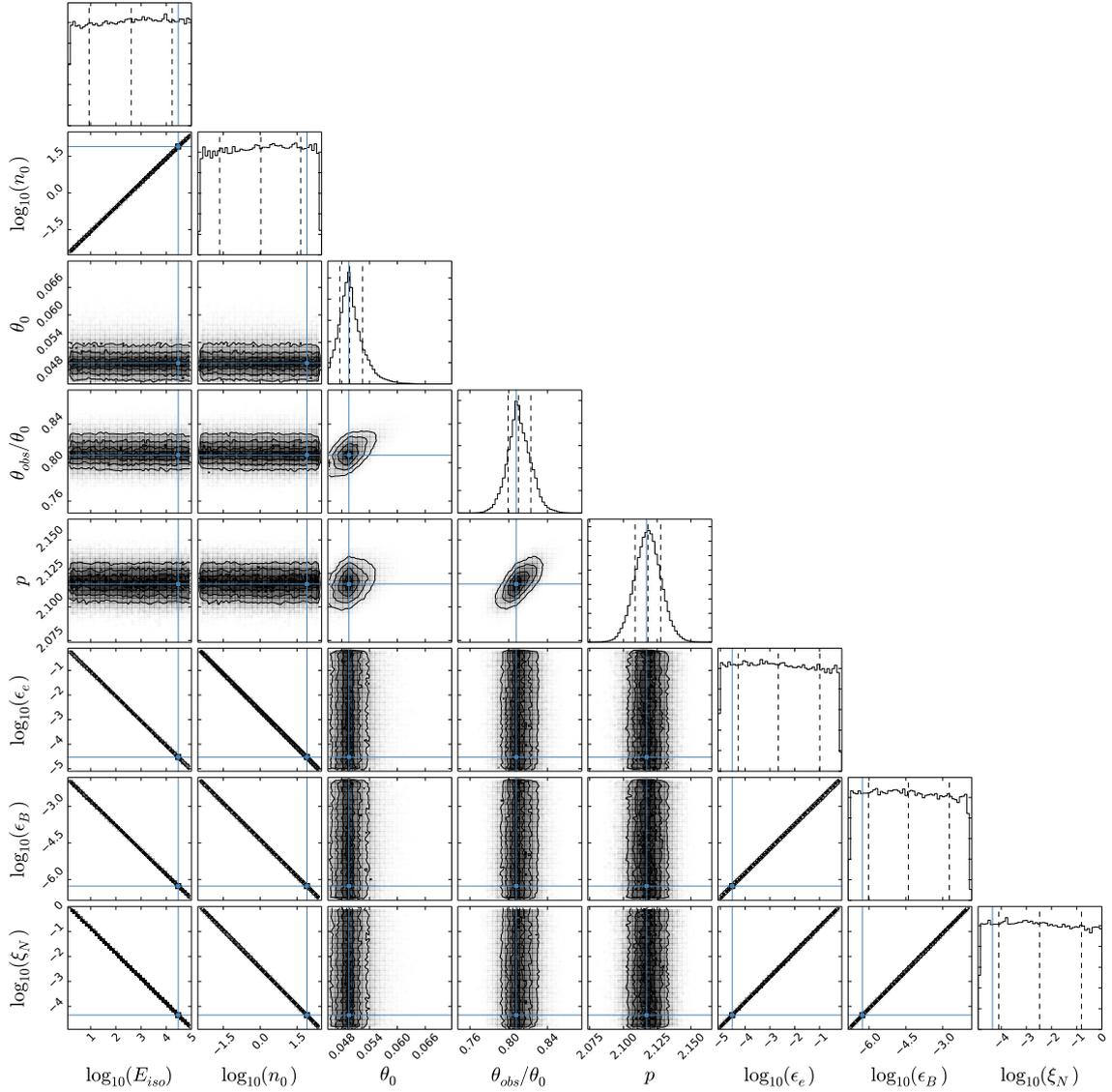
Figure 3.10.: PDF of the MCMC for Model B with a free ξ_N: E_{iso} is given in units of 10^{53} erg, n_0 is given in cm^{-3}, θ_0 in radians. All other parameters are dimensionless.

relativistic spherical outflow, Model B bases on a detailed 2 dimensional hydrodynamical simulation of a jet evolving from an ultra-relativistic state to a Newtonian state.

Fit 1: Model A

For Model A I find intervals for the parameters $\log_{10}(E_{\mathrm{iso}}) \in [-0.25, 0.50]$, $\log_{10}(n_0) \in [-5, -0.5]$ (where the lower limit is given by the prior), $\log_{10}(\epsilon_e) \in [-1, 0]$ (upper limit given by prior), and $\log_{10}(\epsilon_B) \in [-3.2, 0]$ (upper limit given by prior). $p = 2.508^{+0.005}_{-0.005}$ is constrained by the MCMC fit, but inconsistent with the value derived from the snap-shot analysis.

With ξ_N is assumed to be 1, and p derived directly over the spectral shape of the SED, there are 4 degrees of freedom E_{iso}, n_0, ϵ_e, ϵ_B left. With 3 observables
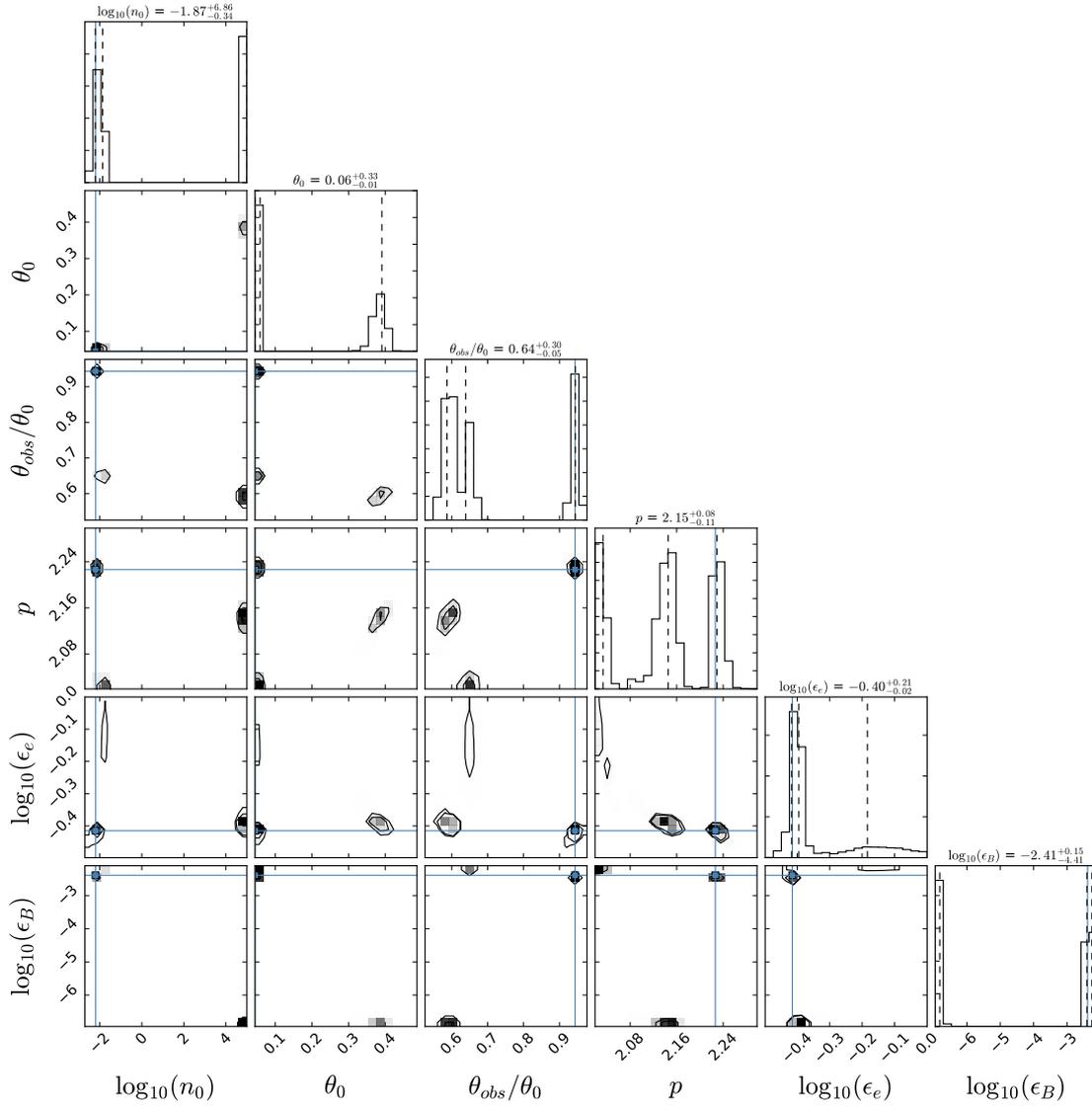
Figure 3.11.: PDF of the MCMC for Model B with a fixed E_{iso}: E_{iso} is given in units of 10^{53} erg, n_0 is given in cm^{-3}, θ_0 in radians. All other parameters are dimensionless. (Visualized with Foreman-Mackey et al. (2014).

ν_m, ν_c and F_{peak} pairwise degeneracies are expected. From the expressions for the observables (Tab. 3.2) I derive

$$n_0 \propto E_{\text{iso}}^{-5}$$
$$\epsilon_e \propto E_{\text{iso}}^{-1} \qquad \epsilon_e \propto n_0^{+1/5}$$
$$\epsilon_B \propto E_{\text{iso}}^{+3} \qquad \epsilon_B \propto n_0^{-3/5} \qquad \epsilon_B \propto \epsilon_e^{-3}$$

Those degeneracies are clearly seen in Fig. 3.7 [6]. A way to break those degeneracies would be the introduction of another observable: The self absorption break ν_a, which corresponds to synchrotron self absorption (Granot et al. 1999) and is observable in the radio and sub-mm regime.

---

[6]With a jet break Eq. 2.31 also implicates $\theta_0 \propto E_{\text{iso}}^{-3/4}$ for an on-axis observation.
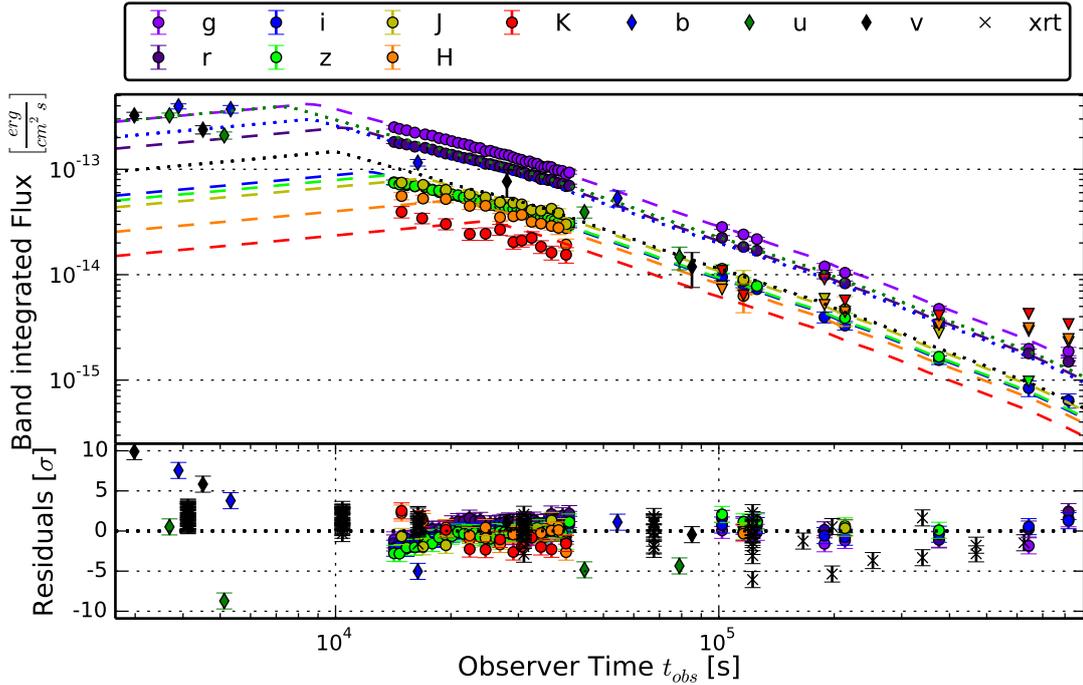
Figure 3.12.: Light curve: The dashed lines are the best fitting model, the error bars of the data points are the 1σ statistical error of the photometry, the statistical error of the calibration and the systematic error of the calibration. The model shows an achromatic break, moving through the optical bands. I find this break to be ν_m crossing the bands. The offset between the data and the model in the first GROND K data points probably results from the discrete spectra of the model. Residual plot: Additionally to the residuals from the light curve (dots for GROND and diamonds for UVOT), the black crosses show the XRT spectral residuals. For every pointing there are multiple spectral bins, therefore multiple black crosses for a single point in time in the residual plot.

Unlike in Sec. 3.3.1, p is not exclusively determined by the spectral shape of the afterglow, but also by the band integrated flux of the light curve at any point in time, which itself depends on the time evolution of ν_m (see Tab. 3.2). Given the high χ^2 and the inconsistent p value, I do not consider this result of Model A trustworthy.

The time evolution of characteristic frequencies on Model A follow a power law, but as can be seen in Fig. 3.3 the time evolution of the break in the SED does not. This specific model does not seem to capture the afterglow phenomenology of GRB 081121A. It may base on the wrong assumptions or over-simplify the physical processes involved.

Fit 2: Model B, $\xi_N = 1$, on-axis

A better result is given by the more detailed Model B. With it I can constrain all fireball parameters when I use the common assumption $\xi_N = 1$.

Assuming an-on axis observation (as implicitly is done by Model A), I get consistent values with Model B: $E_{\text{iso}} = 9.5^{+0.3}_{-0.3} \times 10^{52}$ erg and a rather small $n_0 = 3.5^{+0.5}_{-0.3} \times 10^{-3} \text{cm}^{-3}$. $\theta_0 = 4.6^{+0.2}_{-0.2} \times 10^{-1}$ rad, which is in agreement with small values as reported in literature (Ryan et al. 2015; Racusin et al. 2009). $\epsilon_e = 4.6^{+0.1}_{-0.1} \times 10^{-1}$ and $\epsilon_B = 7.4^{+0.5}_{-0.5} \times 10^{-3}$ are comparable to literature values for other GRBs (Panaitescu & Kumar 2002; Yost et al. 2003; Resmi et al. 2005; Chandra et al. 2008; Cenko et al. 2010). And $p = 2.30^{+0.01}_{-0.01}$ is higher than the value derived from the snap-shot analysis.

Fit 3: Model B, $\xi_N = 1$, off-axis

Using Model B and also fitting the observer angle $\theta_{\text{obs}}/\theta_0 = 8.1^{+0.1}_{-0.1}$ I get a marginally higher $E_{\text{iso}} = 1.34^{+0.06}_{-0.05} \times 10^{53}$ erg, and a similar $n_0 = 3.5^{+0.3}_{-0.2} \times 10^{-3} \text{cm}^{-3}$. $\theta_0 = 5.0^{+0.3}_{-0.2} \times 10^{-2}$ rad, however differ by an order of magnitude, which shows clearly how strong the impact of off-axis effects is. $\epsilon_e = 6.6^{+0.5}_{-0.4} \times 10^{-1}$ is similar, and $\epsilon_B = 1.20^{0.08}_{0.08} \times 10^{-2}$ is slightly bigger.

Why do I find unique solutions for the fireball parameters?

In fit 2 and fit 3 all fireball parameters are constrained and have a very narrow distribution. p is mainly given by the spectral shape of the afterglow. The opening and observer angle θ_0 and θ_{obs} are given by the actual shape of the light curve (Ryan et al. 2015), namely when the jet break occurs and how smeared out it is (the curvature of the light curve, see Sec.2.3.1). Unlike as in amalytical models, the temporal evolutions of the characteristic quantities do not follow a strict power law but have a complex shape. This additional information enables us to find values for θ_0 and θ_{obs}, even without a clear jet break.

E_{iso}, n_0, ϵ_e and ϵ_B, however, just scale the light curve, respectively shift it on a logarithmic axis (as Eq. 3.3, 3.4 and 3.5). For those 4 parameters one would expect the same degeneracies as above. Fig. 3.8 and Fig. 3.9 PDFs actually show tilted ellipses but not the wide degeneracies which are just limited by the prior, as in Fig. 3.7.

Since the model light curves have a defined starting point, the beginning of the deceleration phase, and a also a defined ending point, the end of the numerical simulations, the scaling variables E_{iso}, n_0, ϵ_e and ϵ_B have additional constraints, which limit the size of the degeneracies. Moreover, numerical noise in the hydro-dynamical simulations and the radiative transfer code give the degeneracy a noisy substructure with a unique value of maximal likelihood.

Fit 4: Model B: ξ_N free, off-Axis

The assumption $\xi_N = 1$ is a popular assumption in literature, but an electron acceleration efficiency of 100% is somewhat unrealistic. When I use ξ_N as a free fitting parameter I can not constrain E_{iso}, n_0, ϵ_e and ϵ_B, but scale with ξ_N. The limits are $log_{10}(E_{\text{iso}}) > 0$, $log_{10}(n_0) \in [-2, 2]$, $log_{10}(\epsilon_e) > -5$, $log_{10}(\epsilon_B) \in [-6.5, -2.0]$ and $log_{10}(\xi_N) > -5$. The values vary over several orders of magnitude and are just limited by the prior. How the parameters above scale with ξ_N already was discussed by Eichler & Waxman (2005) [7]. They also derive observational radio signatures from the non accelerated electrons. Additional constrains on ξ_N are fundamental to get absolute measures of a GRBs energy budget since E_{iso} also scales with it.

I can constrain the jet's opening angle $\theta_0 = 5.0^{+0.3}_{-0.2} \times 10^{-2}$ rad, the observer angle $\theta_{\text{obs}}/\theta_0 = 8.1^{+0.1}_{-0.1}$ and $p = 2.11^{+0.01}_{-0.01}$. Both angles and p are independent of ξ_N and have the same best fitting values as in the two Model B fits before.

Fit 5: Model B, $\xi_N = 1$, fixed E_{iso}

In this fit I fix $E_{\text{iso}} = 2.7 \times 10^{53}$ erg (Golenetskii et al. 2008), where I used the isotropic energy release in the γ band as a approximation for E_{iso} (Granot et al. 2006). The fixed value of E_{iso} is well outside the found solution from fit 3. I move along the degeneracy away from the value of maximal likelihood, as one can see in the χ^2 value in Tab. 3.4. The PDF becomes noisier due to

- Noise from the hydrodynamical simulations

- Noise from radiative transfer code

- Noise from interpolations in the template tables

In Fig. 3.11 one can see those noise feature showing up.

The maximal likelihood values of θ_0, θ_{obs} and p are consistent with fit 2, 3, and 4 but alternate modes with a high likelihood also show up.

comparison

Model B predicts ν_m crossing the NIR-bands at $t_{\text{cross}} \sim 3 \times 10^4$ s after the trigger. Such a late crossing of an optical or NIR band, rather rare, was already reported by Mundell et al. (2013) for GRB 120308A $t_{\text{cross}} \sim 1 \times 10^3$s in the r band. Zhang et al. (2015b) for GRB 091127A t_{cross} between 2.1×10^4s and 1.1×10^5s (which is a comparable time range to my t_{cross}), and Bardho et al. (2016) for GRB 141221A $t_{\text{cross}} = 9.2 \pm 1.6 \times 10^2$s in the I band.

---

[7]The reader is asked for extra caution, since the use a different definition of ϵ.

The peak flux $F_{\mathrm{peak}}(t, \Theta)$ depends on additional assumptions about the cosmology and acts as an overall normalization of the SED. To check how a different normalization does influence the results, I performed another fit with a free luminosity distance d_L. The resulting PDF shows that E_{iso}, n_0 and ϵ_B scales with d_L, but θ_0, θ_{obs}, p and ϵ_B does not. Most important, the predicted crossing time t_{cross} of ν_m also is independent of d_L.

In another experiment I extrapolate the GROND K band data to earlier times with a power law with the same slope as after $t_{\mathrm{cross}} \sim 1 \times 10^4$s. In this way I force the fitting routine to find a parameter set, where the ν_m crossing does not occur during the temporal range of the data. The result is a multi-modal PDF, implying that the walkers do not converge properly.

A limitation of the used model is that the SED consists of discrete power laws, connected at the characteristic frequencies. In reality the spectral breaks are smooth, as discussed in Granot & Sari (2002). A smooth SED would result in a smoother temporal break in the light curve and decrease the residuals of the fit further.

For the simulation based model I find values for p close to 2, in the snap-shot analysis, even $p < 2$. This rises the problem, that the integral for the kinetic energy of the electrons (see Eq. 2.19) does not converge when $\gamma_{\mathrm{max}} \to \infty$. A high energy cut-off has to be introduced, and the interpretation of ϵ_e has to be reconsidered. The real ϵ_{eTrue} will scale with the fitted ϵ_{eFit}, when I subtract all contributions from the regime $\gamma_e > \gamma_{max}$

$$\epsilon_{e,\mathrm{True}}\, e = K_0 mc^2 \left(\int_{\gamma_{\mathrm{min}}}^{\infty} \mathrm{d}\gamma\ \gamma^{1-p} - \int_{\gamma_{\mathrm{max}}}^{\infty} \mathrm{d}\gamma\ \gamma^{1-p} \right) \tag{3.8}$$

$$\tag{3.9}$$

It follows

$$\frac{\epsilon_{e,\mathrm{True}}}{\epsilon_{e,\mathrm{Fit}}} = 1 - \left(\frac{\gamma_{\mathrm{max}}}{\gamma_{\mathrm{min}}} \right)^{2-p} = 1 - \left(\frac{\nu_{\mathrm{cutoff}}}{\nu_m} \right)^{\frac{2-p}{2}} \tag{3.10}$$

A physically motivated γ_{max} was proposed by Dai & Cheng (2001). They suggested that when the radiative synchrotron loss $\frac{d\gamma}{dt} = \frac{\sigma_T B^2}{6\pi m_e c}\gamma^2$ equals the acceleration time $t = \frac{f}{c} = \frac{Be}{2\pi m_e}\frac{1}{c}$ the maximum Lorentz factor of the electron distribution is

$$\gamma_{\mathrm{max}} = \left[\frac{3e}{\xi_N \sigma_T B} \right]^{1/2} = 3.2e8 \tag{3.11}$$

Another way to bypass the non converging energy integral is given by Granot &

Sari (2002). They generalized the fireball formalism for $p < 2$ with the substitution

$$\bar{\epsilon}_e = \frac{p-2}{p-1}\epsilon_e \qquad (3.12)$$

3.5. Conclusions

GRB081121A is a relatively simple afterglow, characterized by a smoothly curved light curve without any particular feature. Despite this simplicity, the light curve shape allows us to constrain the jet opening angle $\theta_0 = 5.0^{+0.3}_{-0.2} \times 10^{-2}$ rad and the observer angle $\theta_{\rm obs}/\theta_0 = 8.1^{+0.1}_{-0.1}$, without a clear jet break in the data, and independently from knowledge about the other fireball parameters. Those angles and p do not depend on the scaling parameter $E_{\rm iso}$, n_0, ϵ_e and ϵ_B.

The lack of clear jet breaks is a long-standing issue (Racusin et al. 2009). In most analytical models a runaway behaviour is expected since they use a solution for the hydrodynamics in the ultra-relativistic limit. The simulation based model offers a more detailed insight into the dynamics of the relativistic outflow. A "smooth " jet break evolves naturally in those simulations (van Eerten & MacFadyen 2012b).

However, it became obvious how sensible the derived results depend on the used method and the used model. Even a single method (snap-shot analysis) gave back inconsistent results for different subsets of the data (before and after the temporal break). This is somewhat unavoidable since one always deals with incomplete models and imperfect data, but points out the importance to clarify all details and assumptions of an analysis.

3.6. Fitting Models Based on Numerical Simulations: Issues and Outlook

When using models based on numerical simulations one has to keep in mind:

1. *The temporal range of the simulations is limited.* When the data covers a longer time range than the simulations, the model light curve has to be scaled to cover the measured light curve. As a results non-physical constraints are put on the scaling parameters $E_{\rm iso}$, n_0, ϵ_e and ϵ_B. To bypass this issue, a scheme to extrapolate the templates in time is set in place.

2. *An interpolation error when loading the templates from tables does occur.* SCALEFIT uses trilinear interpolation to interpolate between table entries. If an alternative interpolation scheme (e.g. binomial or logarithmic interpolation) will increase the quality of the result is to be tested.

3. *Numerical noise is present in the hydrodynamical simulations.* To minimize the noise resulting from the limited resolution of the hydro-dynamical simulations, a combination of numerical approaches is used: A relativistic adaptive mesh code (RAM, Zhang & MacFadyen 2006) is applied in a lab frame and a Lorentz boosted frame (van Eerten & MacFadyen 2013).

4. *Numerical noise is present in the radiative transfer code.* The number of rays in the radiative transfer code (van Eerten et al. 2012) has to be optimized.

5. *The error of the model has to be quantified.* Unlike an analytical model, a simulation based model always will suffer from numerical noise. For the model used in SCALEFIT the noise in the light curve is estimated to be $\sim 2\%$ (at the time of writing this thesis). While this noise level is negligible for Swift/XRT light curves with an error in flux $\sim 10\%$ as used by Ryan et al. (2015), a fit to optical data with an error $\sim 1\%$ will be influenced. The error in the model will be treated over a modified log-likelihood used by the MCMC sampler.

Those issues will be addressed in the final release of SCALEFIT (Van Eerten in prep.). Additionally a set of templates covering the stellar wind case and smoothed spectra with a self absorption break ν_a will be available in the release version of SCALEFIT.

CHAPTER 4

OPENING ANGLES OF SHORT GRBS

4.1. The Advantages of ScaleFit

Since the first optical detection of an afterglow from a short GRB (Hjorth et al. 2005b), less than 90 short GRB X-ray afterglows have been detected, as compared to around 1000 long GRB afterglows [1]. Short GRBs are generally about a factor of 10-100 less energetic than the more common long GRBs (Ghirlanda et al. 2009) and also have a fainter afterglow (Berger 2007, 2010; Nakar 2007; Gehrels et al. 2008; Nysewander et al. 2009; Kann et al. 2011), which makes follow up observations challenging. Just about 30% of all short GRB afterglows had an optical/near infrared counterpart, and just about 5% had a radio counterpart (Fong et al. 2015).

In chapter 3 I introduced SCALEFIT. This software implements an analysis method based on the modeling of SED evolutions. Modeling the whole SED evolution instead of focusing on single snap-shots opens the possibility to use data from every point in time, at every point in spectral space. Time synchronous data, and extra- or interpolations are not necessary. SCALEFIT (Van Eerten in prep.; Ryan et al. 2015) includes a model based on hydro-dynamical numerical simulations that allows one to derive the jet opening angle θ_0 without a clear jet break and independently from the knowledge of other fireball parameters. Additionally, the model is capable of deriving the observer angle θ_{obs}.

In this chapter I apply SCALEFIT to a sample of short GRB afterglows (Fong et al. 2015). For most short GRB afterglows only sparse data-sets are available, and SCALEFIT promises to be particularly useful since it can use all the available data and does not rely on a well sampled single band light curve (see Sec. 4.3). The authors collected all estimates of short GRB opening angles and expanded them by their own measurements. They used an established method that is based on the

---

[1] http://www.mpe.mpg.de/~jcg/grbgen.html

measurement of the jet break time (Sari et al. 1999; Frail et al. 2001). They list
jet opening angles for 4 GRBs, and for 7 GRBs they list lower limits of opening
angles. I expand the list to 12 measurements and 2 limits of the opening angles and
14 observer angles, by applying SCALEFIT.

4.2. On the Importance of the Jet Opening Angle

The jet opening angle θ_0 dominates the energy budget of a GRB. A typical isotropic
energy output of a GRB would be within a factor of two of the rest-mass energy of
the Sun. In a collimated outflow the kinetic energy of the jet

$$E_{\text{jet}} = (1 - cos\,\theta_0)E_{\text{iso}} \tag{4.1}$$

becomes much more realistic (Frail et al. 2001). Aloy et al. (2005) found that anni-
hilation of neutrino-antineutrino pairs radiated from a hot accretion torus produce
enough energy for a short GRB, if just $\sim 10^{49}$ erg are deposited in a jet with rela-
tively wide $\theta_0 = 0.8$ rad.

Different jet forming mechanisms result in different jet opening angles, therefore
knowledge of the opening angles puts additional constraints on the possible pro-
genitors of GRBs. For long GRBs Zhang et al. (2003) find that relativistic jets
are collimated by their passage through the stellar mantle. Starting with an initial
half-angle of up to 0.3 rad, the jet emerges with half-angles that are around 0.1 rad.
Duffell et al. (2015) did a similar study for short GRBs, where they find that an
initial full opening angle of 1.0 rad can be collimated into 0.1 rad by an expanding
oblate cloud of ejecta. They claim that they expect different opening angles from
double neutron star mergers, than from a neutron star - black hole merger. Murguia-
Berthier et al. (2017) give a maximal $\theta_0 \sim 0.35$ rad for neutron star mergers; wider
jets have to come from neutron star - black hole mergers. Rosswog & Davies (2002);
Rosswog & Ramirez-Ruiz (2003); Rosswog et al. (2003) find that sufficient energy
to explain the observed isotropic luminosities of short GRBs can be obtained by
neutrino annihilation if the outflow is beamed to narrow angles. They argue that
the energetic neutrino-driven wind that accompanies the merger could collimate
the neutrino annihilation driven jet. As a third collimation mechanism serves a
rapidly spinning compact object surrounded by a hot and highly magnetized torus
which amplifies an initially turbulent magnetic field along the spin axis, within a
half-opening angle of ~ 0.5 rad, which may naturally launch a relativistic jet (e.g.
Rezzolla et al. 2011). Others claim that rotation has neither a collimating nor a
de-collimating effect on field lines, suggesting that relativistic astrophysical jets are
not collimated by the rotational winding up of the magnetic field (e.g. Narayan et al.

2007).

Another example for the importance of the jet opening angle of short GRBs are the prospects of coinciding detections of Gravitational Waves (GWs) with a short GRB counterpart by facilities like Advanced LIGO (Aasi et al. 2015) and Advanced VIRGO (Acernese et al. 2015). Short GRBs as a result from a CBM are a source of gravitational waves (Cutler et al. 1993). Gravitational Wave (GW)s are emitted isotropically, but the coincidence rate with a short GRB depends strongly on the jet opening angle (Clark et al. 2015; D'Avanzo & Ghirlanda 2016; Rueda Hernandez et al. 2016).

4.3. The Sample of Fong et al. (2015)

Fong et al. (2015) collected all data from the literature and the GCN about short GRBs which occurred between November 2004 to March 2015, and had prompt follow-up observations in the radio, optical or X-ray. They list 103 short GRBs. 71 of them have X-ray detections, 30 have optical / NIR detections, and 4 GRBs have radio detections. For 34 GRBs are redshifts available.

Despite that most of the short GRBs have a poor data coverage, the authors derive a number of phenomenological and physical properties.

Spectral and Temporal Slopes

Fong et al. (2015) exclude time intervals that contain flares, a plateau or a steepening. The temporal slope of the X-ray data α_X is derived from a light curve fit. The spectral slope of the X-ray data β_X is derived from the X-ray spectrum, when available.

For well sampled filters Fong et al. (2015) fit the optical temporal slope α_o directly. When there are multiple well sampled filters they use an average α_o, under the implicit assumption that no characteristic frequency is crossing the bands. For bursts with multiple optical observations at the same time, they derive the optical spectral slope β_o. For some bursts there is a measurement of β_o but not a well sampled single band light curve. In those cases they extrapolate over spectral space to a single filter, then derive α_o in that filter. For bursts with non-synchronous optical detection in multiple bands, they use α_o and extrapolate in time space to find β_o with the implicit assumption of an undisturbed power-law decay.

Inferred Physical Properties

Besides a phenomenological description, they also give estimates for some physical parameters: Host extinction A_V^{host}, the position of ν_c relative to the X-ray band, the

electron energy distribution index p, the isotropic energy equivalent release in the γ band $E_{\gamma,\mathrm{iso}}$ (using a measurement of the redshift z where available, and assuming $z = 0.5$ elsewhere), the isotropic kinetic energy $E_{K,\mathrm{iso}}$, the circumburst density n_0.

If the optical spectral slope β_o deviates from a single power law they include extinction with a Milky Way extinction profile. If $\beta_o - \beta_x > 0.5$, they also include extinction until the requirement is fulfilled.

They derive p from the temporal slope α_X and the spectral slope β_X of the X-ray separately, using relations from Granot & Sari (2002). They check if the derived p values are consistent within 1σ for $\nu_m < \nu_{\mathrm{X-ray}} < \nu_c$ or $\nu_c < \nu_{\mathrm{X-ray}}$. Then they calculate the weighted mean value for p. In this way they also locate ν_c relative to the 0.3-10 keV X-ray band.

$E_{K,\mathrm{iso}}/n_0$ is modeled with Granot & Sari (2002) and assuming $\epsilon_e = 0.1$ and $\epsilon_B = 0.1/0.01$ (checking what fits better). They fit $E_{K,\mathrm{iso}}/n_0$ for radio, optical and X-ray data separately, then they create a "joint" probability for $E_{K,\mathrm{iso}}$ and n_0 by combining the individual fits. For 2 GRBs they need to decrease ϵ_B further to form a consistent picture.

In this way they find a median circumburst density $<n_0> \approx 2.9 \times 10^{-3} \mathrm{cm}^{-3}$ and a median $<E_{kin,\mathrm{iso}}> = 1.0 \times 10^{51}$ erg, for the whole sample. Throughout the whole paper, they assume a slow cooling case $\nu_m < \nu_c$.

Opening Angles

The opening angles are derived from the presumed jet break of the best sampled light curve (Sari et al. 1999; Frail et al. 2001).

$$\theta_0 = 9.5 t_{\mathrm{jb}}^{3/8}(1+z)^{-3/8} E_{K,\mathrm{iso}}^{-1/8} n_0^{1/8} \deg \tag{4.2}$$

with the jet break time t_{jb}. For light curves without a break, they assume that the jet break occurs after the last detection and derive a lower limit for the opening angle.

Eq. 4.3 is valid for an on-axis observation of a jet in an ISM, with sharp edges, and no structure. It also requires the knowledge of $E_{K,\mathrm{iso}}/n_0$. I want to point out, that $E_{K,\mathrm{iso}}/n_0$ was derived using a spherical model in an ultra-relativistic regime, and that assumptions about ϵ_e and ϵ_B had to be made. The independent measurement in radio, optical and X-ray of $E_{K,\mathrm{iso}}/n_0$ are made at different points in time (not given by the authors).

In a first approximation, a spherical and a jet model behave in principle in the same way before the jet-break. However, numerical studies (van Eerten & Mac-Fadyen 2012b) unveiled that there is a regime of sideways spreading right from the beginning, and that the front of the jet is highly inhomogeneous.

Table 4.1.: Additional data not in Fong et al. (2015). Corrected for galactic extinction.

GRB 140129B			GRB 140930B		
Time [ks]	Flux [μJy]	Band	Time [ks]	Flux [μJy]	Band
2.8	285.5 ± 52.9	v	27.7	1.7 ± 0.1	g
0.60	349.1 ± 64.7	b	27.7	0.39 ± 0.29	r
0.57	697.1 ± 109.6	u	118.4	0.96 ± 0.13	r
0.64	794.9 ± 117.6	uvw1			
0.80	767.9 ± 135.1	uvm2			
0.84	456.4 ± 80.3	uvw2			

I will discuss the opening angle estimates derived with this *classical method*, based on the measurement of the jet break time, while comparing them to the results from my SCALEFIT analysis in Sec. 4.5.2.

4.4. Additional data

I find additional *Swift*/UVOT data for GRB 140129B (Swenson & Bernardini 2014), and add some so far unpublished GROND data for GRB 140930B in our archive. The additional GROND data was reduced with our pipeline (Yoldaş et al. 2008; Krühler et al. 2008). The additional data is listed in Tab. 4.1.

4.5. Analysis

With SCALEFIT I can constrain the opening angle θ_0 using the information of all bands, without extrapolations. Additionally, I can constrain the observer angle θ_{obs}, and I am not limited by the assumption of an on-axis observation. The simulation based model does not lose its validity when the jet of the GRB slows down and leaves the ultra-relativistic regime. Moreover, my analysis using SCALEFIT does not depend on an estimate of $E_{K,iso}/n_0$, which by itself depends on assumptions about ϵ_e and ϵ_B.

Even if I can not constrain E_{iso}, n_0, ϵ_e and ϵ_B in most cases, I do not have to make assumptions about the those parameters, since SCALEFIT marginalizes over unknown parameters. The estimates of θ_0 and θ_{obs} are therefore more reliable.

Method

I use a flat prior for all physical parameters of the fireball model. The limits of the prior are given in Tab. 4.2. Short GRBs often occur at a relative offset to the host galaxies center (Belczynski et al. 2006; Fong et al. 2010; Church et al. 2011; Fong

Table 4.2.: The prior I used for the sampling. The fraction of accelerated electrons $\xi_N = 1$ is fixed.

parameter	lower bound	upper bound	
$E_{\rm iso}$ [10^{53} erg]	10^{-5}	10^{5}	
n_0 [cm^{-3}]	10^{-10}	10^{5}	
θ_0 [rad]	0.045	0.5	(θ_0 is limited by
$\theta/\theta_{\rm obs}$	10^{-10}	1	the range of the simulations)
p	2.0	4.0	
ϵ_e	10^{-10}	1	
ϵ_B	10^{-10}	1	

& Berger 2013; Behroozi et al. 2014), where the circumburst density is expected to be close to the typical value of the Inter Galactic Medium (IGM) $n_0 \sim 10^{-6}$cm^{-3}. I choose a significantly lower bound of n_0 to be on the safe side.

In the majority of the fits I do not include upper limits of flux measurements, but check afterwards if they are consistent with the model. Radio limits I generally take as not trustworthy, since scintillation might affect the detectability of the afterglow in the radio regime during the first days, and there are no data during that time interval. In fits where an optical or X-ray upper limit would impact the result significantly, I re-fit the data using a modified χ^2 in the likelihood

$$\chi^2 = \begin{cases} \sum \left(\frac{x_{\rm Data} - X_{\rm Model}}{\sigma_{\rm Data}} \right)^2 & , {\rm Model} < {\rm Upper\,Limit} \\ \infty & , {\rm Model} > {\rm Upper\,Limit} \end{cases} \tag{4.3}$$

The Golden Sample

The model has 7 degrees of freedom. 26 afterglows have at least 7 detections at various time and various wavelength, and therefore are suitable for a detailed analysis of the opening angle and observer angle. I refer to all GRBs with at least 7 detections to be part of the *Golden Sample*. I consider a fit as good if the shape of the light curve is well reproduced. Keep in mind, that SCALEFIT fits in temporal and spectral space at the same time. For each fit that is not considered as good in the first run, I re-fit the data taking host extinction into account.

For GRB 050709A there are 2 X-ray detections at the same time, but they are one order of magnitude apart. Since X-ray flares have been frequent, while deep X-ray dips not, it seem likely that the data point with the lower flux is a corrupted measurement. However, the data point with the higher flux has a high residuum given the best fitting model. Omitting the data point with the higher flux does not change the result significantly, so I ignore that detection. GRB 080503A has a unrealistic best-fit p value, so I re-fit the multi-band light curve with a fixed p,

derived from the photon index Γ of the X-ray spectrum[2]. The late optical data of GRB 061006A is diluted by the host, and I omit the host detections. GRB 130603B shows a multi-modal behaviour for θ_0. I additionally sample both modes separately.

In 14 cases I can constrain $\theta_{\mathrm{obs}}/\theta_0$. In 12 cases I can constrain θ_0, and in 2 cases the PDF hits the limits of the prior for θ_0 which I interpret as lower limit of the opening angle.

For GRB 070707A there are exactly 7 detections, and GRB 061006A has just 6 detections after omitting the host. The DoF is DoF = (number of detections) - (degrees of freedom in the model) - 1 , and therefore results in a negative χ^2 for those two GRBs. According to Eq. 3.7 this corresponds in a high, but well defined log-likelihood. Although formally wrong in a statistical sense, it does not compromise the fitting process. All results for the Sample can be found in Tab. 4.5

For less than 7 detections it is not possible to put constraints on 7 fireball parameters. For all afterglows with less than 7 detections, I give the position of the Best Walker in Tab. A.1 for completeness. An example for a PDF where none of the parameters is constrained can be seen in Fig. 4.1.

4.5.1. The Influence of an Unknown Redshift

Not for all GRBs is a redshift measurement available. For the ones without a measurement, I assume a $z = 0.5$, similar to Fong et al. (2015).

The peak flux F_{peak} of the afterglow SED depends on z and $d_L(z)$ (Eq. 3.3). The characteristic frequencies ν_m and ν_c depend differently on the other fireball parameters Θ, but an unknown z would shift the frequencies in a similar fashion (Eq. 3.4 and Eq. 3.5). I check the influence of z on the best fitting fireball parameters Θ by using the afterglow of GRB 060313A, a well fitted afterglow without a redshift measurement. I perform 6 fits where I fix z (and therefore the luminosity distance $d_L(z)$) at a different value for each fit. A plot of the best fitting fireball parameters for each z can be seen in Fig. 4.2.

A different redshift z results in different best fitting parameters for E_{iso} and n_0. The fitting result of E_{iso} increases with a higher z, while the fitting result of n_0 decreases with higher z. This effect looks similar to the degeneracy $n_0 \propto E_{\mathrm{iso}}^{-5}$ from Sec. 3.4.2. However, the degeneracy occurs in a single set of best fitting parameters. What is seen in Fig. 4.2, are multiple sets of different best fitting parameters.

χ^2/DoF decreases with increasing redshift, until it converges at $\chi^2/\mathrm{DoF} \sim 1.6$ for $z > 0.5$. For fits with $z \lesssim 0.3$ the error in E_{iso}, n_0 and ϵ_B becomes large compared to the error of those quantities for $z \gtrsim 0.3$.

I find that ϵ_e, ϵ_B, p, θ_0 and θ_{obs} do not vary over z by an amount similar or

---

[2]Provided by the Swift/XRT online repository (Evans et al. 2009)
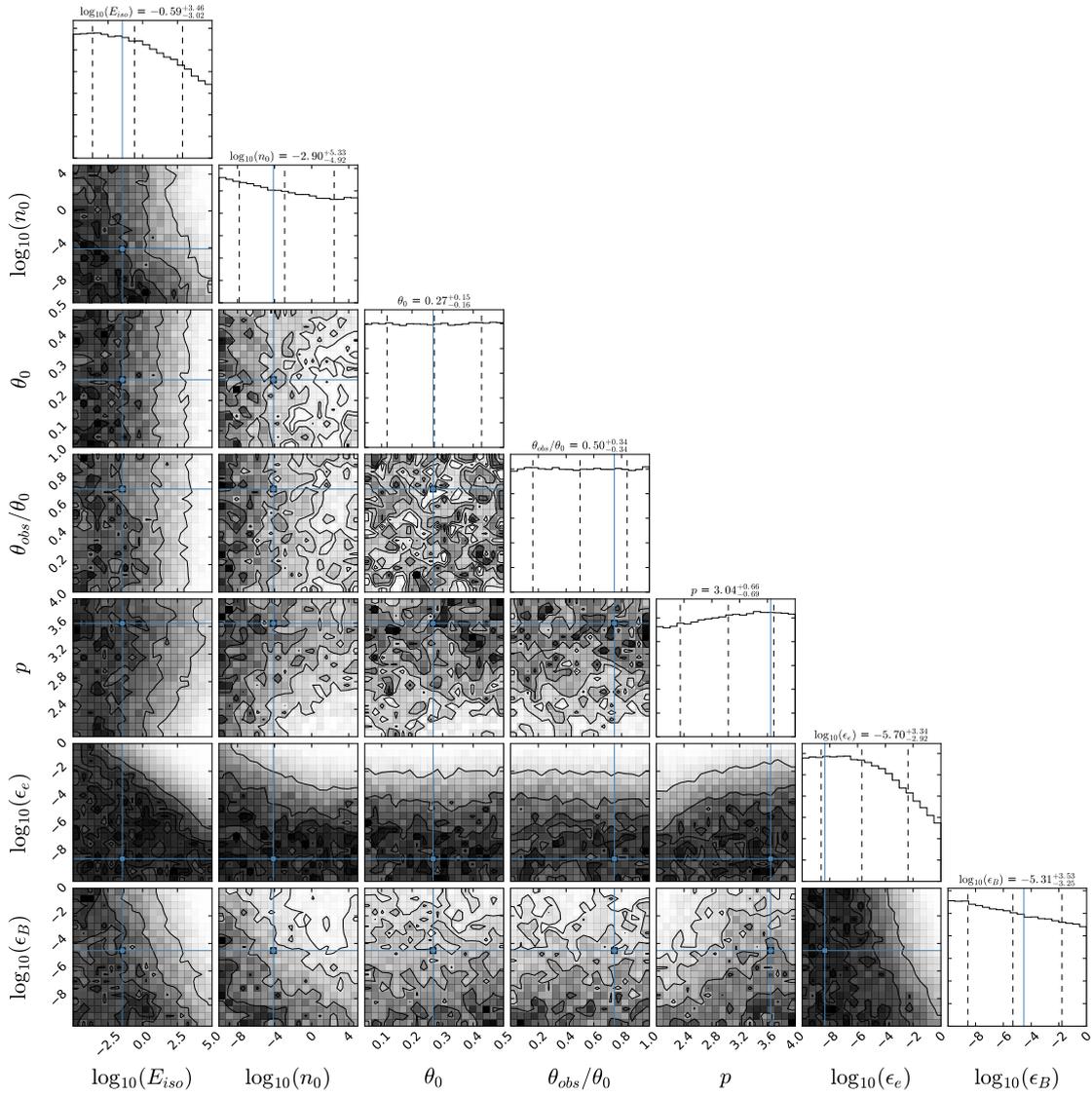
Figure 4.1.: PDF of GRB 081226B with 0 detections and 3 upper limits. None of the parameters is constrained. The blue dot corresponds to the Best Walker.
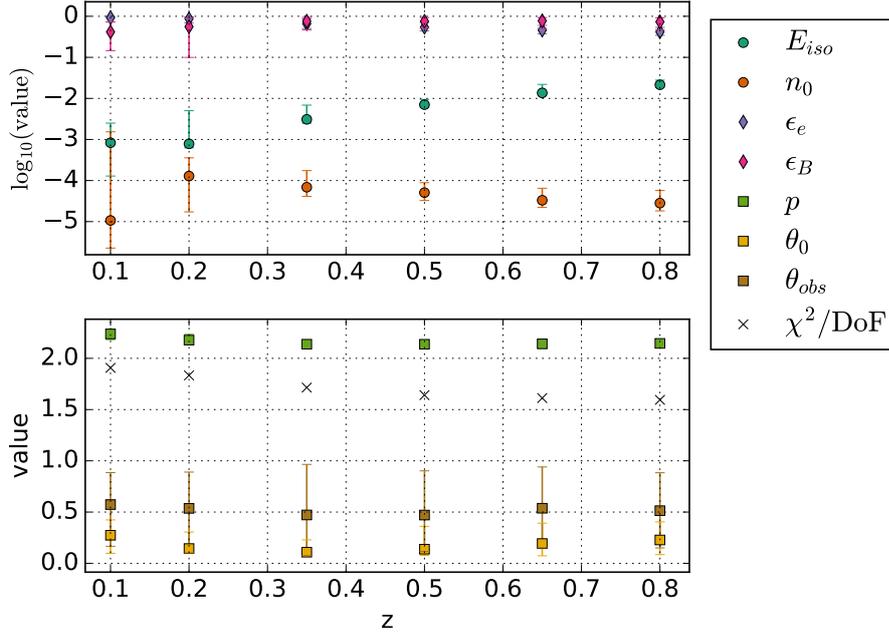
Figure 4.2.: Variation of the different quantities over the redshift z (and luminosity distance $d_L(z)$), for GRB 080503A. In the top plot the logarithmic quantities are shown, in the bottom plot, the linear quantities are shown. ϵ_e, ϵ_B, p, θ_0 and θ_{obs} do not vary over z. E_{iso} and n_0 are anti-correlated.

larger than their 1σ error. For the afterglows without a redshift measurement, my estimates of θ_0 and $\theta_{\mathrm{obs}}/\theta_0$ therefore are not corrupted by the (possibly wrong) assumption $z = 0.5$.

4.5.2. Opening and Observer Angles

The opening angles by Fong et al. (2015) in comparison to the angles of my method are given in Tab. 4.3. All jet opening and observer angles from my Golden Sample can be seen in Tab. 4.5.

The jet-opening angles $\theta_{0,\mathrm{Fong}}$ collected in Table 5 of Fong et al. (2015) are angles derived via the measurement of the jet break time (Eq. 4.3), and therefore under the assumption of an on-axis observer angle. I compare them with the angles derived with SCALEFIT in an *on-axis case* $\theta_{0,\mathrm{SF,OnAxis}}$, where I set the observer angle to the jet axis $\theta_{\mathrm{obs}}/\theta_{0,\mathrm{SF}} = 0$ Moreover, I list the opening angles $\theta_{0,\mathrm{SF}}$ for the *off-axis case*, where I also give the observer angle as a fraction of the opening angle $\theta_{\mathrm{obs}}/\theta_{0,SF}$.

Table 4.3.: Opening angles according to Fong et al. (2015) $\theta_{0,\text{Fong}}$, and according to my analysis for an on-axis case $\theta_{0,\text{SF,OnAxis}}$, and an off-axis case $\theta_{0,\text{SF}}$. $\theta_{\text{obs}}/\theta_0$ is the observer angle for the off-axis case. Good fits are tagged with a "g". Good fits with a constrained θ_0 are marked with a *, good fits with a constrained $\theta_{\text{obs}}/\theta_0$ are marked with a +. All angles are given in radians. The values with errors correspond to the median of the PDF of the parameter and its $\pm 68\%$ trusting levels. The values without errors are the Best Walker position, and come from data-sets with less than 7 detections.

GRB	$\theta_{0,\text{Fong}}$	$\theta_{0,\text{SF,OnAxis}}$	χ^2/DoF	$\theta_{0,\text{SF}}$	$\theta_{\text{obs}}/\theta_{0,\text{SF}}$	χ^2/DoF
050709A g +	$\gtrsim 0.262$	$> 0.39^{+0.07}_{-0.09}$	18.3	$> 0.40^{+0.07}_{-0.12}$	$0.3^{+0.2}_{-0.2}$	18.1
050724A g*+	$\gtrsim 0.436$	$0.192^{+0.005}_{-0.003}$	5.6	$0.193^{+0.021}_{-0.004}$	$0.02^{+0.03}_{-0.02}$	5.8
051221A g*+	$0.105 - 0.122$	$0.046^{+0.001}_{-0.001}$	3.3	$0.050^{+0.013}_{-0.004}$	$0.65^{+0.08}_{-0.09}$	3.0
090426A g*+	$0.087 - 0.122$	$0.10^{+0.01}_{-0.00}$	3.3	$0.11^{+0.03}_{-0.02}$	$0.92^{+0.03}_{-0.04}$	2.7
101219A	$\gtrsim 0.070$	-	na	0.05	0.95	na
111020A g	$0.052 - 0.140$	$0.3^{+0.2}_{-0.2}$	2.7	$0.28^{+0.15}_{-0.16}$	$0.5^{+0.3}_{-0.3}$	3.7
111117A	$\gtrsim 0.052 - 0.175$	-	na	0.10	0.70	na
120804A	$\gtrsim 0.227$	$0.07^{+0.33}_{-0.03}$	14.9	$0.11^{+0.31}_{-0.06}$	$0.3^{+0.5}_{-0.3}$	9.0
130603B g	$0.070 - 0.140$	$0.057^{+0.067}_{-0.001}$	4.3	$0.12^{+0.00}_{-0.06}$	$0.17^{+0.02}_{-0.04}$	4.3
130603B (I) g*+	$0.070 - 0.140$	-	-	$0.123^{+0.001}_{-0.001}$	$0.17^{+0.02}_{-0.03}$	4.3
130603B (II)g*+	$0.070 - 0.140$	-	-	$0.060^{+0.002}_{-0.002}$	$0.18^{+0.03}_{-0.05}$	4.3
140903A g*+	$\gtrsim 0.105$	$0.2^{+0.2}_{-0.1}$	3.6	$0.06^{+0.03}_{-0.01}$	$0.82^{+0.06}_{-0.04}$	3.3
140930B g*+	$\gtrsim 0.157$	$0.17^{+0.20}_{-0.04}$	4.7	$0.27^{+0.15}_{-0.12}$	$0.6^{+0.3}_{-0.5}$	5.1

4.6. Discussion

4.6.1. Details on the individual GRBs

For all angles where an opening angle estimate already exists in the literature (see Tab. 4.5.2; Tab. 5 in Fong et al. 2015) I check how the results from the classical method compare to the results from SCALEFIT with the observer angle to be fixed *on-axis*. Then I check if a free observer angle, an *off-axis* case, improves the fit.

050709A is in the Golden Sample and a good fit, but just a limit for the opening angle is derived. My on-axis case is consistent with Fong et al. (2015). Taking an off-axis observer angle into account does improve the fit.

050724A is in the Golden Sample, a good fit, and both angles are constrained. My on-axis case is inconsistent with the result from Fong et al. (2015). They give a lower limit for the jet opening angle under the assumption that the jet break does not occur before the last detection.

In my off-axis fit, I get the same opening angle θ_0 as in the on-axis case, and a very narrow observer angle. A free observer angle did not improve the fit. The model used by me interprets the achromatic steepening after the bump as jet break around $\sim 6 \times 10^4$s .

051221A is in the Golden Sample, a good fit, and both angles are constrained. My on-axis case is inconsistent with the result from Fong et al. (2015). They give a lower limit for the jet opening angle under the assumption that the jet break does not occur before the last detection.

Taking an off-axis observer angle into account does improve the fit. In my analysis the curvature of the light curve is interpreted as a smeared out jet break around $\sim 4 \times 10^5$s.

090426A is in the Golden Sample, a good fit, and both angles are constrained. My on-axis case is consistent with Fong et al. (2015).

In the off-axis case my result indicates that the jet is observed almost on-edge. The fit of the off-axis case has a significantly smaller χ^2, showing that in for GRB 090426A an on-axis observation would be a crude approximation.

101219A is not in my Golden Sample. For completeness I give the value of the Best Walker. With just 2 detections my method is not able to constrain any of the fireball parameters.

111020A is in the Golden Sample and a good fit, but the angles are not constrained. The on-axis case of my method has a lower χ^2/DoF since I use one model parameter less than in the off-axis case. The total χ^2 of the fit stays the same. Fong et al. (2015) (citing Fong et al. (2012)) interpret a break in the Swift/XRT light curve $\sim 1.7 \times 10^5$s as jet break.

111117A is not in my Golden Sample. For completeness I give the value of the

Best Walker. With just 5 detections my method is not able to constrain any of the fireball parameters. Fong et al. (2015) give a lower limit for the jet opening angle under the assumption that the jet break does not occur before the last detection.

120804A is in the Golden Sample, but not a good fit. The model failed to reproduce the slope of the light curve, and therefore I do not consider my estimates for the angles as trustworthy. Fong et al. (2015) give a limit for the jet opening angle under the assumption that the jet break does not occur before the last detection.

130603B is in the Golden Sample and a good fit. My on-axis case is consistent with Fong et al. (2015). The off-axis case shows a multi-modal behavior for θ_0 in its PDF. Therefore I sample each mode separately: Mode (I) at $\theta_{0,SF} = 0.12^{+0.00}_{-0.00}$ Mode (II) at $\theta_{0,SF} = 0.06^{+0.00}_{-0.00}$, In both modes the angles are constrained. Involving an off-axis observer angle does not improve the fit.

140903A is in the Golden Sample, a good fit, and both angles are constrained. My on-axis fit is consistent with the limit for the opening angle derived by Fong et al. (2015).

In the off-axis case my result indicates that the jet is observed almost on-edge. The fit of the off-axis case has a smaller χ^2, showing that in for GRB 140903A an on-axis observation would be a crude approximation.

This GRB was also discussed by Zhang et al. (2017). They use energy injection to explain the light curve in the time interval 10^3 s to 7×10^3 s as a plateau, and find a $\theta_0 = 0.05$ rad using an on-axis model with energy injection. I find that the data during this time interval does not diverge more than 3σ from my model, which does not involve energy injection. Their values are neither consistent with my on-axis estimate, nor with the on-axis estimate from Fong et al. (2015).

Another analysis was done by Troja et al. (2016), where they found $\theta_0 = 0.09 \pm 0.01$ rad and $\theta_{\rm obs}/\theta_0 \sim 0.611$. Their opening angle is consistent with my result for the opening angle, however their observer angle is smaller.

140930B is in the Golden sample and a good fit, but the angles are not constrained. The trusting interval of my PDF is consistent with the lower limit for the jet opening angle derived by Fong et al. (2015), in the on-axis and the off-axis case. The on-axis case of my method has a lower χ^2/DoF since I use one model parameter less than in the off-axis case, while the total χ^2 of the fit stays the same.

Additionally to the afterglows above, I find 6 GRBs that are well fitted and have constraints on the angles:

060313A is in the Golden Sample, a good fit, and both angles are constrained. This afterglow I also use to check the influence of the redshift on the fit.

061201A is in the Golden Sample, a good fit, and both angles are reasonably constrained.

080503A is in the Golden Sample, a good fit, and both angles are constrained.
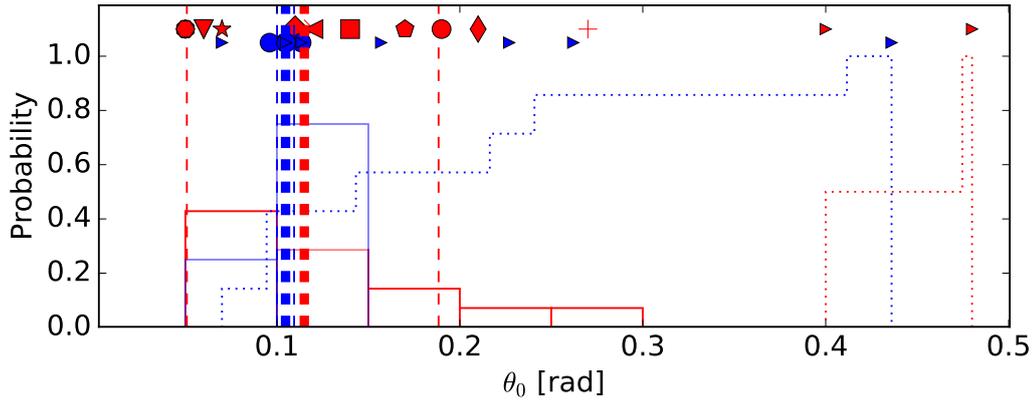
Figure 4.3.: Distribution of short GRB jet-opening angles of my analysis (red histogram, off-axis case, median: $\tilde{\theta}_{0,\text{short}} = 0.12^{+0.07}_{-0.06}$ rad), and lower limits (red cumulative histogram). Also shown are measurements by Fong et al. (2015) (blue histogram, $\tilde{\theta}_{0,\text{Fong}} = 0.104$ rad) and lower limits (blue cumulative histogram). The red and blue markers indicate the opening angles of the individual GRBs. A small triangle pointing to the right indicates a lower limit. In most cases Fong et al. (2015) did not give values with uncertainties for their estimates, but ranges for measurements or limits. I plot the mean of their intervals. The thick vertical lines indicate the median of the histograms, the thin vertical lines indicate the 68% range.

To receive a good fit, I fixed $p = 3.8$ as the XRT spectrum (Evans et al. 2009) implied, when $\nu_c > \nu_{X-ray}$. The assumption $\nu_c < \nu_{X-\text{ray}}$ implying a $p = 2.8$ leads to a worse fit. According to my model this afterglow is observed nearly edge on.

090305A is in the Golden Sample and a good fit, however θ_0 hits the edge of the prior. I interpret this as lower limit $\theta_0 > 0.5$. The observer angle is on-axis. The best fitting model finds a rather late ν_m crossing $\sim t_{\text{cross}} \sim 7000$ s in the optical. Before that time the light curve shows a phase with a shallow decay, which also maybe explained by energy injection. More details in Fig. A.20

090510A is in the Golden Sample, a good fit, and both angles are constrained. The best fitting model implies an observer angle which is almost at the edge of the jet.

140129B is in the Golden Sample, a good fit, and both angles are constrained. The jet is rather narrow, and the observer angle is close to the edge of the jet.

All results are listed in Tab. 4.5. The cumulative distributions can be seen in Fig. 4.4.

On the Distribution of Short GRB Jet Opening Angles

In Fig. 4.4 the distributions of all derived opening and observer angles are shown. In my analysis the median with the 68% quantiles of the opening angle is $\tilde{\theta}_{0,short} = 0.12^{+0.07}_{-0.06}$ rad, and the median of the observer angle as fraction of the opening angle
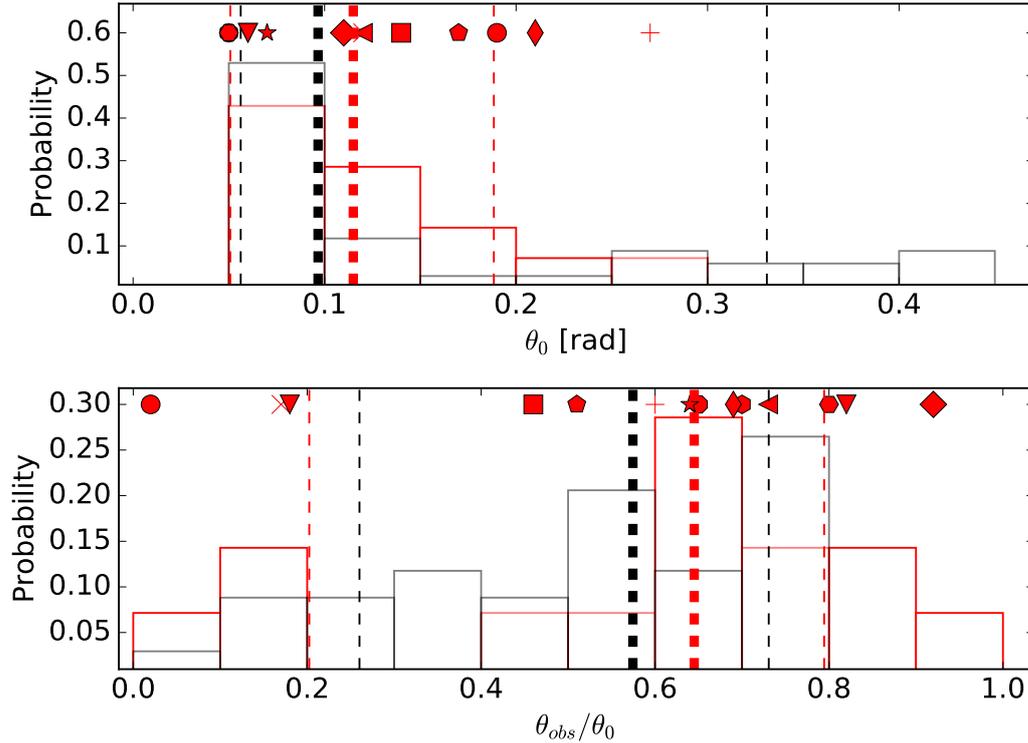
Figure 4.4.:
Top: Distribution of short GRB jet-opening angles of my analysis (red histogram, off-axis case, median: $\tilde{\theta}_{0,\text{short}} = 0.12^{+0.07}_{-0.06}$ rad), and long GRB opening angle measurements of Ryan et al. (2015) (black histogram, $\tilde{\theta}_{0,\text{long}} = 0.10^{+0.23}_{-0.04}$ rad).
Bottom: Distribution of the observer angle as fraction of the opening angle from my analysis of short GRBs (red, $\tilde{\theta}_{\text{obs,short}}/\theta_0 = 0.65^{+0.15}_{-0.44}$) and for long GRBs (Ryan et al. 2015) (black, $\tilde{\theta}_{\text{obs,long}}/\theta_0 = 0.57^{+0.16}_{-0.31}$).
Both: The red markers from the top plot are found in the bottom plot. Same markers correspond to the same GRB. The thick vertical lines indicate the median of the histograms, the thin vertical lines indicate the 68% range.

is $\tilde{\theta}_{\text{obs,short}}/\theta_{0,short} = 0.6^{+0.1}_{-0.4}$.

According to my analysis 3 GRBs have a remarkably small opening angle $\theta_0 < 0.1$ rad compared to the classically derived opening angles

- 051221A: $\theta_{0,SF} = 0.050^{+0.013}_{-0.004}$ rad, $\theta_{\text{obs}}/\theta_{0,SF} = 0.65^{+0.08}_{-0.09}$
  The fitted light curve has a curvature that is interpreted as an early smeared out jet break. This afterglow was observed off-axis. Ryan et al. (2015) also fitted this GRB with SCALEFIT ($\theta_0 = 0.45^{+0.03}_{-0.04}$ rad, $\theta_{\text{obs}}/\theta_0 = 0.45^{+0.05}_{-0.06}$) only using XRT data. Zhang et al. (2015a) estimated a $\theta_0 = 0.09^{+0.16}_{-0.04}$ rad, $\theta_{\text{obs}}/\theta_0 = 0.02^{+0.3}_{-0.02}$ using *Swift/XRT* and late time *Chandra* data, and a nested sampling approach. My opening angle is consistent with the opening angle from Zhang et al. (2015a), but not with Ryan et al. (2015) who are missing the Chandra data. GRB 051221A is an example how sensitive the derived values depend

on the data, the model and the used fitting method.

- 080503A: $\theta_{0,SF} = 0.050^{+0.009}_{-0.004}$ rad, $\theta_{\mathrm{obs}}/\theta_{0,SF} = 0.80^{+0.09}_{-0.12}$
  This afterglow was observed off-axis. The fitted light curve shows a late ν_m crossing. Due to a multi-modality in PDF of the first fit, I had to fix p to get a good fit. The high value for p (derived from the XRT spectrum) indicates that this afterglow may not be explained by the standard model.

- 130603B (Mode II): $\theta_{0,SF} = 0.060^{+0.002}_{-0.002}$ rad, $\theta_{\mathrm{obs}}/\theta_{0,SF} = 0.18^{+0.03}_{-0.05}$
  From the 3 GRBs with a small opening angle, this is the one with the smallest observer angle, which basically rules out an off-axis effect. The best fitting model shows a break around $\sim 10^5$s. The initial fit of GRB 130603B showed a multi-modality. The data also allows for an opening angle $\theta_0 = 0.123^{+0.001}_{-0.001}$ (Mode I)

I find 2 lower limits for jet opening angles:

- GRB 050709A with $\theta_0 > 0.4$ rad: The light curve of this afterglow follows a single power law, and there is no apparent curvature. A wide jet in which the curvature effect of a smeared out jet break occurs as late as possible, is the favoured for SCALEFIT.

- GRB 090305 with $\theta_0 > 0.48$ rad: The fit is driven by a "plateau like phase" in the light curve. A somewhat exotic combination of two effects is favoured by SCALEFIT: A late ν_m crossing and a transition from fast to slow cooling. In this best fitting model, the jet opening angle happens to be very wide.

Jet breaks have been discussed by e.g. Zhang & MacFadyen (2009) and Wygoda et al. (2011) in the context of numerical simulations. They argue that for larger opening angles $\theta_0 > 0.2$ rad there is no exponential sideways expansion of the jet, and therefore no sharp jet break. Granot & Piran (2012) even claim that sideways spreading is largely eliminated for $\theta_0 \gtrsim 0.05$ rad. As a consequence, the classical method would not be able to measure opening angles $\theta_0 > 0.2$, respectively $\theta_0 > 0.05$. The 4 estimates of short GRB opening angle of Fong et al. (2015) are narrowly distributed $\tilde{\theta}_{0,\mathrm{Fong}} = 0.104^{+0.005}_{-0.005}$ rad. The limits up to $\theta_0 > 0.44$ rad are derived under the assumption that the jet break occurs after the last detection of the afterglow.

In Tab. 4.4 I compare the jet opening and observer angles of short GRBs, derived in this work, and the jet opening and observer angles of long GRBs from Ryan et al. (2015). I find that the median of the distribution of the angles of short GRBs does not differ significantly from the median of the distribution of long GRBs.

Table 4.4.: Summary of the jet median opening and observer angles. The errors are the 0.84 quantiles of the distribution, corresponding to the 68% confidence intervals.

	θ_0 [rad]	$\theta_{\mathrm{obs}}/\theta_0$	Reference
short GRBs	0.104	on-axis assumption	Fong et al. (2015)
short GRBs	$0.12^{+0.07}_{-0.06}$	$0.6^{+0.1}_{-0.4}$	this work
long GRBs	$0.10^{+0.23}_{-0.04}$	$0.6^{+0.2}_{-0.3}$	Ryan et al. (2015)

4.7. Conclusion

4.7.1. Comparison of the Methods

Out of the 11 afterglows with existing jet opening angle estimates my method failed to describe 3: While Fong et al. (2015) estimated limits for GRB 101219A and GRB 111117A, there is not enough data to use my method. For GRB 120804A SCALEFIT is not able to fit the temporal and spectral slope satisfactory at the same time. The main difference between both methods is that in the classical method Eq. 4.3 is applied to a single band, instead I applied SCALEFIT to the whole multiband set. I explain the discrepancy between the two methods by the fact that the classical method is "too simple to fail". Even in the case of no apparent jet break a limit can be derived, and just data from a single band is taken into account. The hydro-simulations, however, assume the specific scenario of a jet in the deceleration phase in an ISM. If those assumptions are not fulfilled, the model is not capable of reproducing the temporal and spectral behaviour of the afterglow. I can not say if limits for GRB 101219A and GRB 111117A of by Fong et al. (2015) are trustworthy, since I can not make any statement about whether their model assumptions are correct or incorrect for that specific afterglow. However, SCALEFIT fails to fit the afterglow of GRB 120804A, which indicates that it is not a standard afterglow in an ISM. Fong et al. (2015) gives a limit anyway because their method ignores a part of the data. Therefore the limit for the opening angle of GRB 120804A I claim to be wrong.

First I compared on-axis fits to off-axis fits. In 5 cases of my analysis an off-axis observation does not improve the fit (050709A, 050724A, 111020A, 130603B, 140930B), where 3 of them are consistent with the classically derived on-axis angles (050709A, 130603B, 140930B), and 2 are not (050724A, 111020A). In 4 cases of my analysis the fit improved, by taking an off-axis observation angle into account (050709A, 051221A, 090426A, 140903A), where 1 is inconsistent (051221A) with the classically derive on-axis angles, and 2 are consistent (090426A, 140903A).

Then I applied SCALEFIT to afterglows that do not have an opening angle estimate

so far, and have a minimum of 7 detections. I derived the opening and observer angle of 5 additional afterglows (060313A, 061201A, 080503A, 090510A, 140129B), and limits in the opening angle of 1 afterglows (090305A) (see Tab. 4.5).

Summarizing, in 5 cases my method gave constraints on the angles, where the classical method did not. In 3 cases my method gave no constraints on the angles, where the classical method did: Two times, because the data coverage was not sufficient enough for my method; One time, because my method was not able to reproduce the temporal and spectral behaviour, while the classical method just ignores the spectral information in the data, therefore gives a not trustworthy result.

SCALEFIT models the whole SED evolution of an afterglow, which makes it possible to use data from all points in time and spectral space without any intra- or extrapolations. Especially for the sparse data sets of short GRB afterglow this feature proves to be very useful. Unlike in the classical method I do not rely on a single well sampled light curve, and I am not forced to ignore all spectral information.

4.7.2. On the Jet Opening Angles

SCALEFIT includes a model based on 2D hydro-dynamical numerical simulations that treat the dynamics of the jet in high detail, and is paired with a radiative transfer code. Compared to analytical models the detailed physics adds another level of complexity to the light curve shape: A smooth curvature due to continuous sidewards spreading and decreasing beaming of the emission. Most analytical models assume a runaway behaviour or a sudden visibility of the jet edges, and therefore a discrete jet break. If the curvature of the measured light curve is constraining enough it is possible to derive the jet opening angle θ_0 without a clear jet break, and independently from the knowledge of other fireball parameters. Additionally the model is capable of deriving the observer angle $\theta_{\rm obs}$.

I found that short GRBs have a median opening angle $\tilde{\theta}_0 = 0.12^{+0.07}_{-0.06}$, and a median observer angle $\tilde{\theta}_{\rm obs,short}/\theta_0 = 0.6^{+0.1}_{-0.4}$. My median opening angle is consistent with the median opening angle derived by Fong et al. (2015).

The distribution of the opening angles does not differ significantly from the distribution of the jet opening of long GRBs. Due to the cosmological principle, the observer angle is expected to be distributed isotropically. The systematic derivation from an isotropic distribution is the same for my short GRB estimates and the long GRB estimates by Ryan et al. (2015) (both using SCALEFIT).

Table 4.5.: Fitting Results for more than 6 detections. The values correspond to the marginalized median of the PDF, and its 68% trusting interval. Good fits are tagged with a "g". Good fits with a constrained θ_0 are marked with a *, good fits with a constrained $\theta_{\mathrm{obs}}/\theta_0$ are marked with a +. In two cases the PDF of θ_0 has a maximum at the edge of the prior. I interpret this as lower limit, since the prior in the direction of $\theta_0 = 0.5$ is not a physical restriction, but the maximal opening angle used in the simulations. The cases where $\theta_{\mathrm{obs}}/\theta_0 = 1$ hits the prior are in fact physical and correspond to an observer angle on the edge of the jet $\theta_{obs} = \theta_0$. GRBs that show up in Tab. 4.3 are tagged with an o.

GRB	r	o	x	n	χ^2/DoF	θ_0	$\theta_{\mathrm{obs}}/\theta_0$	p
050709A og +	y	y	y	10	18.1	$> 0.40^{+0.07}_{-0.12}$	$0.29^{+0.24}_{-0.20}$	$3.13^{+0.01}_{-0.01}$ [3]
050724A og*+	y	y	y	39	5.8	$0.193^{+0.021}_{-0.004}$	$0.02^{+0.03}_{-0.02}$	$2.37^{+0.02}_{-0.02}$
051221A og*+	y	y	y	46	3.0	$0.050^{+0.013}_{-0.004}$	$0.65^{+0.08}_{-0.09}$	$2.41^{+0.02}_{-0.02}$
060121A	n	y	y	54	10.5	$0.42^{+0.05}_{-0.07}$	$0.34^{+0.15}_{-0.18}$	$2.004^{+0.005}_{-0.002}$
060313A g*+	y	y	y	60	1.6	$0.14^{+0.21}_{-0.06}$	$0.46^{+0.45}_{-0.35}$	$2.14^{+0.04}_{-0.04}$
061006A g	n	y	y	9	"-0.2"	$0.28^{+0.15}_{-0.15}$	$0.50^{+0.33}_{-0.33}$	$2.90^{+0.24}_{-0.80}$ [4]
061201A g*+	n	y	y	9	2.2	$0.17^{+0.20}_{-0.10}$	$0.51^{+0.34}_{-0.31}$	$2.51^{+0.22}_{-0.18}$
070707A g	n	y	y	7	"-25.2"	$0.24^{+0.03}_{-0.03}$	$0.03^{+0.04}_{-0.02}$	$2.06^{+0.08}_{-0.03}$
070714B	y	y	y	14	0.8	$0.28^{+0.15}_{-0.16}$	$0.49^{+0.38}_{-0.34}$	$3.39^{+0.23}_{-0.39}$ [5]
070724A	y	y	y	11	37.9	$0.32^{+0.12}_{-0.14}$	$0.44^{+0.32}_{-0.30}$	$3.96^{+0.03}_{-0.07}$
070809A g	n	y	y	15	2.9	$0.29^{+0.14}_{-0.16}$	$0.49^{+0.35}_{-0.33}$	$2.04^{+0.06}_{-0.03}$
080426A g	n	y	y	14	2.1	$0.26^{+0.16}_{-0.16}$	$0.53^{+0.32}_{-0.35}$	$2.64^{+0.52}_{-0.33}$
080503A g*+	y	y	y	9	17.6	$0.050^{+0.009}_{-0.004}$	$0.80^{+0.09}_{-0.12}$	3.8 (fixed)
090305A g +	n	y	y	34	8.9	$> 0.48^{+0.01}_{-0.05}$	$0.14^{+0.31}_{-0.11}$	$2.012^{+0.014}_{-0.005}$
090426A og*+	n	y	y	51	2.7	$0.11^{+0.03}_{-0.02}$	$0.92^{+0.03}_{-0.04}$	$2.10^{+0.01}_{-0.01}$
090510A g*+	y	y	y	42	0.5	$0.21^{+0.18}_{-0.11}$	$0.69^{+0.22}_{-0.40}$	$2.90^{+0.13}_{-0.13}$
110112A g	y	y	y	9	5.3	$0.28^{+0.15}_{-0.15}$	$0.51^{+0.34}_{-0.33}$	$2.80^{+0.16}_{-0.60}$
111020A og	y	y	y	11	3.7	$0.28^{+0.15}_{-0.16}$	$0.50^{+0.33}_{-0.34}$	$2.28^{+0.15}_{-0.21}$
111121A g	y	n	y	27	1.6	$0.26^{+0.16}_{-0.15}$	$0.52^{+0.32}_{-0.31}$	$2.80^{+0.61}_{-0.40}$
120804A o	y	y	y	22	9.0	$0.11^{+0.31}_{-0.06}$	$0.31^{+0.52}_{-0.26}$	$2.01^{+0.02}_{-0.01}$
130603B o g	y	y	y	78	4.3	$0.121^{+0.002}_{-0.062}$	$0.17^{+0.02}_{-0.04}$	$2.56^{+0.03}_{-0.09}$
130603B o(I) g *+	y	y	y	78	4.3	$0.123^{+0.001}_{-0.001}$	$0.17^{+0.02}_{-0.03}$	$2.59^{+0.02}_{-0.02}$
130603B o(II)g *+	y	y	y	78	4.3	$0.060^{+0.003}_{-0.002}$	$0.18^{+0.03}_{-0.05}$	$2.48^{+0.02}_{-0.02}$
130912A g	y	y	y	14	2.4	$0.28^{+0.15}_{-0.15}$	$0.49^{+0.35}_{-0.34}$	$3.24^{+0.28}_{-0.62}$
131004A	y	y	y	18	13.7	$0.32^{+0.12}_{-0.14}$	$0.62^{+0.27}_{-0.42}$	$2.28^{+0.07}_{-0.06}$
140129B g*+	n	y	y	14	6.0	$0.12^{+0.15}_{-0.04}$	$0.73^{+0.15}_{-0.19}$	$2.27^{+0.21}_{-0.13}$
140903A og*+	y	y	y	41	3.3	$0.06^{+0.03}_{-0.01}$	$0.82^{+0.06}_{-0.04}$	$2.02^{+0.01}_{-0.01}$
140930B og*+	y	y	y	22	5.1	$0.27^{+0.15}_{-0.12}$	$0.60^{+0.26}_{-0.47}$	$2.20^{+0.11}_{-0.10}$

CHAPTER 5

THE PARTICULARLY INTERESTING GRB 150424A

This chapter is a wrap up of a paper I submitted to Astronomy & Astrophysics on 8th February 2017. I perform an afterglow analysis of the EE short GRB GRB 150424A. GRB 150424A is particularly interesting, since just $\sim 10\%$ of all GRBs are short GRBs, and just $\sim 15\%$ of those short GRBs show EE. What makes this burst very valuable is that there are early optical detections which revealed a plateau phase in the optical afterglow.

Examples for short GRBs with plateaus are GRB 060313A (Roming et al. 2006); GRB 061201A (Stratta et al. 2007); GRB 130603B (Fan et al. 2013; de Ugarte Postigo et al. 2014); see also Kann et al. (2011) for 060313A, 061201A, 090510A. To my knowledge just GRB 060313A (Roming et al. 2006) has a temporal data coverage comparable to GRB 150424A, but is not covered in as many bands. There so far is no data-set for other short GRBs with a plateau phase, that can compete with the temporal and spectral coverage of the data I present.

I show that energy injection can explain the plateau phase of the afterglow of GRB 150424A, and that the energy injection is consistent with what is expected from a magnetar central engine.

5.1. GRB Details

In this work I analyse afterglow data of GRB150424A: An EE short GRB with early multi-band coverage. I use data from the Gamma-ray Optical Near-infrared Detector (GROND) (Greiner et al. 2008), the Keck/LRIS instrument[1], the Swift/Ultraviolet and Optical Telescope (UVOT) (Roming et al. 2005), the Swift/X-Ray Telescope

---

[1]Provided by D.A. Perley and M.J. McConnell

(XRT) (Burrows et al. 2005), the Hubble Space Telescope (HST)[2] and additional data from the literature. This high quality data-set of an optical plateau phase in EE short GRB afterglows is unique in temporal and spectral coverage.

In Sec. 5.2 I present the data I use. In Sec. 5.3 I perform a phenomenological analysis and present its physical implications. In Sec. 5.4 I discuss the results and its implications for the physical nature of the GRB, followed by my conclusions in Sec. 5.5.

5.2. Data

On 24th April 2015 the *Swift* Burst Alert Telescope (BAT) detected the short GRB 150424A with a single peak of 0.5s duration, and a fading X-ray counterpart was instantly detected by the *Swift*/XRT (Beardmore et al. 2015). A non fading optical counterpart was found immediately (Marshall & Beardmore 2015) with the *Swift*/UVOT (Roming et al. 2005). In a refined analysis weak extended emission for ~ 100s was found (Barthelmy et al. 2015) and resulted in a $T_{90} = 91 \pm 22$s.

The UVOT observations cover the time from $82\,\text{s} - 1.4 \times 10^6\,\text{s}$ after the burst. UVOT photometry was carried out [3]. on pipeline processed sky images downloaded from the *Swift* data center [4] following the standard UVOT procedure (Poole et al. 2008). Source photometric measurements were extracted from the UVOT early-time event data and later imaging data files using the tool UVOTMAGHIST (v1.1) with a circular source extraction region of 5" radius for the first 16ks of data, after which a 3.5" source region radius was used to maximize the signal-to-noise. In order to remain compatible with the effective area calibrations, which are based on 5" aperture photometry, an aperture correction was applied on the photometry that was extracted using the smaller source aperture. I consider a signal-to-noise ratio of $\sigma > 3$ as detection.

1.6 hrs after the burst Perley & McConnell (2015) reported a *g*- and *R*- band detection of the afterglow with the Low Resolution Imaging Spectrometer (LRIS). GROND was able to follow up (Kann et al. 2015) 15 hrs after the burst and observed strong fading at this point. All in all, GROND observations covered 8 epochs with detections in the first 3 epochs. I performed aperture photometry on the LRIS and GROND data, using a IRAF/PyRAF (Tody 1993) based pipeline (Yoldaş et al. 2008; Krühler et al. 2008), and calibrated the data against secondary field stars.

---

[2]Based on observations made with the NASA/ESA Hubble Space Telescope, obtained from the Data Archive at the Space Telescope Science Institute, which is operated by the Association of Universities for Research in Astronomy, Inc., under NASA contract NAS 5-26555. These observations are associated with program # 13830 Pi'ed by N. Tanvir.

[3]The reduced UVOT data was provided by Patricia Shady, who acknowledges support through the Sofja Kovalevskaja Award from the Alexander von Humboldt Foundation of Germany.

[4]www.swift.ac.uk/swift_portal

The GRB afterglow is north east of an elliptical galaxy with a spectroscopic redshift $z = 0.3$ (Castro-Tirado et al. 2015) (see finding chart in Fig. 5.1), but there are Hubble Space Telescope (HST) detections (Tanvir et al. 2015) of an extended source right at the position of the afterglow which is more likely the host galaxy.

Fong (2015) report a VLA 9.8 GHz detection 18 hrs after the trigger, and Kaplan et al. (2015) report early MWA upper limits in the MHz regime.
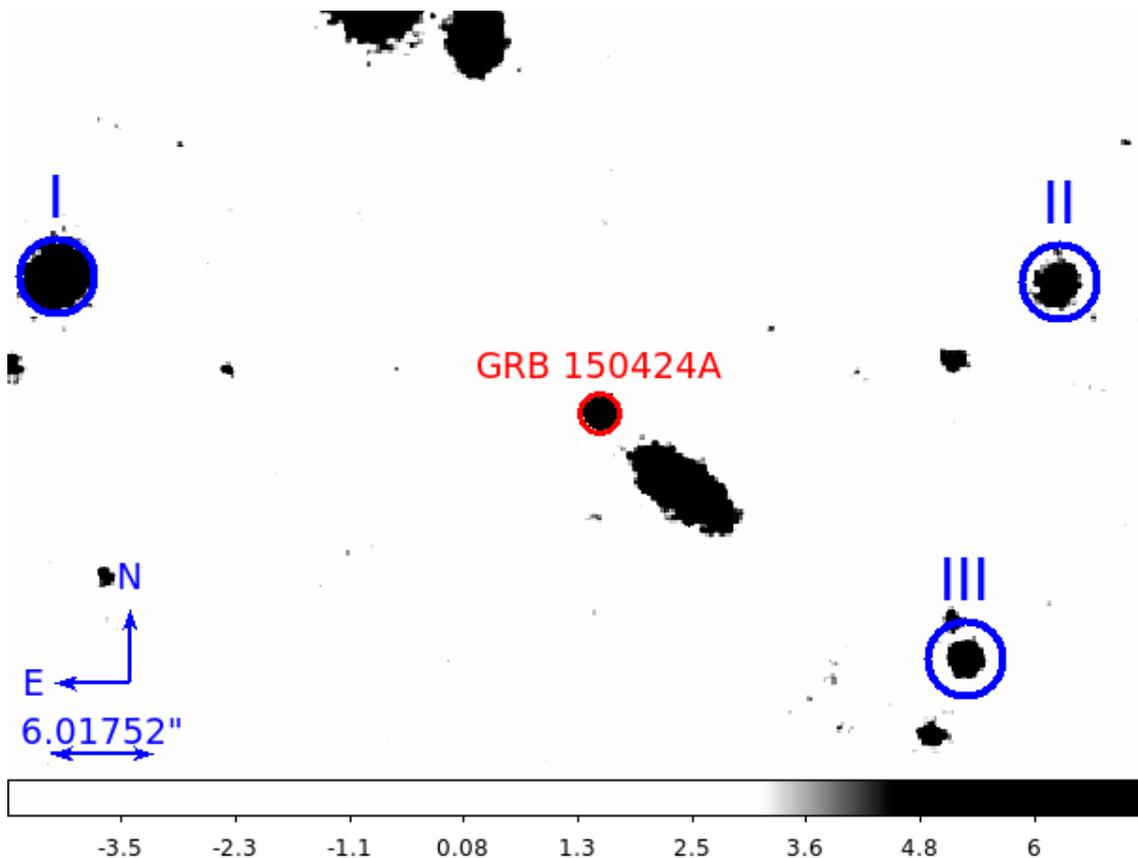
Figure 5.1.: GROND finding chart of GRB 150424A (GROND r band). There is a galaxy south west of the afterglow, but late time HST observations find a weak expanded source at the position of the afterglow which is believed to be the host.

5.3. Analysis

5.3.1. Phenomenology

A GRB afterglow can be described by the empirical flux description (Eq. 2.33)

$$F_\nu(t) \propto t^{-\alpha}\nu^{-\beta}$$

with time t and observed frequency ν. The temporal slope α and the spectral slope β depend on the observed spectral regime and can change over time (Mészáros &

Rees 1997a; Granot & Sari 2002).

The optical light curve of GRB 150424A (see Fig. 5.2) consists of two segments, a plateau and a decay phase. Both phases are covered by the UVOT observations. The GROND observations cover the decay phase and constrain its temporal slope. I fit all optical bands with more than one detections with one smoothly broken power law per band. They all share their temporal slopes α and break time $t_{\text{break,opt}}$.

The X-ray light curve shows a steep decay until around 10^3 s, followed by a shallow decay phase, steepening again after $\sim 5 \times 10^5$ s. The steep decay phase is most likely due to the tail of prompt emission, so I ignore the X-ray data before 10^3 s, since a standard fireball afterglow model is not applicable. The rest of the X-ray light curve I fit with a smoothly broken power law.

To determine the spectral slopes β, I perform a joined broad-band fit of optical and X-ray data using XSPEC (Arnaud 1996). The fireball model assumes synchrotron as the underlying emission mechanism, therefore the spectral slopes just depend on the electron energy distribution. The model uses a power law like electron energy distribution with slope p. Assuming a constant p, the spectral slopes do not change. The light curve fit supports the assumption, since thanks to the multi-band capabilities of GROND a chromatic break would be clearly seen in the residuals around the optical break time.

I choose 4 time slices over which I integrate the XRT spectral counts (indicated with the grey bars in Fig. 5.2). Then I re-bin each spectrum, where I have to find an optimum between counts per spectral bin and number of spectral bins. For SED2 and SED3 I re-normalize the total flux of the spectrum to the flux of the XRT light curve at the point in time of the optical data. For SED0 and SED1 I do not expect the total flux to be significantly different from the flux at the point in time of the optical data. Afterwards I add a systematic error of 10 %, accounting for the flux calibration relative to the optical data.

First, I correct the optical/NIR and UV data for galactic extinction $E(B - V) = 0.051 \pm 0.002$ (Schlafly & Finkbeiner 2011), then I use a model consisting of a (broken) power law, and involve galactic absorption $N_H = 0.602 \times 10^{21} \text{cm}^{-2}$ (Kalberla et al. 2005), and host extinction and absorption. I fit the 4 SEDs simultaneously, while each single SED has an individual break frequency and normalization. I find the spectral slopes before and after the temporal break to be consistent, so for the final fit I link them for all 4 SEDs. I also use the constraint $\beta_{\text{optical}} - \beta_{\text{X-ray}} = 0.5$ for a synchrotron SED in the slow cooling case with the cooling frequency ν_c between optical and X-ray. Not setting this constraint leads to a degeneracy between the spectral slopes and the break frequency. The resulting optical slope also is consistent with the fast cooling case where $\beta_{\text{opt}} = 0.5$

The SED fits including the data and the unfolded model (just the power law,
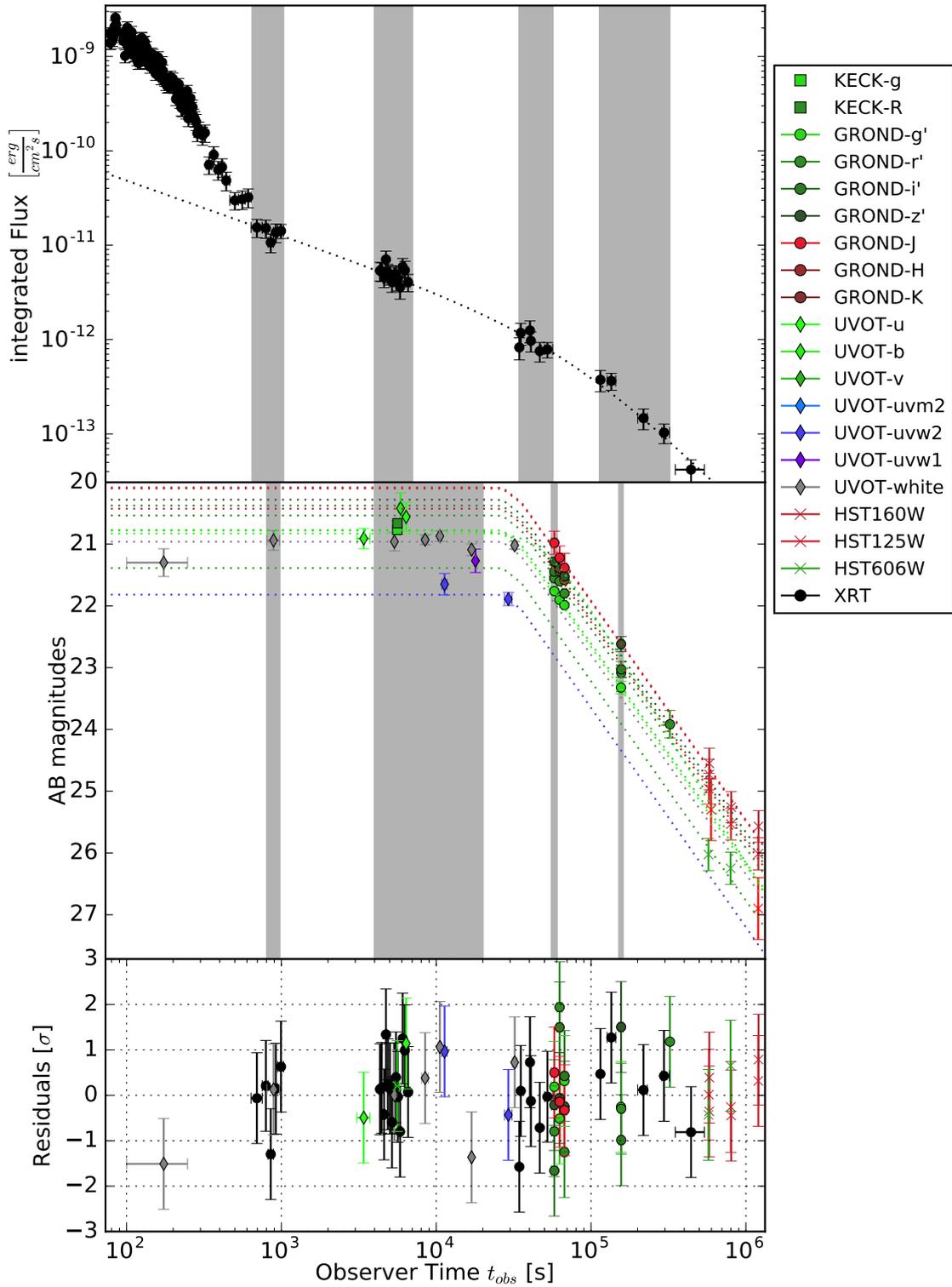
Figure 5.2.: XRT and GROND light curves of GRB 150424A. The shaded areas correspond to the time slices of the snap shot analysis. The dotted lines are the best fitting smoothly broken power laws. The X-ray light curve fit has a reduced $\chi^2 = 0.57$, the optical light curve fit has a reduced $\chi^2 = 1.04$. I fit all bands with more than one detections: g', r', i', z', J, white, u, uvw2, HST160W, HST125W and HST606W. All detections and upper limits (not shown in light curve) are given in Tab. B.3. The temporal slopes α are given in Tab. 5.2.
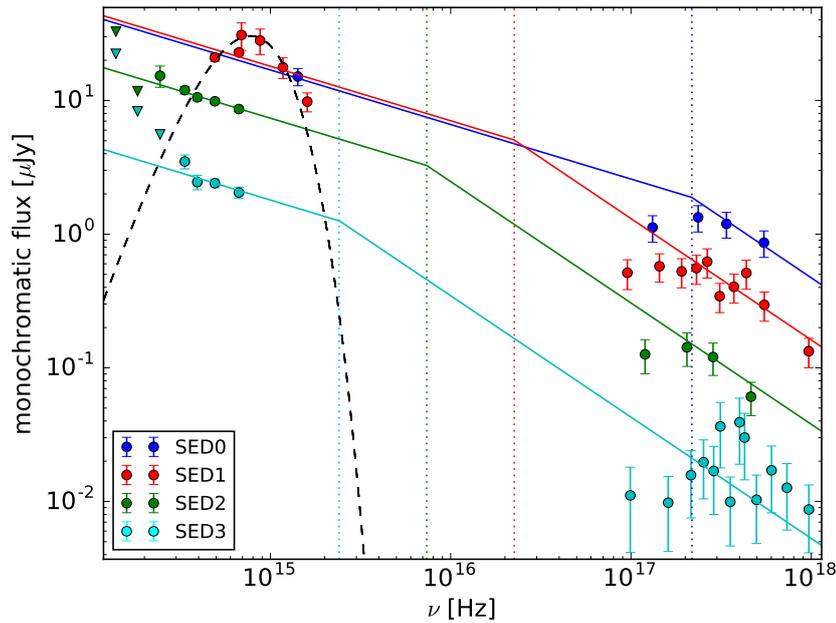
Figure 5.3.: Broad band fit of 4 SEDs during the time bins indicated in Fig. 5.2. All 4 SEDs share the same spectral slopes. One can see a characteristic frequency evolving towards the low energy part of the spectrum. The dashed black line is black body emission with 7500K. A black body could contribute to the optical part of the SED, without diluting the X-ray (see Sec. 5.4.3).

without extinction and absorption) are shown in Fig. 5.3. All results of my analysis for α and β are given in Tab. 5.2. A summary of the physical values from the spectral fitting is summarized in Tab. 5.1.

The radio detection from Fong (2015) at time $t_{\text{SED2}} = 57900\,\text{s}$ allows us to constrain the peak of the SED, and both characteristic frequencies (see Fig. 5.4). For the spectral slope below the maximum frequency I assume the standard fireball $\beta = -1/3$, the other spectral slopes are the ones derived in the multi-SED fit.

Fig. 5.5 shows the evolution of the characteristic frequencies based on my 4 SEDs, and the evolution of the characteristic frequencies according to some physical models, respectively, which I will discuss in Sec. 5.4.

Table 5.1.: Additional data for the GRB

	150424A	reference
Galactic E(B-V)[mag]	0.051 ± 0.002	Schlafly & Finkbeiner (2011)
Galactic N_H $[10^{21}cm^{-2}]$	0.60	Kalberla et al. (2005)
z	$1.0^{+0.3}_{-0.2}$	afterglow photometry
$d_L[10^{28}cm]$	2.1	from z
Host E(B-V) [mag]	$0.0^{+1.5}_{-0.0}$	SED fit
Host N_H $[10^{22}cm^{-2}]$	$0.04^{+0.24}_{-0.04}$	SED fit
R_V	3.08 (MW)	assumption
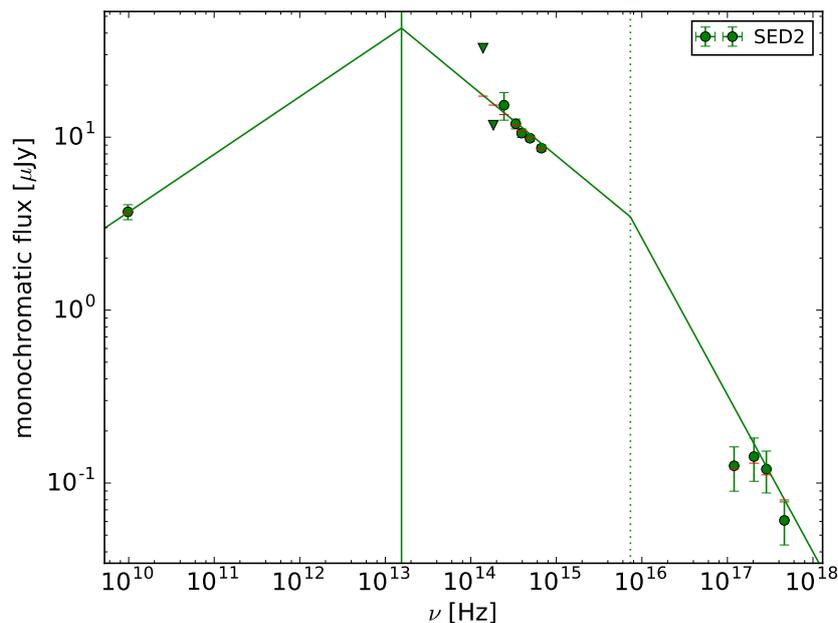
Figure 5.4.: SED2 $t_{\text{SED2}} = 57900\,\text{s}$ after the trigger. The radio detection allows us to determine the peak frequency of the spectrum, using a spectral slope $\beta = -1/3$ below the peak frequency, and the spectral slope derived in the multi SED fit.

5.3.2. Closure Relations

Within the fireball model (Mészáros & Rees 1997a, review e.g. Piran 2004; van Eerten 2015) a GRB afterglow is explained as synchrotron radiation of shock accelerated electrons from an ultra-relativistic outflow hitting the circumburst medium. In a dynamical afterglow model one can link the temporal and spectral behavior of an afterglow over a set of so-called *closure relations* between α and β. They depend on the state and structure (isotropic or jet) of the outflow, the circumburst density profile, and the energy distribution of the electrons.

The dynamics of the relativistic outflow is influenced by the circumburst medium. 2 scenarios are usually distinguished. First, the *Interstellar Medium (ISM) case*, where the circumburst medium is assumed to be homogeneous. Second, the *stellar wind case*, where the circumburst medium has radial density profile $n = n_0(R/R_0)^{-2}$, with a reference density n_0 and a reference radius R_0.

A synchrotron spectrum is conveniently characterized by characteristic frequencies: The injection frequency ν_m, which derives from the peak of the electron energy distribution, and the cooling frequency ν_c above which the electrons loose a significant amount of energy via synchrotron cooling. The *slow-cooling* case is defined as $\nu_m < \nu_c$, the *fast-cooling* case is defined as $\nu_m > \nu_c$.

I compare the fitted α and β to the theoretical closure relations collected by Racusin et al. (2009) (from Zhang & Mészáros 2004; Zhang et al. 2006; Dai &
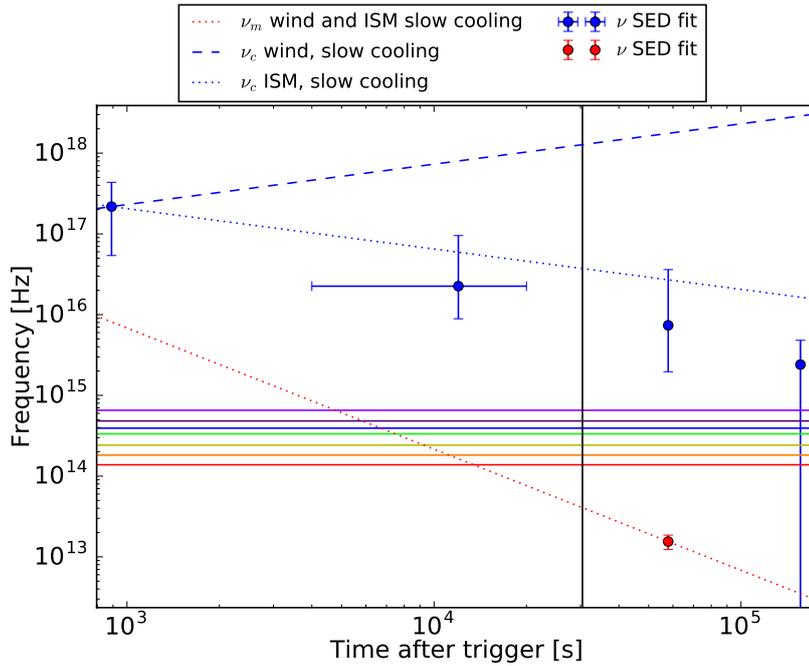
Figure 5.5.: Evolution of the characteristic frequencies from the SED fit and the standard fireball model. The horizontal lines are the GROND bands. The vertical black line corresponds to the optical break time. The blue data points are the break frequencies of the multi SED fit. The red data point is the peak frequency of the fit of SED2. The dashed and dotted lines are the evolutions of the characteristic frequencies according to different fireball scenarios.

Cheng 2001; Panaitescu et al. 2006; Panaitescu 2005 and expanded, see Tab. 2.1). I will abbreviate the closure relations with CR 1-14 from now. I follow this scheme: I use the β value fitted to the data. Then I calculate $p(\beta)$. In Racusin et al. (2009) there are multiple ways to calculate α. They differ if $p > 2$ or $p < 2$, and if I want to consider energy injection. I first calculate $\alpha(\beta)$ without energy injection. If the calculated α is consistent with the α I fitted to the data, I consider it a "plausible scenario". If not, I calculate the energy injection index $q(\alpha, \beta)$. q is defined over

$$L_{\mathrm{inj}}(t) = L_0(t/t_b)^{-q} \tag{5.1}$$

and is valid for $q \leqslant 1$. L_{inj} is the luminosity injected into the blast wave. The time t and break time t_b are given in the observer frame. $q = 1$ is the impulsive injection case, and $q = 0$ corresponds to a constant energy injection from e.g. a magnetar spin-down (Zhang et al. 2006). I check all $\alpha - \beta$ pairs from the phenomenological analysis (Tab. 5.2). In Tab. B.1 I list all closure relations that describe my afterglow, and the q values if needed.

In the SED fits I saw a break between the spectral regimes, so a set of closure relations can just be consistent with both spectral regimes if I find closure relations that

Table 5.2.: Summary of the phenomenological analysis. Temporal slopes α and spectral slopes β as defined in Eq. 2.33.

GRB	Optical		X-rays		
	α	β	α	β	
150424A	0.00 ± 0.01	$0.41^{+0.11}_{-0.07}$	0.58 ± 0.07	$0.91^{+0.11}_{-0.07}$	$t < t_{\text{break}}$
	1.42 ± 0.05	$0.41^{+0.11}_{-0.07}$	1.66 ± 0.26	$0.91^{+0.11}_{-0.07}$	$t > t_{\text{break}}$
	smoothness: 15.0 ± 13.8		smoothness: 1.0 ± 0.8		
	$t_{\text{break,opt}}$		$t_{\text{break,xrt}}$		
	$30.4 \pm 0.9\,\text{ks}$		$81.8 \pm 49.7\,\text{ks}$		

lie on different sides of a characteristic frequency, and describe the same scenario. After the break I just consider scenarios without energy injection to be plausible.

I find only one scenario that describes both spectral regimes (optical and X-ray), before and after the break: A uniform non-spreading jet in an ISM environment. After the temporal break the scenario is consistent with the optical data (CR11, $\nu_m < \nu < \nu_c$) and the X-ray (CR12, $\nu > \nu_c$), without the need for energy injection. Before the temporal break, the optical data implies the need for energy injection with an injection index $q_{\text{opt}} = 0.06 \pm 0.07$, and the X-ray data imply a different $q_x = 0.14 \pm 0.11$.

5.3.3. Redshift and Host

Using the extinction corrected SED1, I obtain the redshift from the afterglow as described by Krühler et al. (2011), and find $z = 1.0^{+0.3}_{-0.2}$. Using a standard ΛCDM cosmology with $H_0 = 67.3\,\text{km}\,\text{s}^{-1}\text{Mpc}^{-1}$, $\Omega_m = 0.315$, $\Omega_\Lambda = 0.685$ (Planck Collaboration 2014), this corresponds to a distance modulus of 44.2 mag, and a luminosity distance of $d_L = 2.1 \times 10^{28}\,\text{cm}$.

I note that the both the size (<1", corresponding to <8 kpc diameter) and absolute luminosity ($M_B \sim -17.2 \pm 0.5$ mag) of the host are very unusual for short-duration GRBs.

5.3.4. The Plausibility of a Magnetar Central Engine

During the merging process, the two neutron stars can either collapse directly into a black hole, or form a strongly magnetized and rapidly rotating neutron star: a magnetar (Duncan & Thompson 1996; Yi & Blackman 1997; Metzger et al. 2008; Zhang & Mészáros 2001). A magnetar would lose energy via dipole radiation and could provide a prolonged energy injection to the GRB and its afterglow.

Zhang & Mészáros (2001) suggested a magnetar model as short GRB progenitor. According to that model the magnetic field strength B_{0p} at the poles of a magnetar is linked to its spin down luminosity L_{sd}, and the initial spin period P_0 of the magnetar is linked to the spin-down time of the magnetar τ:

$$B_{0p,15}^2 = 4.20 \, I_{45}^2 R_6^{-6} L_{\text{sd},49}^{-1} \tau_{\text{sd},3}^{-2} \tag{5.2}$$

$$P_{0,-3}^2 = 2.05 \, I_{45} L_{\text{sd},49}^{-1} \tau_{\text{sd},3}^{-1} \tag{5.3}$$

with the moment of inertia I_{45} in 10^{45}g cm^2. The spin down luminosity of the magnetar $L_{\text{sd},49}$ is given in in 10^{49} erg/s. $B_{0p,15}$ is in units of 10^{15} Gauss. In the special case of an EE short GRB, P_0 corresponds to the spin period after EE (Zhang et al. 2007; Gompertz et al. 2013), rather than the spin down period when formed. $\tau_{\text{sd},3}$ is the spin-down energy release time scale in units of 10^3 s, which corresponds to my plateau end time, respectively break time $t_{\text{break,xrt}}$. Following Zhang & Mészáros (2001) I adopt a radius of the neutron star $R_6 = 10^6$ cm and a neutron star mass $m = 1.4 M_\odot$, which leads to $I = 1.85 \times 10^{45} \text{ g cm}^2$.

The efficiency with which $L_{\text{sd},49}$ is converted to the afterglow luminosity L_X is

$$L_X \equiv \eta_1 L_{\text{BOL}} \equiv \eta_1 \eta_2 L_{\text{inj}} \equiv \eta_{12} L_{\text{inj}} \equiv \eta_{12} L_{\text{sd}} \tag{5.4}$$

with the bolometric afterglow luminosity L_{BOL}, the luminosity injected into the blast wave L_{inj}, the observed luminosity L_X, and the corresponding efficiency factors η. I assume that all the magnetar spin-down luminosity is injected into the blast wave $L_{\text{inj}} = L_{\text{sd}}$.

I assume η_{12} to be constant in time, while it generally is expected to be time dependent, since the characteristic quantities of a synchrotron spectrum in the fireball model also evolve with time.

I use the break time $t_{\text{break,xrt}}$ of the X-ray light curve, and SED2 to calculate the rest frame luminosity at that time. Gompertz et al. (2013); Rowlinson et al. (2014); Rea et al. (2015) approximate the bolometric luminosity with the 1-10000keV band, extrapolated from Swift data. Using the LUMIN command of XSPEC and a dummy response leads to a luminosity $L_{1-10000 \text{ keV}} = 2.6 \times 10^{46} \text{ erg s}^{-1}$. When I integrate SED2 ($10^{-14} - 10^4 keV$) I find a similar $L_{0-10000 \text{ keV}} = 2.7 \times 10^{46} \text{ erg s}^{-1}$. Using $L_{0-10000 \text{ keV}}$ and assuming a 10% error in the luminosity, and $\eta_{12} = 1$ this results in magnetar parameters $B_{0p} = (0.9 \pm 0.5) \times 10^{15} G$ and $P_0 = 4.3 \pm 1.3 \text{ ms}$.

Since naturally $\eta_{12} < 1$ my values for B_{0p} and P_0 therefore have to be seen as limits. Moreover, a $\eta_{12} = 1$ would mean that all the injected luminosity is radiated away immediately, and nothing goes into the kinetic energy of the outflow. The fireball model therefore just can be self-consistent when $\eta_{12} << 1$.

My P_0 lies above the mass-shedding limit $P_0 = 0.81\,\mathrm{ms}$ (Lattimer & Prakash 2004) below which a neutron star would be disrupted due to centrifugal forces. For my fitted $t_{\mathrm{break,xrt}}$, the mass-shedding limit is reached when the $L_{\mathrm{sd,max}} > (7 \pm 4) \times 10^{47}\,\mathrm{erg/s}$. This yields a $\eta_{12} \gtrsim 4\%$.

The isotropic energy in the γ band is

$$E_{\gamma,\mathrm{iso}} = f_\gamma \times d_L(z)^2 4\pi \times (1 + z)^{-1} \tag{5.5}$$

with the γ-fluence $f_\gamma = 15(1) \times 10^{-7}\,\mathrm{erg\,cm^{-2}}$ measured by the Swift/BAT [5] and the luminosity distance d_L, follows $E_{\gamma,\mathrm{iso}} = 4.1 \times 10^{51}\,\mathrm{erg}$. $E_{\gamma,\mathrm{iso}}$ is a proxy for the impulsive energy input into the the blast wave (Granot et al. 2006). The prolonged energy injected is the luminosity at the end of the plateau times the length of the plateau. The sum of both is the total energy of the blast wave $E_{\mathrm{tot}} = E_{\gamma,\mathrm{iso}} + t_{\mathrm{break,xrt}} \times L_{0-10000\,\mathrm{keV}} = (6.3 \pm 1.4) \times 10^{51}$ erg and does not exceed the limits for the maximal rotational energy of a proto magnetar of $(1 - 2) \times 10^{53}$erg suggested by Metzger et al. (2015).

5.4. Discussion

5.4.1. General Description

The X-ray light curve of GRB 150424A shows a steep decay from the prompt emission followed by a smoothly broken power law. GRB 150424A seems to be a typical EE short GRB (Gompertz et al. 2013). This GRB becomes special since it is one of the rare cases with an early multi-epoch optical coverage, during which the optical emission is basically constant for 8 hrs. While the temporal break in the optical is very sharp, the break of the X-ray light curve is more smooth, yet the breaks occur around the same time. This is a strong indicator that the underlying dynamics changes at that point in time, i.e. the end of the optical plateau.

Studies concerning the relation between the end time of a plateau and the luminosity at the end of the plateau (Dainotti et al. 2008; Li et al. 2012; Dainotti et al. 2013) show that the afterglow of GRB 150424A represents a "typical" shallow decay afterglow. As seen in Fig. 5.6 the afterglow does not have an outstanding position in the plateau end time - luminosity parameter space, which was originally established for long GRBs.

---

[5]http://swift.gsfc.nasa.gov/archive/grb_table.html
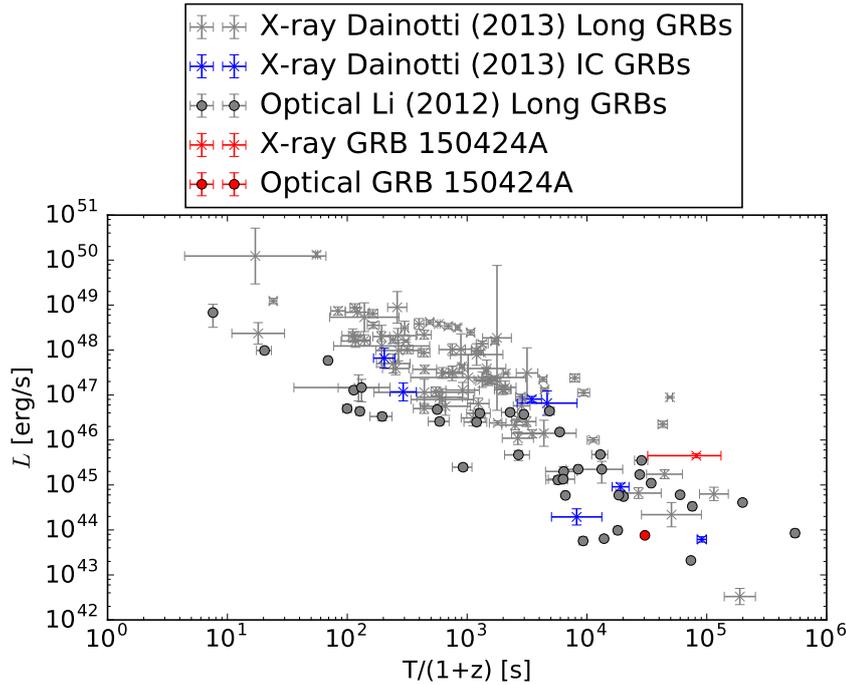
Figure 5.6.: Plateau end time luminosity correlations. The X-ray data for long GRBs and EE short GRBs (tagged as Intermediate Class (IC) GRBs) is taken from Dainotti et al. (2013) (grey and blue crosses). The optical data comes from Li et al. (2012) (grey circles). The afterglow of GRB 150424A does not show any special behaviour, whether in the optical (red circle), nor in the X-ray (red cross).

5.4.2. Physical Interpretation

With an electron distribution index ~ 2, an optical spectral slope $\sim 1/2$ and an X-ray spectral slope ~ 1, the spectral fits do not allow me to distinguish between a slow or fast cooling case, using the spectral shapes given by Sari et al. (1998).

In Sec. 5.3.2 I tested the derived spectral and temporal slopes with the most common closure relations (see Tab. B.1), and now will present my findings. In Sec. 5.4.3 and Sec. 5.4.4 I discuss two standard afterglow scenarios, and in Sec. 5.4.5 a scenario with energy injection involved.

5.4.3. Scenario 1: ISM, Slow Cooling

The spectral shape of SED2 is compatible with slow cooling in an ISM, and would allow me to constrain ν_m (see Fig. 5.4). The temporal evolution of ν_c also fits the observation (blue dotted line and blue resp. red dots in Fig. 5.5).

The spectral shape from my SED fits shows that the X-ray data lies well above the cooling break. However, the X-ray data by itself can only be explained by closure relations for slow cooling in the ISM when the observed X-ray frequency would be $\nu_m < \nu_{\text{X-ray}} < \nu_c$ (CR1), with energy injection before the break and no energy injection after the break. The SED fits and the closure relation CR1 for the X-ray
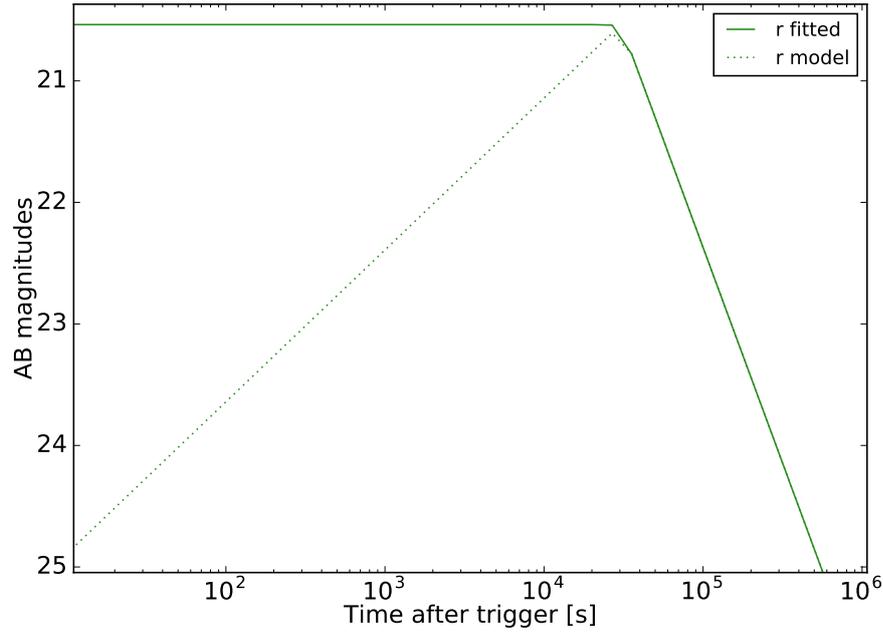
Figure 5.7.: r band light curve for scenario 1. The solid line is the fit of the light curve, the dashed line is the hypothetical model light curve for an ISM and observer frequency below ν_m, with a temporal slope $\alpha = -1/2$.

light curve therefore contradict each other.

Being agnostic about the spectral shape of an afterglow in the optical opens another line of thought. In Fig. 5.7 I show the fitted (solid) optical light curve and the hypothetical (dotted) light curve under the assumption that ν_m crosses the observational band at the break time. The deviation between fitted and hypothetical light curve would imply the need for an additional emission component at early times. Black body emission with temperature $T_{\mathrm{BB}} \sim 7500\,\mathrm{K}$ may contribute to the optical emission and not dilute the X-rays (see black dashed line in Fig. 5.3), but it is very unlikely that thermal emission from an electron population behaves in a way that their emission combined with the synchrotron emission from the relativistic outflow form a completely flat plateau over such a long time range. A synchrotron signature from such a thermal population is expected to emit at energies lower than the optical (Eichler & Waxman 2005).

5.4.4. Scenario 2: Slow Cooling in Wind Without Energy Injection

Granot & Sari (2002) give a temporal slope $\alpha = 0$ for this scenario when the observer frequency $\nu < \nu_m$, so the optical plateau could be explained if ν_m is above the optical frequencies. The spectral shape I observe does not rule out this scenario. If I extrapolate from SED2 and follow the temporal evolution $\nu_m \propto t^{-3/2}$ I find

that it would cross my observed bands at the time of SED1 (red dotted line in Fig. 5.5), before the temporal break in the optical. In my SED fits, SED0 has just one UVOT-white band data point, and for SED1 I had to use a wide time bin for the optical part of the SED. A ν_m crossing at that point in time may therefore not be detectable by my spectral fitting, but it should coincide with the end of the plateau.

Before the break the X-ray data is not consistent with this scenario (to fulfill CR5 or CR6 in Tab. B.1 energy injection has to be accounted for). After the break it is consistent when $\nu_m < \nu_{\mathrm{X-ray}} < \nu_c$ (CR5). However my SED fit shows that the fitted ν_c is well below the X-ray (blue dots in Fig. 5.5), and that the evolution of the break frequency does not follow the predicted evolution for ν_c in this scenario (see blue dashed line and blue data points in Fig. 5.5).

5.4.5. Scenario 3: Uniform Nonspreading Jet in ISM with Energy Injection

The closure relations for a uniform nonspreading jet in an ISM medium with slow cooling are valid for all temporal and spectral regimes (the optical is consistent with CR11, the X-ray is consistent with CR12). Before the temporal break energy injection is needed; After the temporal break it is consistent with both spectral regimes without energy injection. I derived an efficiency to convert the spin-down luminosity of the magnetar to the total afterglow luminosity $\eta_{12} \gtrsim 4\%$. The used model specifically, and generally all models that assume an adiabatic blast wave, harmonize with a 4% loss due to radiation.

I derived the energy injection index q independently from the optical and the X-ray data. Both q values are consistent with a constant energy injection (q=0), as expected from a magnetar.

5.5. Conclusions

I presented multi-band data with a uniquely high temporal and spectral coverage of the EE short GRB 150424A. I did a phenomenological analysis and interpreted them in the context of the fireball model. I found 3 scenarios that explain parts of the temporal and spectral behaviour of the afterglow.

1. Slow cooling in an ISM

2. Slow cooling in wind without energy injection

3. A uniform nonspreading jet in an ISM medium with energy injection

I found that typical standard scenarios of GRB afterglows, i.e. slow cooling in an ISM or wind environment, are not able to explain my data.

In contrast, a uniform, non-spreading jet expanding into an ISM medium and re-powered for $\approx 10^4$s with additional constant energy injection can explain the data. This means, however, that the jet break already has to have had happened before the plateau begins, before the first optical data point $t_{\rm jb} \lesssim 100$ s. Otherwise the jet nature of the outflow would not be detectable by the analysis. Assuming an on-axis observation in an ISM Eq. 4.3 implies a $\theta_0 \lesssim 0.01$ rad. The jet opening angle would have to be an order of magnitude smaller than the opening angles from sample analysis of other afterglows (see Chapter 4).

For a magnetar as supplier of prolonged energy injection an efficiency $\eta_{12} \gtrsim 4\%$ in converting the spin-down luminosity of the magnetar $L_{\rm sd}$ to the afterglow luminosity has to be assumed. However, the local magnetar rate is not in a agreement with the GRB rate (Rea et al. 2015).

The unique and very-long-duration energy injection provides, within a factor of 2, a similar energy input into the surrounding as the prompt GRB emission. Yet, the total energy release is a factor of 20 below the maximum possible for a magnetar. It is interesting to note that this short-duration GRB has an energy output typical of long duration GRBs.

CHAPTER 6

SUMMARY

In Chapter 1 and Chapter 2 I gave an overview of GRB history, followed by a quantitative introduction of the fireball model. I clarified the basic concepts, assumptions, capabilities and limitations of the fireball model.

In Chapter 3 I analysed afterglow data of GRB 081121A, a relatively simple afterglow, characterized by a smoothly curved light curve without any particular feature. The data served as an excellent "textbook" example to compare different analysis methods and implementations of the fireball model. I uncovered degeneracies between some of the fireball parameters, that occur when just ν_c and ν_m are present as observables. I also motivated a reinterpretation of ϵ_e, to deal with very high non-physical best fitting values for ϵ_e and high energy cut-offs in the electron energy distribution.

Moreover, I introduced SCALEFIT (Van Eerten in prep., Ryan et al. 2015), and applied it for the first time to multi-band data. SCALEFIT implements a MCMC approach, that enables the user to explore the whole PDF of model parameters, given the data. The software also provides an afterglow model, that bases on 2D hydro-dynamical simulations. Those simulations handle the dynamics of the outflow in high detail, and allow to constrain the jet opening angle θ_0, even without a jet break, and without knowledge of the other fireball parameters. The simulations also open the new possibility to derive the observer angle.

In Chapter 3 I applied SCALEFIT to a sample of short GRB afterglows. Fong et al. (2015) gave 4 estimates and 7 limits for the GRB jet opening angles. With SCALEFIT I expanded the list to 12 estimates and 2 limits of the jet opening angle and 14 estimates of the observer angle.

I found that short GRBs have a median opening angle $\theta_0 = 0.12^{+0.07}_{-0.06}$ and a median observer angle $\theta_{\rm obs,short}/\theta_0 = 0.6^{+0.1}_{-0.4}$. The distribution of the angles does not differ significantly from the distribution of the angles of long GRBs.

In Chapter 5 I analyzed data of the particularly interesting GRB 150424A, an EE short GRB with a long optical plateau. I presented a high quality data-set, which so far is unique in temporal and spectral coverage. I found that within the fireball model a uniform, non-spreading jet expanding into an ISM medium and re-powered for $\approx 10^4\,$s with additional constant energy injection can explain the data self-consistently.

For a magnetar as supplier of this prolonged energy injection an efficiency $\eta_{12} \gtrsim 4\%$ in converting the spin-down luminosity of the magnetar L_{sd} to the afterglow luminosity has to be assumed.

BIBLIOGRAPHY

Aasi, J., Abadie, J., Abbott, B. P., et al. 2015, Classical and Quantum Gravity, 32, 115012

Abdo, A. A., Ackermann, M., Arimoto, M., et al. 2009, Science, 323, 1688

Acernese, F., Agathos, M., Agatsuma, K., et al. 2015, Classical and Quantum Gravity, 32, 024001

Aloy, M. A., Janka, H.-T., & Müller, E. 2005, A&A, 436, 273

Arnaud, K. A. 1996, in Astronomical Society of the Pacific Conference Series, Vol. 101, Astronomical Data Analysis Software and Systems V, ed. G. H. Jacoby & J. Barnes, 17

Atteia, J.-L., Barat, C., Hurley, K., et al. 1987, ApJ, 64, 305

B. Rybicki, G. & P. Lightman, A. 1979, Radiative Processes in Astrophysics (Wiley)

Band, D., Matteson, J., Ford, L., et al. 1993, ApJ, 413, 281

Bardho, O., Gendre, B., Rossi, A., et al. 2016, ArXiv e-prints

Barniol Duran, R., Leng, M., & Giannios, D. 2016, MNRAS, 455, L6

Barthelmy, S. D., Baumgartner, W. H., Beardmore, A. P., et al. 2015, GRB Coordinates Network, 17761

Beardmore, A. P., Page, K. L., Evans, P. A., et al. 2009, GRB Coordinates Network, 8937

Beardmore, A. P., Page, K. L., Palmer, D. M., & Ukwatta, T. N. 2015, GRB Coordinates Network, 17743, 1

Bégué, D. & Burgess, J. M. 2016, ApJ, 820, 68

Behroozi, P. S., Ramirez-Ruiz, E., & Fryer, C. L. 2014, ApJ, 792, 123

Belczynski, K., Perna, R., Bulik, T., et al. 2006, ApJ, 648, 1110

Beniamini, P. & Kumar, P. 2016, MNRAS, 457, L108

Berger, E. 2007, ApJ, 670, 1254

Berger, E. 2010, ApJ, 722, 1946

Berger, E. 2014, Annual review of astronomy and astrophysics, 52, 43

Berger, E., Cenko, S. B., Fox, D. B., & Cucchiara, A. 2009, ApJ, 704, 877

Berger, E., Kulkarni, S. R., & Frail, D. A. 2004, ApJ, 612, 966

Berger, E. & Rauch, M. 2008, GRB Coordinates Network, 8542, 1

Blackburn, J. K. 1995, in Astronomical Society of the Pacific Conference Series,
    Vol. 77, Astronomical Data Analysis Software and Systems IV, ed. R. A. Shaw,
    H. E. Payne, & J. J. E. Hayes, 367

Blandford, R. & Eichler, D. 1987, Physics Reports, 154, 1

Blandford, R. D. & McKee, C. F. 1976, Physics of Fluids, 19, 1130

Burrows, D. N., Hill, J. E., Nousek, J. A., et al. 2005, Space science reviews, 120,
    165

Cardelli, J. A., Clayton, G. C., & Mathis, J. S. 1989, ApJ, 345, 245

Castro-Tirado, A. J., Sanchez-Ramirez, R., Lombardi, G., & Rivero, M. A. 2015,
    GRB Coordinates Network, 17758

Cavallo, G. & Rees, M. J. 1978, MNRAS, 183, 359

Cenko, S. B., Frail, D. A., Harrison, F. A., et al. 2010, ApJ, 711, 641

Chandra, P., Cenko, S. B., Frail, D. A., et al. 2008, ApJ, 683, 924

Church, R. P., Levan, A. J., Davies, M. B., & Tanvir, N. 2011, MNRAS, 413, 2004

Clark, J., Evans, H., Fairhurst, S., et al. 2015, ApJ, 809, 53

Connaughton, V., Burns, E., Goldstein, A., et al. 2016, ArXiv e-prints

Costa, E., Frontera, F., Heise, J., et al. 1997, Nature, 387, 783

Cucchiara, A., Levan, A. J., Fox, D. B., et al. 2011, ApJ, 736, 7

Cutler, C., Apostolatos, T. A., Bildsten, L., et al. 1993, Phys. Rev. Lett., 70, 2984

Dado, S., Dar, A., & De Rújula, A. 2002, ApJ, 572, L143

Dado, S., Dar, A., & De Rújula, A. 2003, ApJ, 585, 890

Dai, Z. G. & Cheng, K. S. 2001, ApJ, 558, L109

Dai, Z. G. & Lu, T. 2002, ApJ, 565, L87

Dainotti, M. G., Cardone, V. F., & Capozziello, S. 2008, MNRAS, 391, L79

Dainotti, M. G., Petrosian, V., Singal, J., & Ostrowski, M. 2013, ApJ, 774, 157

D'Avanzo, P. & Ghirlanda, G. 2016, LPI Contributions, 1962, 4031

D'Avanzo, P., Malesani, D., Covino, S., et al. 2009, A&A, 498, 711

de Ugarte Postigo, A., Thöne, C. C., Rowlinson, A., et al. 2014, A&A, 563, A62

Dermer, C. D., Böttcher, M., & Chiang, J. 1999, ApJ, 515, L49

Dickey, J. M. & Lockman, F. J. 1990, Annual review of astronomy and astrophysics,
    28, 215

Drenkhahn, G. & Spruit, H. C. 2002, A&A, 391, 1141

Duffell, P. C., Quataert, E., & MacFadyen, A. I. 2015, ApJ, 813, 64

Duncan, R. C. & Thompson, C. 1996, in American Institute of Physics Confer-
    ence Series, Vol. 366, High Velocity Neutron Stars, ed. R. E. Rothschild & R. E.
    Lingenfelter, 111–117

Eichler, D., Livio, M., Piran, T., & Schramm, D. N. 1989, Nature, 340, 126

Eichler, D. & Waxman, E. 2005, ApJ, 627, 861

Evans, P. A., Beardmore, A. P., Page, K. L., et al. 2009, MNRAS, 397, 1177

Fan, Y.-Z., Yu, Y.-W., Xu, D., et al. 2013, ApJ, 779, L25

Fermi, E. 1949, Physical Review, 75, 1169

Filgas, R., Greiner, J., Schady, P., et al. 2011, A&A, 535, A57

Fishman, G. J., Meegan, C. A., Wilson, R. B., et al. 1994, ApJ, 92, 229

Fong, W. 2015, GRB Coordinates Network, 17804

Fong, W. & Berger, E. 2013, ApJ, 776, 18

Fong, W., Berger, E., Chornock, R., et al. 2013, ApJ, 769, 56

Fong, W., Berger, E., & Fox, D. B. 2010, ApJ, 708, 9

Fong, W., Berger, E., Margutti, R., & Zauderer, B. A. 2015, ApJ, 815, 102

Fong, W., Berger, E., Margutti, R., et al. 2012, ApJ, 756, 189

Foreman-Mackey, D., Hogg, D. W., Lang, D., & Goodman, J. 2013, ASP , 125, 306

Foreman-Mackey, D., Price-Whelan, A., Ryan, G., et al. 2014, triangle.py v0.1.1

Frail, D. A., Kulkarni, S. R., Sari, R., et al. 2001, ApJ, 562, L55

Gat, I., van Eerten, H., & MacFadyen, A. 2013, ApJ, 773, 2

Gehrels, N., Barthelmy, S. D., Burrows, D. N., et al. 2008, ApJ, 689, 1161

Gehrels, N., Piro, L., & Leonard, P. J. T. 2002, Scientific American, 287

Ghirlanda, G., Nava, L., Ghisellini, G., Celotti, A., & Firmani, C. 2009, A&A, 496, 585

Ghisellini, G. 2013, Radiative Processes in High Energy Astrophysics, Lecture Notes in Physics (Springer International Publishing)

Goad, M. R., Osborne, J. P., Beardmore, A. P., & Evans, P. A. 2008, GRB Coordinates Network, 8541, 1

Godet, O. & Oates, S. 2008, GRB Coordinates Network, 8543, 1

Golenetskii, S., Aptekar, R., Mazets, E., et al. 2008, GRB Coordinates Network, 8548

Gompertz, B. P., O'Brien, P. T., Wynn, G. A., & Rowlinson, A. 2013, MNRAS, 431, 1745

Goodman, J. 1986, ApJ, 308, L47

Granot, J., Königl, A., & Piran, T. 2006, MNRAS, 370, 1946

Granot, J. & Piran, T. 2012, MNRAS, 421, 570

Granot, J., Piran, T., & Sari, R. 1999, ApJ, 527, 236

Granot, J. & Sari, R. 2002, ApJ, 568, 820

Greiner, J., Bornemann, W., Clemens, C., et al. 2008, ASP , 120, 405

Greiner, J., Krühler, T., Klose, S., et al. 2011, A&A, 526, A30

Greiner, J., Mazzali, P. A., Kann, D. A., et al. 2015, Nature, 523, 189

Hjorth, J., Sollerman, J., Gorosabel, J., et al. 2005a, ApJ, 630, L117

Hjorth, J., Watson, D., Fynbo, J. P. U., et al. 2005b, Nature, 437, 859

Iwamoto, K., Mazzali, P. A., Nomoto, K., et al. 1998, Nature, 395, 672

Kagan, D., Sironi, L., Cerutti, B., & Giannios, D. 2015, Space science reviews, 191, 545

Kalberla, P. M. W., Burton, W. B., Hartmann, D., et al. 2005, A&A, 440, 775

Kann, D. A., Klose, S., Zhang, B., et al. 2011, ApJ, 734, 96

Kann, D. A., Tanga, M., & Greiner, J. 2015, GRB Coordinates Network, 17757, 1

Kaplan, D. L., Rowlinson, A., Bannister, K. W., et al. 2015, ApJ, 814, L25

Klebesadel, R. W., Strong, I. B., & Olson, R. A. 1973, ApJ, 182, L85

Kocevski, D. & Butler, N. 2008, ApJ, 680, 531

Kouveliotou, C., Meegan, C. A., Fishman, G. J., et al. 1993, ApJ, 413, L101

Krühler, T., Küpcü Yoldaş, A., Greiner, J., et al. 2008, ApJ, 685, 376

Krühler, T., Schady, P., Greiner, J., et al. 2011, A&A, 526, A153

Kulkarni, S. R., Djorgovski, S. G., Ramaprakash, A. N., et al. 1998, Nature, 393, 35

Kumar, P. & Barniol Duran, R. 2010, MNRAS, 409, 226

Laskar, T., Alexander, K. D., Berger, E., et al. 2016, ApJ, 833, 88

Laskar, T., Berger, E., Margutti, R., et al. 2015, ApJ, 814, 1

Lattimer, J. M. & Prakash, M. 2004, Science, 304, 536

Leventis, K., van Eerten, H. J., Meliani, Z., & Wijers, R. A. M. J. 2012, MNRAS, 427, 1329

Li, L., Liang, E.-W., Tang, Q.-W., et al. 2012, ApJ, 758, 27

Lithwick, Y. & Sari, R. 2001, ApJ, 555, 540

Loew, S., Kruehler, T., & Greiner, J. 2008, GRB Coordinates Network, 8540, 1

Marshall, F. E. & Beardmore, A. P. 2015, GRB Coordinates Network, 17751, 1

Matz, S. M., Forrest, D. J., Vestrand, W. T., et al. 1985, ApJ, 288, L37

Mazets, E. P., Aptekar, R. L., Frederiks, D. D., et al. 2002, ArXiv Astrophysics e-prints

Mazets, E. P., Golenetskii, S. V., Ilinskii, V. N., et al. 1981, APSS, 80, 3

Meegan, C., Fishman, G., Wilson, R., et al. 1993, in American Institute of Physics Conference Series, Vol. 280, American Institute of Physics Conference Series, ed. M. Friedlander, N. Gehrels, & D. J. Macomb, 681–685

Meszaros, P., Laguna, P., & Rees, M. J. 1993, ApJ, 415, 181

Mészáros, P., Ramirez-Ruiz, E., Rees, M. J., & Zhang, B. 2002, ApJ, 578, 812

Meszaros, P. & Rees, M. J. 1992, ApJ, 397, 570

Meszaros, P. & Rees, M. J. 1993, ApJ, 405, 278

Mészáros, P. & Rees, M. J. 1997a, ApJ, 476, 232

Mészáros, P. & Rees, M. J. 1997b, ApJ, 482, L29

Mészáros, P., Rees, M. J., & Wijers, R. A. M. J. 1998, ApJ, 499, 301

Metzger, B. D., Margalit, B., Kasen, D., & Quataert, E. 2015, MNRAS, 454, 3311

Metzger, B. D., Quataert, E., & Thompson, T. A. 2008, MNRAS, 385, 1455

Metzger, M. R., Djorgovski, S. G., Kulkarni, S. R., et al. 1997, Nature, 387, 878

Mundell, C. G., Kopač, D., Arnold, D. M., et al. 2013, Nature, 504, 119

Murguia-Berthier, A., Ramirez-Ruiz, E., Montes, G., et al. 2017, ApJ, 835, L34

Nakar, E. 2007, Physics Reports, 442, 166

Nakar, E. & Piran, T. 2017, ApJ, 834, 28

Narayan, R., McKinney, J. C., & Farmer, A. J. 2007, MNRAS, 375, 548

Narayan, R., Paczynski, B., & Piran, T. 1992, ApJ, 395, L83

Norris, J. P. & Bonnell, J. T. 2006, ApJ, 643, 266

Norris, J. P., Gehrels, N., & Scargle, J. D. 2010, ApJ, 717, 411

Nysewander, M., Fruchter, A. S., & Pe'er, A. 2009, ApJ, 701, 824

Oates, S. R., Baumgartner, W. H., Beardmore, A. P., et al. 2008, GRB Coordinates
    Network, 8537, 1

Paciesas, W. S., Meegan, C. A., Pendleton, G. N., et al. 1999, ApJ, 122, 465

Paczynski, B. 1986, ApJ, 308, L43

Paczynski, B. 1990, ApJ, 363, 218

Paczyński, B. 1998, ApJ, 494, L45

Paczynski, B. & Proszynski, M. 1986, ApJ, 302, 519

Panaitescu, A. 2005, MNRAS, 362, 921

Panaitescu, A. & Kumar, P. 2002, ApJ, 571, 779

Panaitescu, A. & Mészáros, P. 1998, ApJ, 501, 772

Panaitescu, A., Mészáros, P., Gehrels, N., Burrows, D., & Nousek, J. 2006, MNRAS,
    366, 1357

Pei, Y. C. 1992, ApJ, 395, 130

Perley, D. A., Bloom, J. S., Modjaz, M., et al. 2008, GRB Coordinates Network,
    7889

Perley, D. A. & McConnell, N. J. 2015, GRB Coordinates Network, 17745

Perley, D. A., Metzger, B. D., Granot, J., et al. 2009, ApJ, 696, 1871

Piran, T. 1999, Physics Reports, 314, 575

Piran, T. 2004, Reviews of Modern Physics, 76, 1143

Piranomonte, S., D'Avanzo, P., Covino, S., et al. 2008, A&A, 491, 183

Piro, L., Troja, E., Gendre, B., et al. 2014, ApJ, 790, L15

Planck Collaboration. 2014, A&A, 571, A16

Poole, T. S., Breeveld, A. A., Page, M. J., et al. 2008, MNRAS, 383, 627

Preece, R. D., Briggs, M. S., Mallozzi, R. S., et al. 2000, ApJ, 126, 19

Racusin, J. L., Liang, E. W., Burrows, D. N., et al. 2009, ApJ, 698, 43

Rea, N., Gullón, M., Pons, J. A., et al. 2015, ApJ, 813, 92

Rees, M. J. & Meszaros, P. 1992, MNRAS, 258, 41P

Rees, M. J. & Meszaros, P. 1994, ApJ, 430, L93

Resmi, L., Ishwara-Chandra, C. H., Castro-Tirado, A. J., et al. 2005, A&A, 440, 477

Rezzolla, L., Giacomazzo, B., Baiotti, L., et al. 2011, ApJ, 732, L6

Rhoads, J. E. 1997, ApJ, 487, L1

Rhoads, J. E. 1999a, A&A, 138, 539

Rhoads, J. E. 1999b, ApJ, 525, 737

Roming, P. W. A., Kennedy, T. E., Mason, K. O., et al. 2005, Space science reviews, 120, 95

Roming, P. W. A., Vanden Berk, D., Pal'shin, V., et al. 2006, ApJ, 651, 985

Rosswog, S. & Davies, M. B. 2002, MNRAS, 334, 481

Rosswog, S. & Ramirez-Ruiz, E. 2003, MNRAS, 343, L36

Rosswog, S., Ramirez-Ruiz, E., & Davies, M. B. 2003, MNRAS, 345, 1077

Rowlinson, A., Gompertz, B. P., Dainotti, M., et al. 2014, MNRAS, 443, 1779

Rueda Hernandez, J., Fryer, C., Muccino, M., & Ruffini, R. 2016, in APS Meeting Abstracts

Ryan, G., van Eerten, H., MacFadyen, A., & Zhang, B.-B. 2015, ApJ, 799, 3

Sari, R. 1997, ApJ, 489, L37

Sari, R. & Piran, T. 1995, ApJ, 455, L143

Sari, R., Piran, T., & Halpern, J. P. 1999, ApJ, 519, L17

Sari, R., Piran, T., & Narayan, R. 1998, ApJ, 497, L17

Scarsi, L. 1997, in Data Analysis in Astronomy, ed. V. Di Gesu, M. J. B. Duff, A. Heck, M. C. Maccarone, L. Scarsi, & H. U. Zimmerman, 65–78

Schady, P., Dwelly, T., Page, M. J., et al. 2012, A&A, 537, A15

Schlafly, E. F. & Finkbeiner, D. P. 2011, ApJ, 737, 103

Schlegel, D. J., Finkbeiner, D. P., & Davis, M. 1998, ApJ, 500, 525

Sedov, L. I. 1959, Similarity and Dimensional Methods in Mechanics (not available)

Stanek, K. Z., Matheson, T., Garnavich, P. M., et al. 2003, ApJ, 591, L17

Stratta, G., D'Avanzo, P., Piranomonte, S., et al. 2007, A&A, 474, 827

Swenson, C. A. & Bernardini, M. G. 2014, GRB Coordinates Network, 15780

Tanvir, N. R., Levan, A. J., Fruchter, A. S., et al. 2013, Nature, 500, 547

Tanvir, N. R., Levan, A. J., Fruchter, A. S., et al. 2015, GRB Coordinates Network, 18100

Taylor, G. 1950, Royal Society of London Proceedings Series A, 201, 159

Tody, D. 1993, in ASP Conference Series, Vol. 52, Astronomical Data Analysis Software and Systems II, ed. R. J. Hanisch, R. J. V. Brissenden, & J. Barnes, 173

Troja, E., Sakamoto, T., Cenko, S. B., et al. 2016, ApJ, 827, 102

van Eerten, H. 2014, MNRAS, 442, 3495

van Eerten, H. & MacFadyen, A. 2013, ApJ, 767, 141

van Eerten, H., van der Horst, A., & MacFadyen, A. 2012, ApJ, 749, 44

van Eerten, H., Zhang, W., & MacFadyen, A. 2010a, ApJ, 722, 235

van Eerten, H. J. 2015, Journal of High Energy Astrophysics, 7, 23

van Eerten, H. J., Leventis, K., Meliani, Z., Wijers, R. A. M. J., & Keppens, R. 2010b, MNRAS, 403, 300

van Eerten, H. J. & MacFadyen, A. I. 2012a, ApJ, 747, L30

van Eerten, H. J. & MacFadyen, A. I. 2012b, ApJ, 751, 155

van Paradijs, J., Groot, P. J., Galama, T., et al. 1997, Nature, 386, 686

Vedrenne, G. and Atteia, J.-L. 2009, Gamma-Ray Bursts: The brightest explosions in the Universe

Wanderman, D. & Piran, T. 2015, MNRAS, 448, 3026

Warren, D. C., Ellison, D. C., Barkov, M. V., & Nagataki, S. 2017, ApJ, 835, 248

Woosley, S. E. 1993, ApJ, 405, 273

Wygoda, N., Waxman, E., & Frail, D. A. 2011, ApJ, 738, L23

Yi, I. & Blackman, E. G. 1997, ApJ, 482, 383

Yoldaş, A. K., Krühler, T., Greiner, J., et al. 2008, in AIP Conf. Series, Vol. 1000, AIP Conference Series, ed. M. Galassi, D. Palmer, & E. Fenimore, 227–231

Yost, S. A., Harrison, F. A., Sari, R., & Frail, D. A. 2003, ApJ, 597, 459

Yu, H.-F., van Eerten, H. J., Greiner, J., et al. 2015, A&A, 583, A129

Zhang, B., Fan, Y. Z., Dyks, J., et al. 2006, ApJ, 642, 354

Zhang, B. & Mészáros, P. 2001, ApJ, 552, L35

Zhang, B. & Mészáros, P. 2004, International Journal of Modern Physics A, 19, 2385

Zhang, B., Zhang, B.-B., Liang, E.-W., et al. 2007, ApJ, 655, L25

Zhang, B.-B., van Eerten, H., Burrows, D. N., et al. 2015a, ApJ, 806, 15

Zhang, Q., Huang, Y.-F., & Zong, H.-S. 2015b, ApJ, 811, 83

Zhang, S., Jin, Z.-P., Wang, Y.-Z., & Wei, D.-M. 2017, ApJ, 835, 73

Zhang, W. & MacFadyen, A. 2009, ApJ, 698, 1261

Zhang, W. & MacFadyen, A. I. 2006, ApJ, 164, 255

Zhang, W., Woosley, S. E., & MacFadyen, A. I. 2003, ApJ, 586, 356

APPENDIX A

ADDITIONAL DATA FOR CHAPTER 4

Table A.1.: Fitting Results for data sets with less or equal 6 detections. There are more degrees of freedom in the model than data points. The values correspond to the position of the best walker.

GRB	r	o	x	n	θ_0	$\theta_{\mathrm{obs}}/\theta_0$	p
050202A	y	y	n	0	0.30	0.25	2.44
050509B	y	y	y	1	0.29	0.67	2.08
050813A	y	y	y	1	0.16	0.31	2.14
050906A	y	y	y	0	0.34	0.63	3.65
050925A	y	n	y	0	0.50	0.64	2.73
051105A	y	n	n	0	0.40	0.91	2.33
051210A	n	y	y	1	0.40	0.94	2.76
060502B	n	y	y	0	0.38	0.42	2.48
060801A	y	y	y	1	0.40	0.57	2.54
061210A	y	y	y	3	0.39	0.13	2.01
061217A	n	y	y	0	0.18	0.95	2.36
070209A	n	y	y	0	0.07	0.61	3.18
070406A	n	y	y	0	0.29	0.52	3.84
070429B	y	y	y	1	0.05	0.89	2.15
070729A	y	y	y	0	0.20	0.97	3.98
070810B	n	y	y	0	0.17	0.93	3.03
070923A	y	n	n	0	0.19	0.59	3.56
071017A	n	n	y	0	0.31	0.33	3.24
071112B	y	y	y	0	0.40	0.19	2.57
071227A	n	y	y	4	0.09	0.40	3.94
080121A	n	y	y	0	0.08	0.33	2.75
080123A	n	y	n	0	0.41	0.26	3.55

GRB	r	o	x	n	θ_0	$\theta_{\mathrm{obs}}/\theta_0$	p
080702A	y	y	y	1	0.18	0.72	2.15
080905A	n	y	y	3	0.42	0.50	2.14
080919A	n	y	y	2	0.29	0.18	2.43
081023A	n	n	y	2	0.42	0.19	2.34
081024A	y	y	y	1	0.30	0.85	3.84
081024B	y	y	n	0	0.23	0.96	3.76
081226A	y	y	y	5	0.44	0.36	2.03
081226B	y	y	y	0	0.27	0.75	3.65
090417A	y	n	n	0	0.45	0.92	2.22
090515A	y	y	y	3	0.47	0.33	3.68
090607A	n	y	y	1	0.11	0.93	2.40
090621B	y	y	y	2	0.42	0.01	3.34
090715A	y	n	n	0	0.32	0.42	3.37
090916A	n	y	y	0	0.13	0.27	3.86
091109B	n	y	y	6	0.40	0.71	2.01
091117A	y	y	n	0	0.30	0.30	3.65
100117A	n	y	y	2	0.39	0.57	2.50
100206A	n	y	y	0	0.46	0.03	2.41
100213A	n	n	y	0	0.26	0.28	2.85
100625A	y	y	y	1	0.16	1.00	2.75
100628A	y	y	y	0	0.42	0.72	2.82
100702A	n	y	y	0	0.30	0.33	2.98
101219A	n	y	y	2	0.05	0.95	3.81
101224A	y	n	y	1	0.37	0.38	2.92
110112B	y	y	y	0	0.23	0.96	4.00
110420B	y	y	n	0	0.38	0.72	2.63
111117A	y	y	y	5	0.10	0.70	2.12
111222A	n	n	y	1	0.45	0.92	2.47
120229A	y	y	n	0	0.26	0.66	3.05
120305A	y	y	y	1	0.09	0.29	2.25
120521A	y	y	y	0	0.11	0.88	3.45
120630A	n	n	y	1	0.22	0.94	3.09
120817B	n	y	y	0	0.17	0.32	2.50
121226A	y	y	y	6	0.42	0.14	2.05
130313A	y	y	y	0	0.38	0.27	3.61
130515A	n	y	y	0	0.20	0.38	3.91
130626A	n	n	y	0	0.29	0.47	3.75
130716A	y	y	y	1	0.11	0.63	2.84

GRB	r	o	x	n	θ_0	$\theta_{\mathrm{obs}}/\theta_0$	p
130822A	y	y	y	0	0.29	0.43	2.40
131125A	n	y	n	0	0.05	0.15	3.47
131126A	n	y	n	0	0.17	0.76	3.16
131224A	y	n	y	0	0.48	0.90	2.84
140320A	n	y	y	1	0.07	0.41	3.46
140402A	n	y	y	0	0.49	0.73	3.94
140414A	n	y	y	0	0.37	0.70	2.06
140516A	y	y	y	2	0.06	0.77	2.02
140606A	n	y	y	0	0.07	0.75	3.49
140619B	y	y	y	0	0.23	0.14	2.15
140622A	y	y	y	2	0.34	0.20	3.95
141202A	n	n	y	0	0.27	0.91	3.93
141205A	n	y	y	0	0.33	1.00	2.18
141212A	y	y	y	4	0.34	0.95	2.39
150101A	y	n	y	1	0.46	0.50	3.67
150101B	y	y	y	4	0.25	0.52	2.15
150120A	y	y	y	0	0.38	0.52	2.56
150301A	n	n	y	0	0.17	0.80	3.36
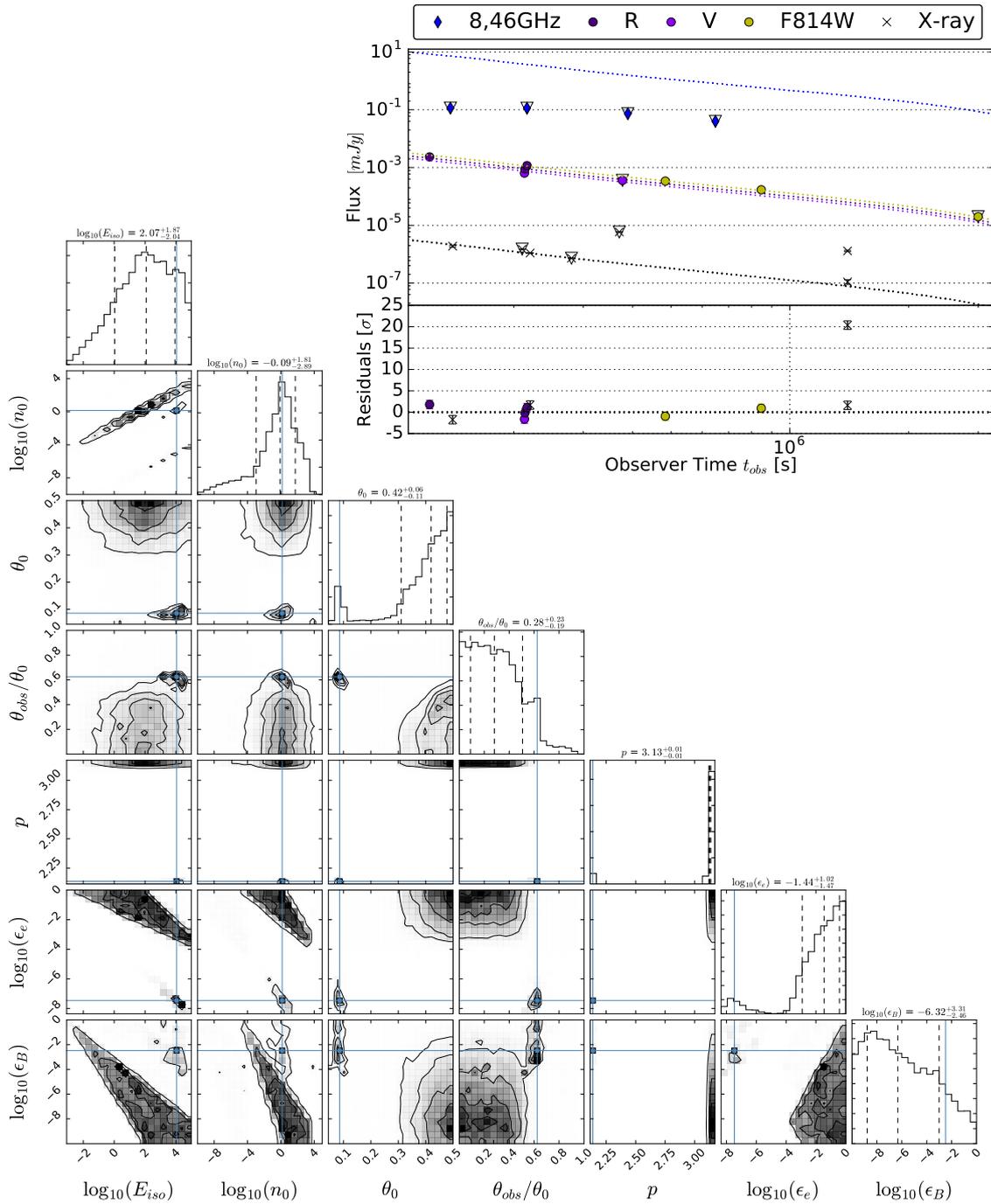
Figure A.1.: Best walker light curve and PDF of GRB 050709A, with a χ^2/DoF = 216. The redshift is $z = 0.161$. I took the optical upper limit into account during the fitting process, but omitted the radio upper limits. The two X-ray data points after 10^6 s come from Chandra. Two fluxes which are one order of magnitude apart in flux space are not explainable by the fire-ball model. To improve the fit I omit the one Chandra data-point with the higher flux (see Fig. A.2).
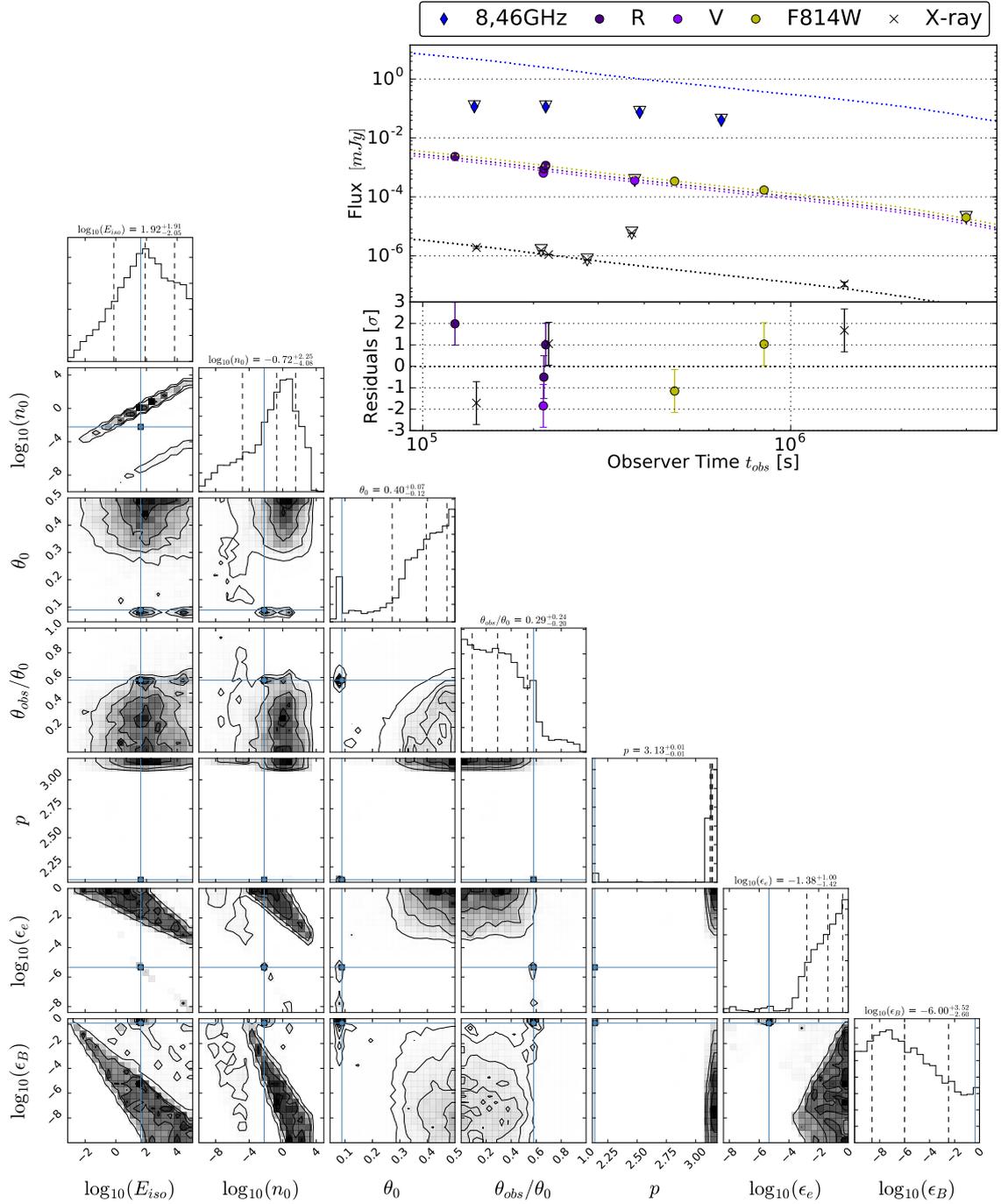
Figure A.2.: Best walker light curve and PDF of GRB 050709A (ignoring the upper Chandra X-ray data point at $\sim 10^6$ s), with a $\chi^2/\text{DoF} = 18.1$. The redshift is $z = 0.161$. I took the optical upper limit into account during the fitting process, but omitted the radio upper limits. θ_0, θ_{obs} and p are constrained. The distribution of θ_0 is at the edge of the prior, which I interpret as a lower limit.
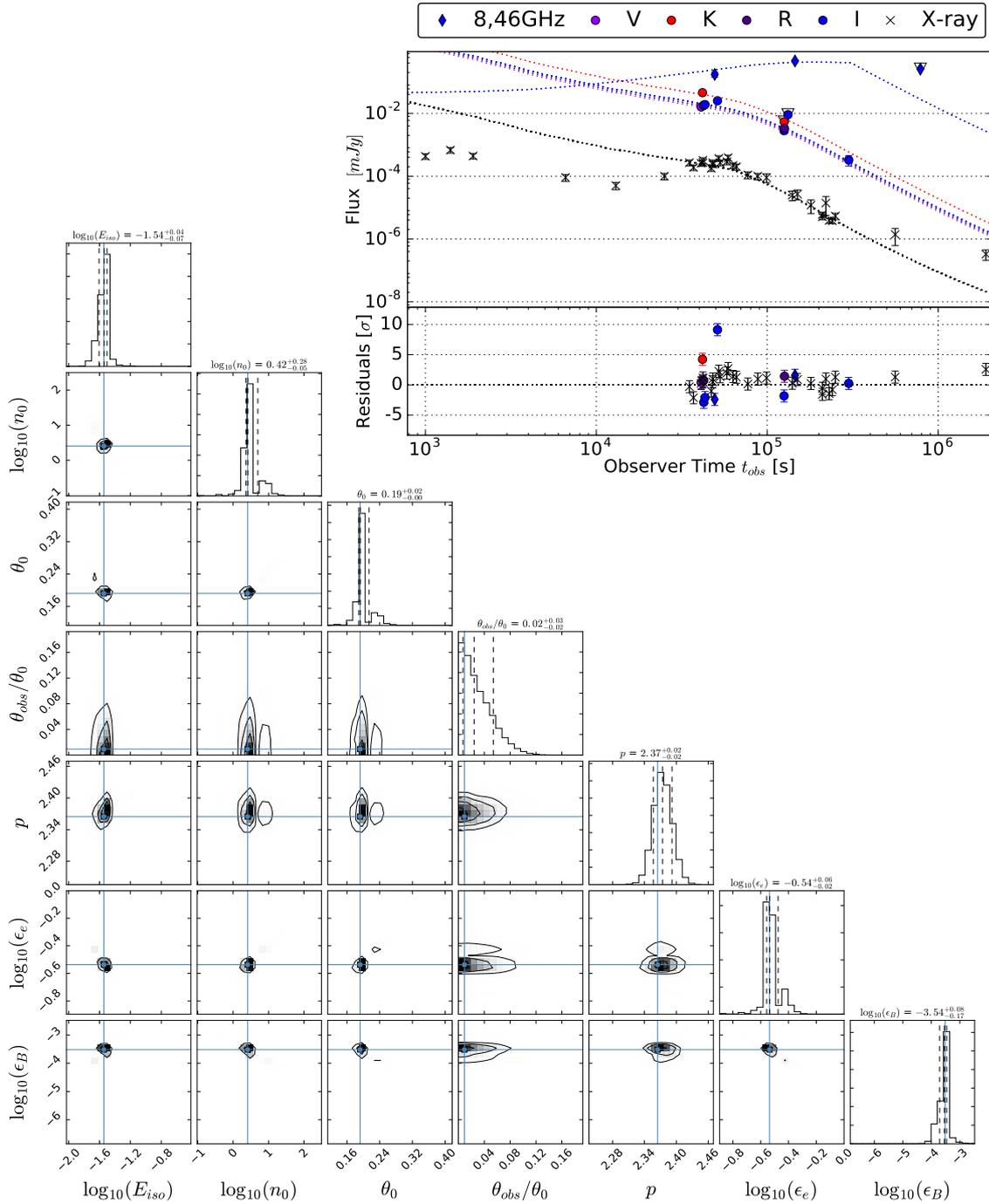
Figure A.3.: Best walker light curve and PDF of GRB 050724A, with a χ^2/DoF = 5.8. The redhsift is $z = 0.257$. I did not include the X-ray data before 3×10^4 s into the fit, since such a re-brightening is not covered by a deceleration model. The first K and I data point diverge from the model by ~ 5 respectively $\sim 10\ \sigma$. This maybe due to achromatic behaviour of the re-brightening. I do consider this a good fit, and θ_0, θ_{obs} and p are constrained.
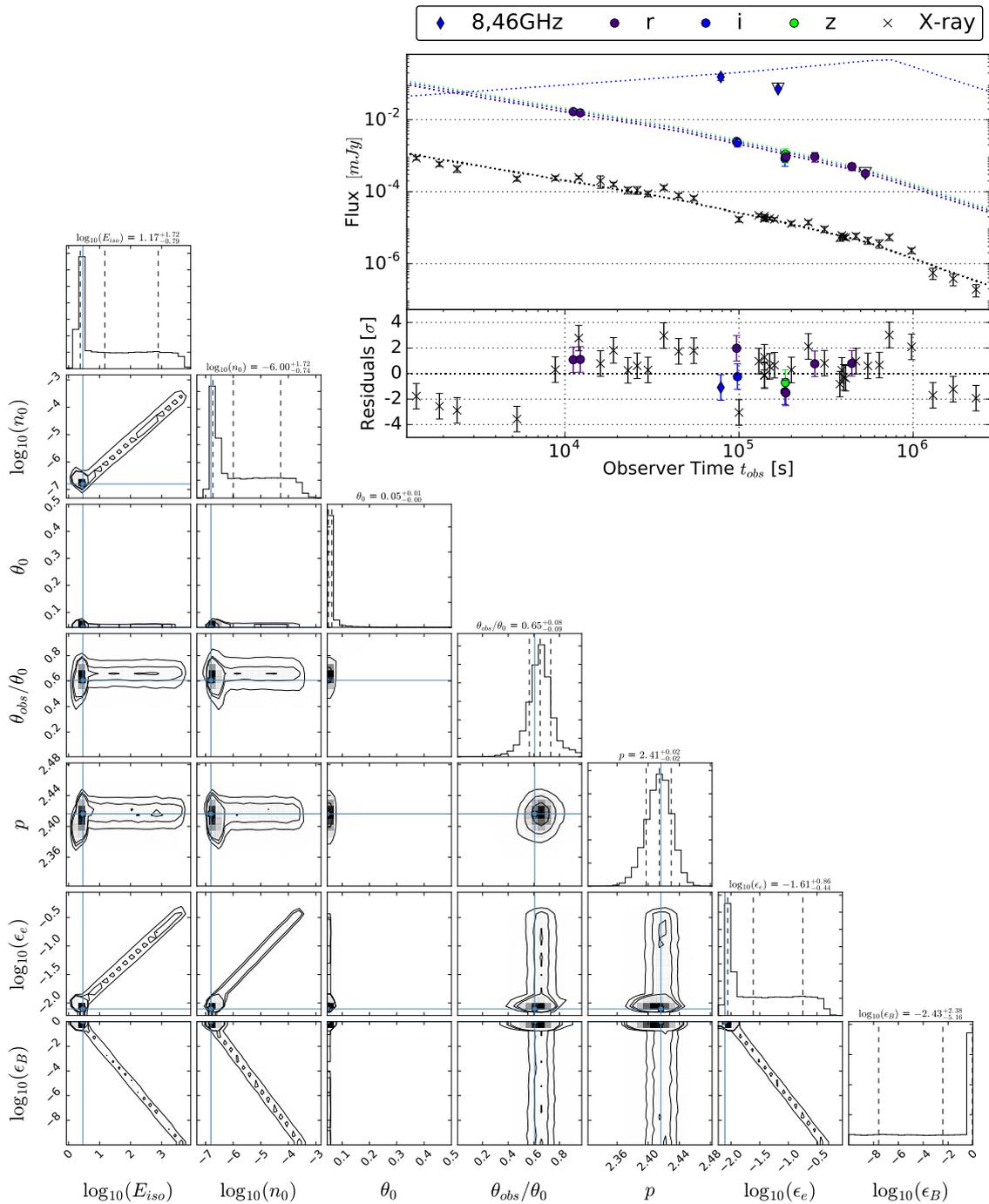
Figure A.4.: Best walker light curve and PDF of GRB 051221A, with a χ^2/DoF = 3.0. The redshift is $z = 0.546$ The radio upper limit was not included in the fitting process, since it could be affected by scintillation. The radio, optical and X-ray detections are well modeled. I do consider this a good fit, and θ_0, θ_obs and p are constrained.
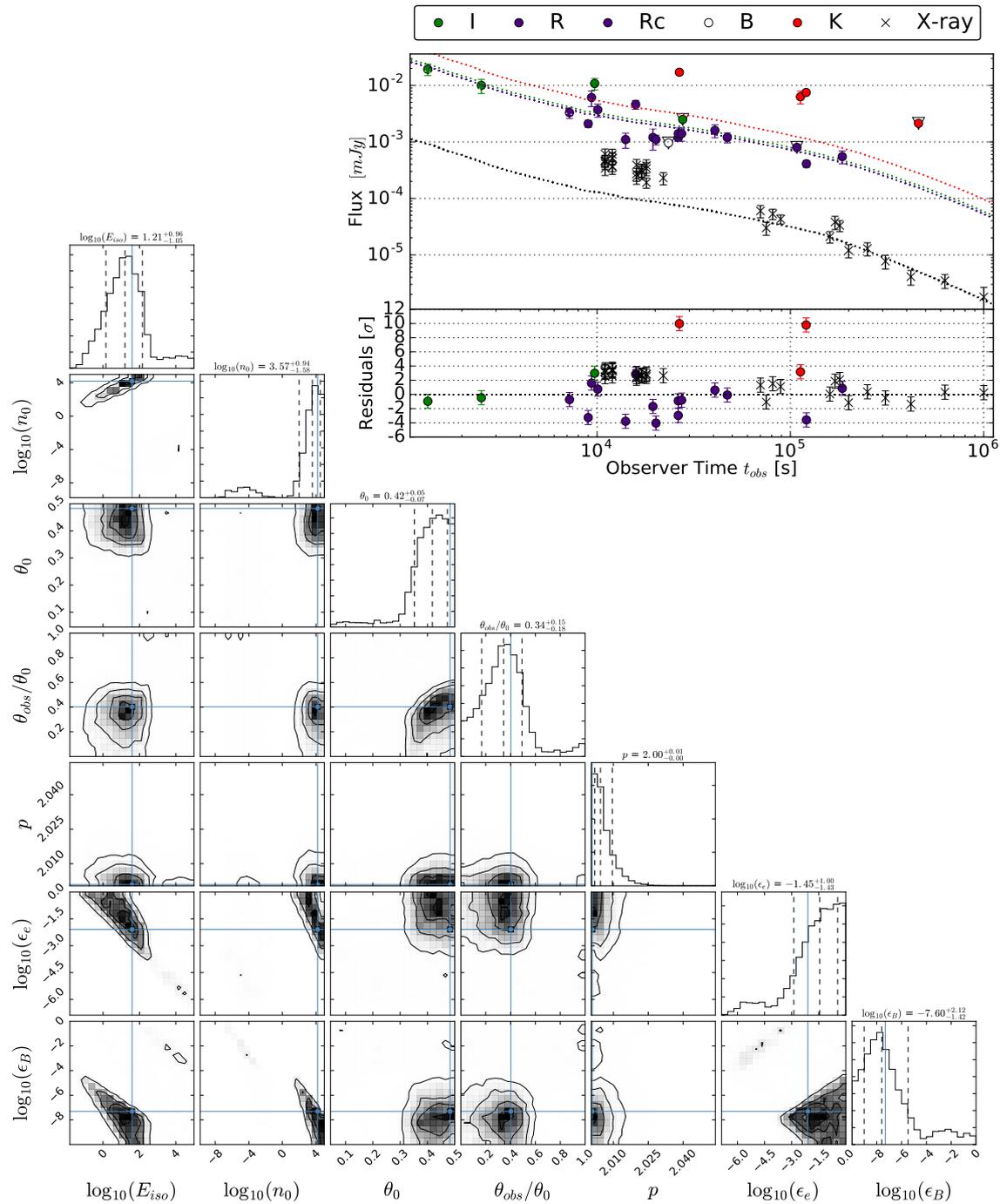
Figure A.5.: Best walker light curve and PDF of GRB 060121A, with a χ^2/DoF = 10.5. The redshift is assumed to be $z = 0.5$. Incorporating a $A_V^{\text{host}} = 1.6\,\text{mag}$ at $z = 0.5$ did not improve the fit. The K band data diverges significantly from the model. That they K band is off may be attributed to a wrong cross calibration of the data, or that the model hits the prior in p, and fails to reproduce the spectral slope. Moreover, the model does not reproduce the shape of the X-ray light curve. I do not consider this a good fit.
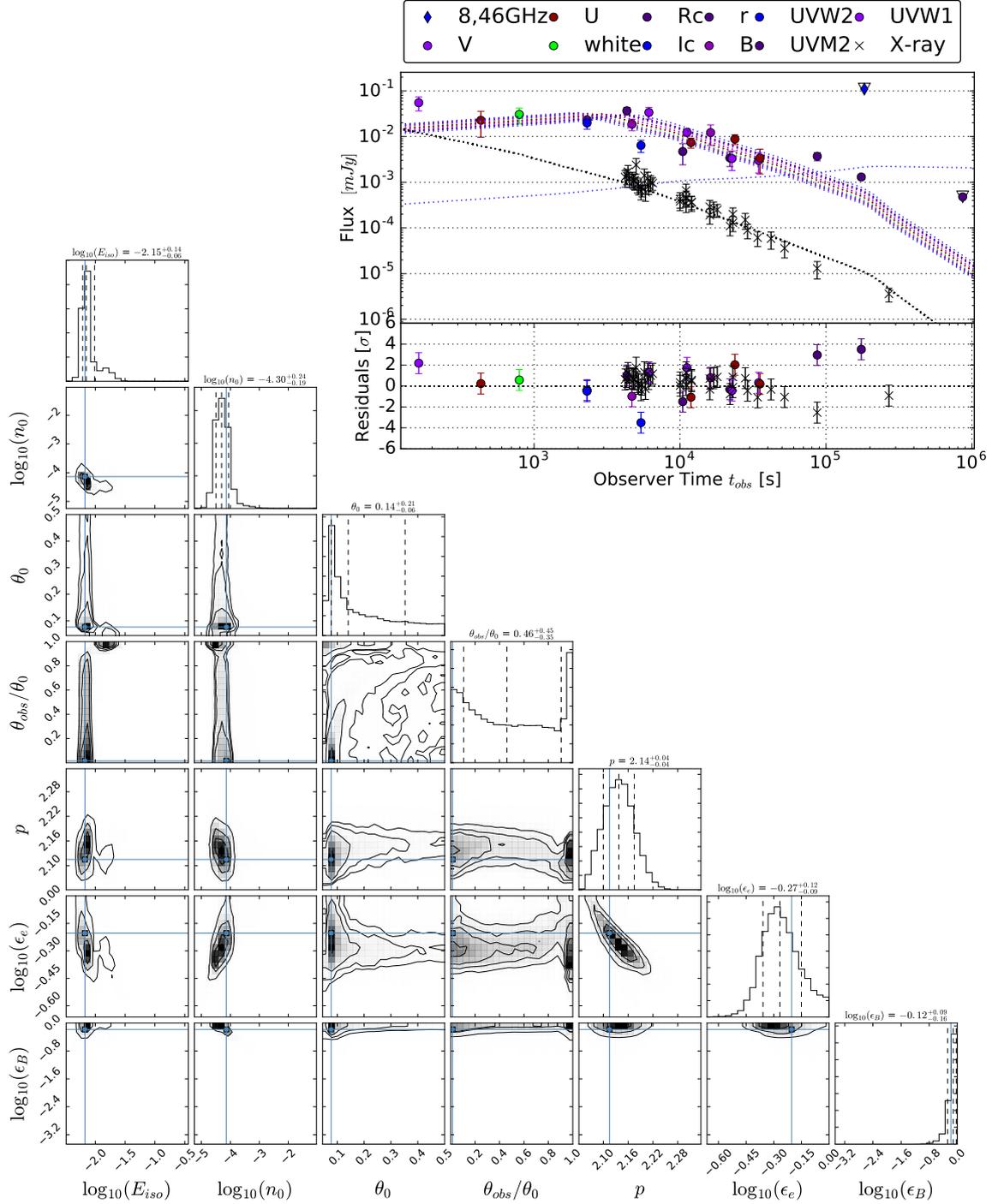
Figure A.6.: Best walker light curve and PDF of GRB 060313A, with a χ^2/DoF = 1.6. The redshift is assumed to be $z = 0.5$. This burst serves as an example to demonstrate the impact of the redshift on the fitting process in Sec. 4.5.1. The light curve for each optical band is plotted, which appears like a shaded are. I do consider this a good fit, and θ_0, θ_{obs} and p are reasonably constrained.
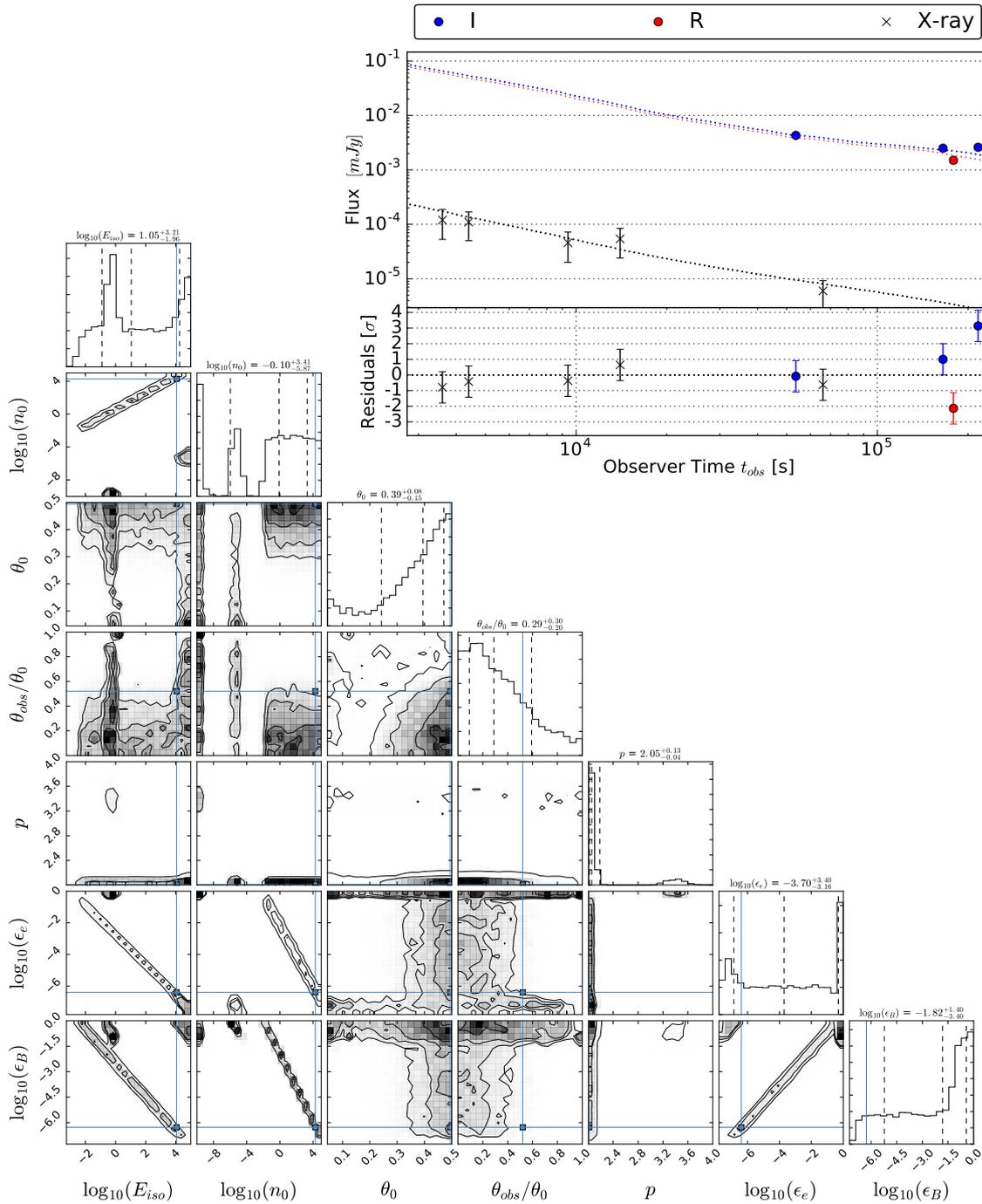
Figure A.7.: Best walker light curve and PDF of GRB 061006A, with a $\chi^2/\mathrm{DoF} = 17.0$. The redshift is $z = 0.438$. The I band data comes from D'Avanzo et al. (2009), where they identify the late optical data as the host via VLT/FORS1 spectroscopy. I re-fit the data, omitting the host detections (see Fig. A.8).
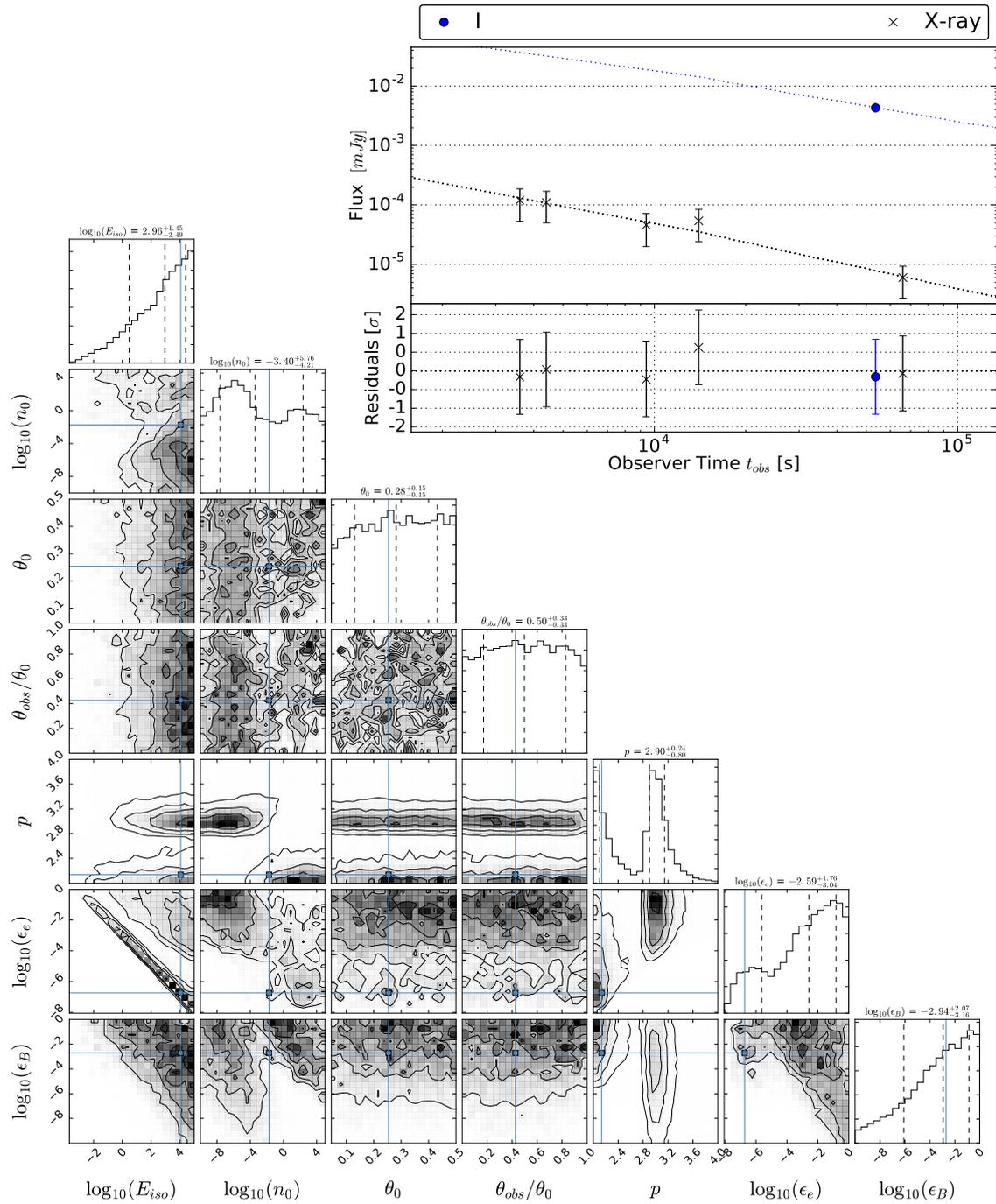
Figure A.8.: Best walker light curve and PDF of GRB 061006A without host, with a $\chi^2/\text{DoF} = $ "-0.2". The redshift is $z = 0.438$. I do consider this a good fit, but θ_0, θ_{obs} are not constrained.
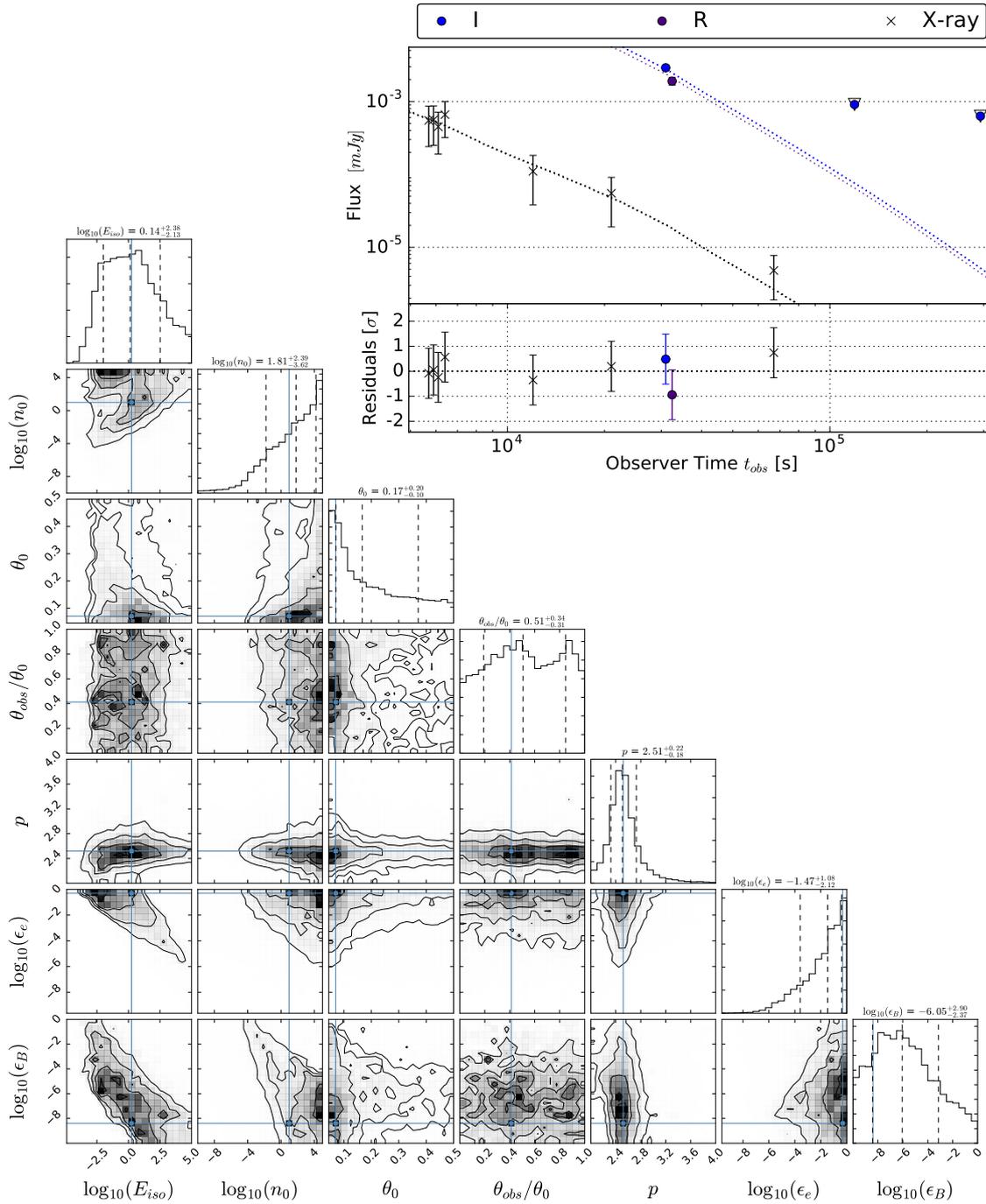
Figure A.9.: Best walker light curve and PDF of GRB 061201A, with a χ^2/DoF = 2.2. The redshift is $z = 0.111$. I do consider this a good fit, and θ_0, θ_{obs} and p are reasonably constrained.
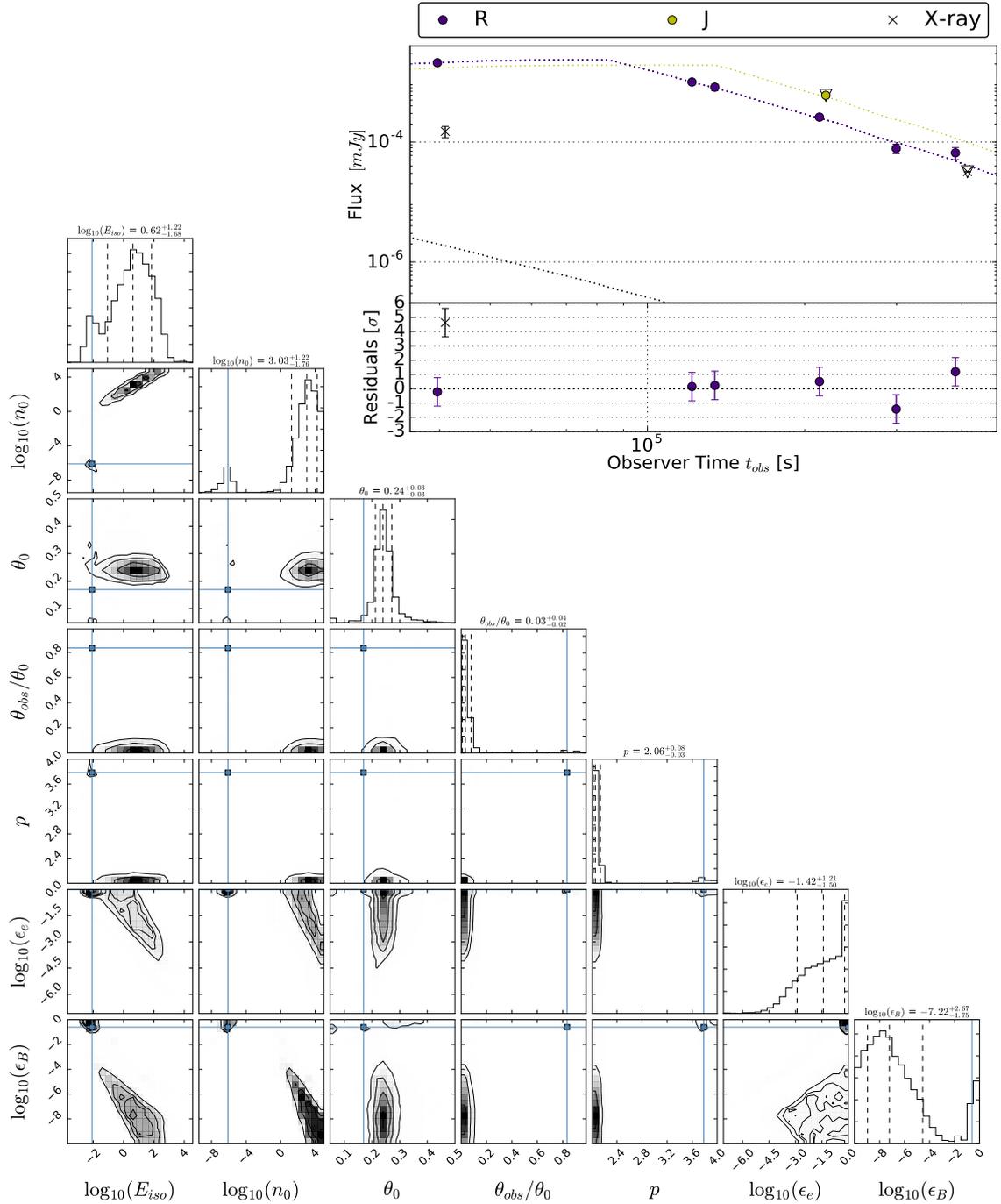
Figure A.10.: Best walker light curve and PDF of GRB 070707A, with a $\chi^2/\text{DoF} = $ "-25.2". The redshift is assumed to be $z = 0.5$. The J band upper limit was ignored by the fitting process, but correctly predicted by the model. The host contribution in the last R band data point (Piranomonte et al. 2008) does not affect the fit significantly. The X-ray data, however, is not well fitted. There is a multi-modality especially visible in the p direction of the parameter space. From the XRT spectrum I find a photon index $\Gamma = 2.8$ (Evans et al. 2009) leading to a $p = 3.6$ (under the assumption $\nu_c < \nu_{\text{X-ray}}$, the assumption $\nu_c < \nu_{\text{X-ray}}$ would lead to a very high $p = 4.6$), which is consistent with the "island of maximum likelyhood" in the corner plot, but not with the bulge of the PDF. The "island of maximal likelyhood" also does not lay on the expected degeneracy in e.g. the E_{iso} / n_0 plane. I do not consider this a good fit.
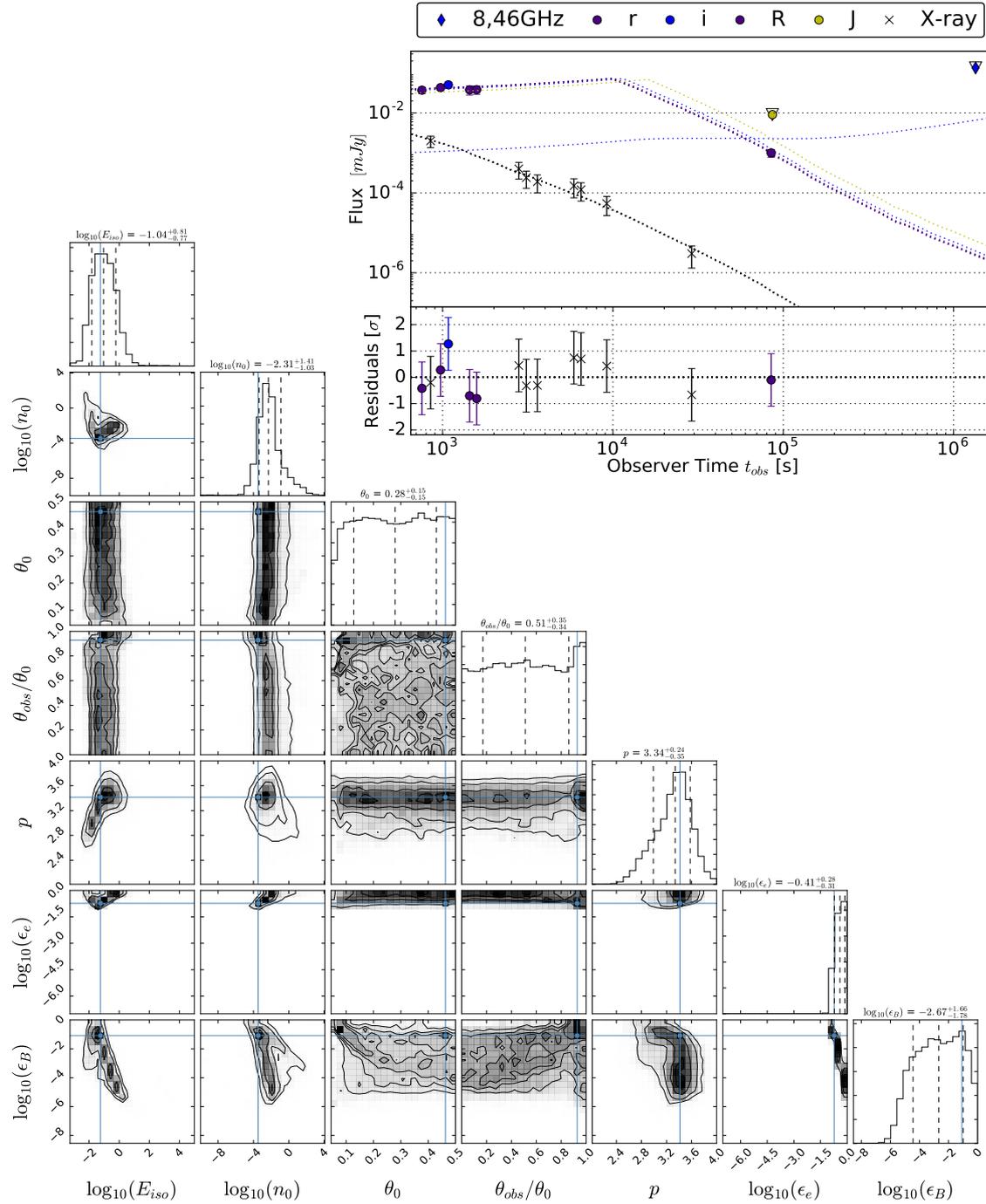
Figure A.11.: Best walker light curve and PDF of GRB 070714B, with a χ^2/DoF = 0.9. The redshift is $z = 0.923$. I note that I do not incorporate host extinction as suggested by Fong et al. (2015). Incorporating an $A_V^{\mathrm{host}} = 0.5\,\mathrm{mag}$ decreases the χ^2/DoF =0.8 (I do that in Fig. A.13). The value for p is suspiciously high. The XRT spectrum has a photon index $\Gamma = 2.0$ (Evans et al. 2009) and would imply a $p = 2.0$ (under the assumption that $\nu_c < \nu_{\mathrm{X-ray}}$). I do consider this a good fit. However, θ_0 and θ_{obs} is not constrained. Fixing $p = 2.0$ increased the $\chi^2/\mathrm{DoF} = 4.1$ (see Fig. A.12).
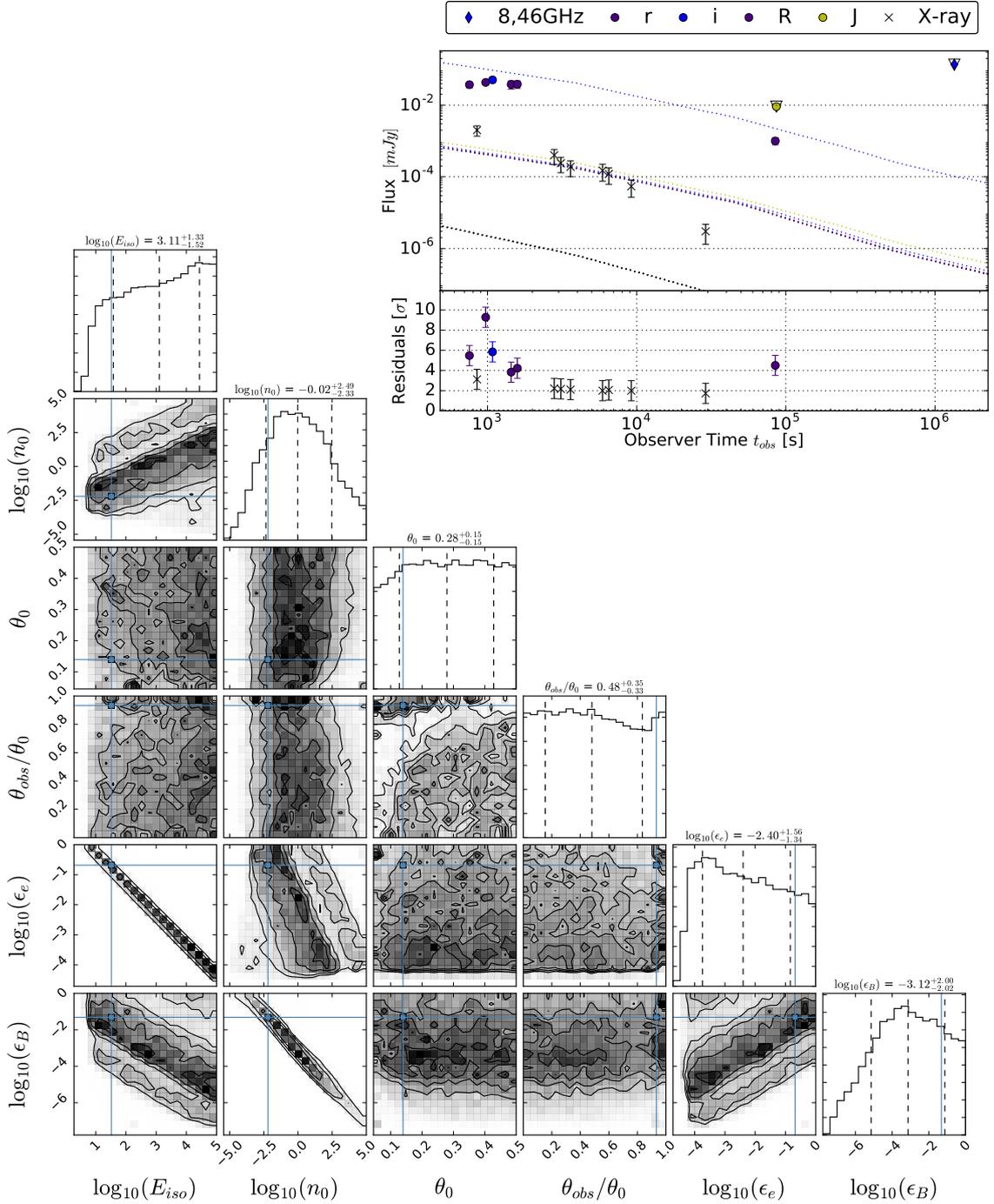
Figure A.12.: Best walker light curve and PDF of GRB 070714B, with a fixed $p = 2.0$ and a $\chi^2/\text{DoF} = 4.1$. The redshift is $z = 0.923$. I note that I do not incorporate host extinction as suggested by Fong et al. (2015). The light curve is not well reproduced. I do not consider this a good fit.
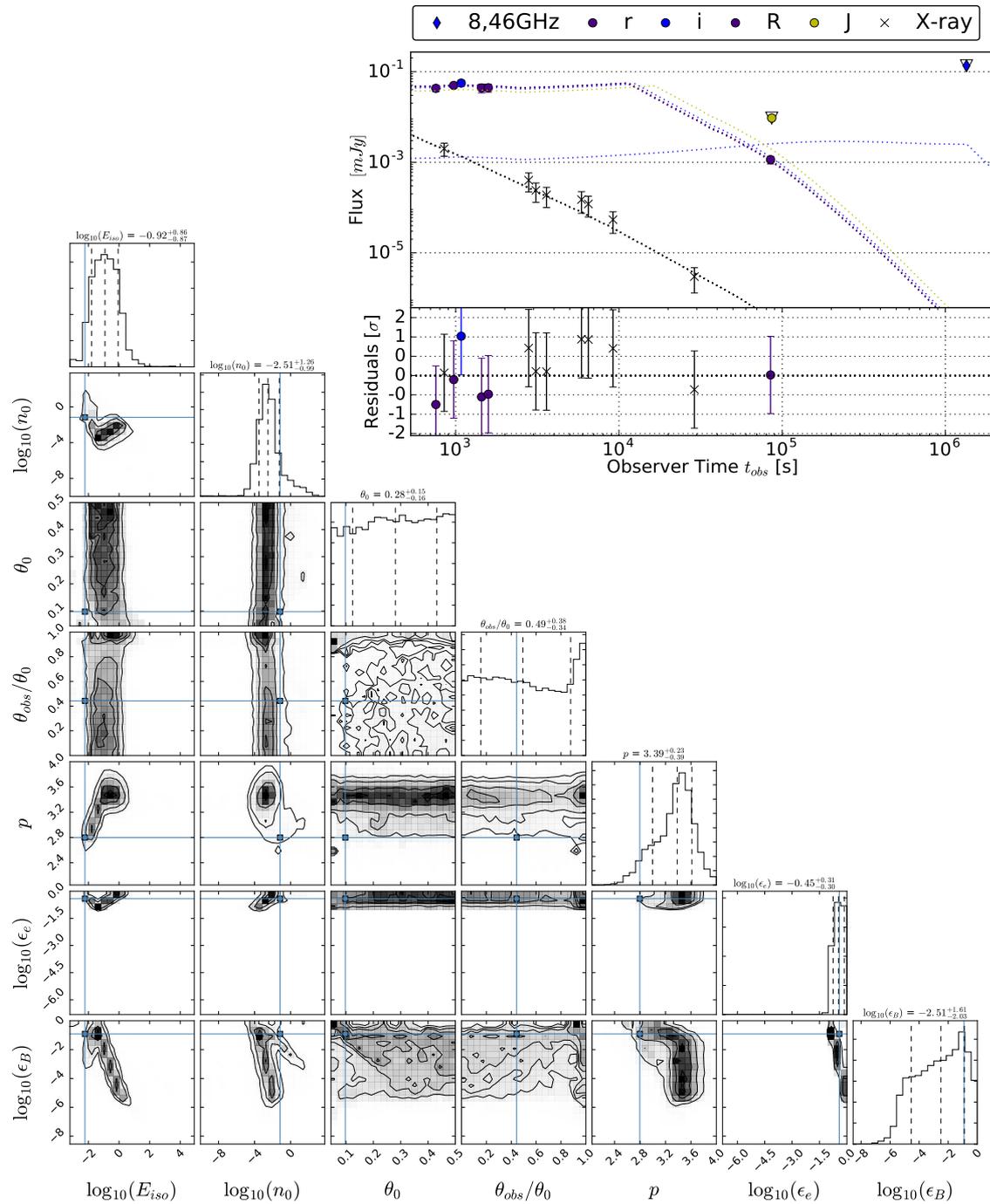
Figure A.13.: Best walker light curve and PDF of GRB 070714B, with a χ^2/DoF = 0.8. I incorporated an $A_V^{\mathrm{host}} = 0.5\,\mathrm{mag}$ at redshift is $z = 0.923$. I do consider this a good fit. However, θ_0 and θ_{obs} is not constrained. The fitting results do not differ significantly from the fit without host extinction.
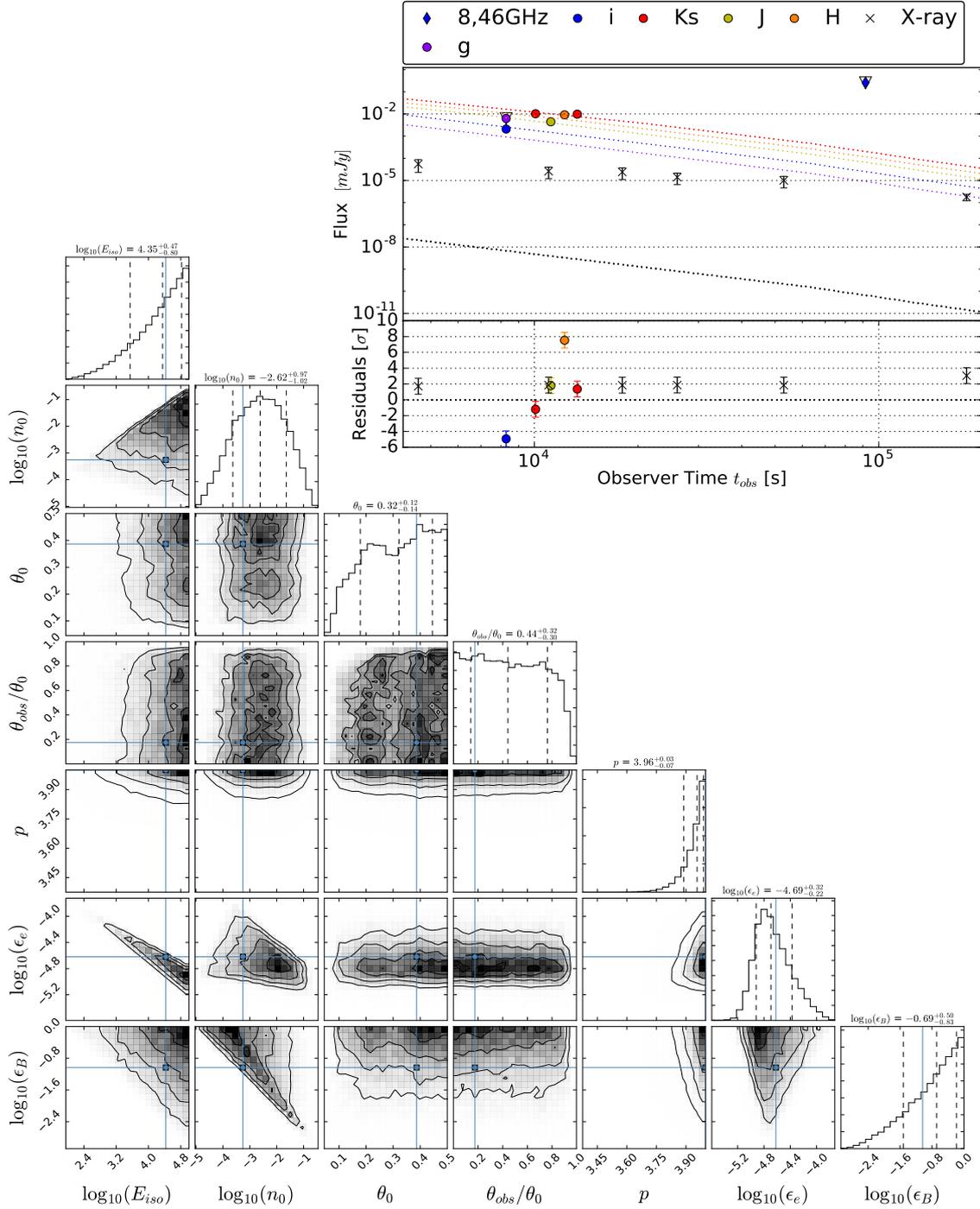
Figure A.14.: Best walker light curve and PDF of GRB 070724A, with a χ^2/DoF = 37.9. I additionally corrected the optical data for an $A_V^{\mathrm{host}} = 2.0$ mag at a redshift z = 0.457. The optical data comes from the GMOS, NIRI, PANIC and LDSS3 instruments (Berger et al. 2009). Berger et al. (2009) point out that the SED is much redder than expected from the standard afterglow model. The model fails to reproduce the spectral slope and p hits the prior. The XRT spectrum has a photon index $\Gamma = 1.4$ (Evans et al. 2009) and implies a $p = 1.8$ (under the assumption that $\nu_m < \nu_{\mathrm{X-ray}} < \nu_c$; The assumption that $\nu_{\mathrm{X-ray}} > \nu_c$ leads to an unphysical $p = 0.8$). Fong et al. (2015) suggested a $p = 2.24$. Fixing $p = 2.24$ increased the χ^2/DoF = 49.7. I do not consider this a good fit.
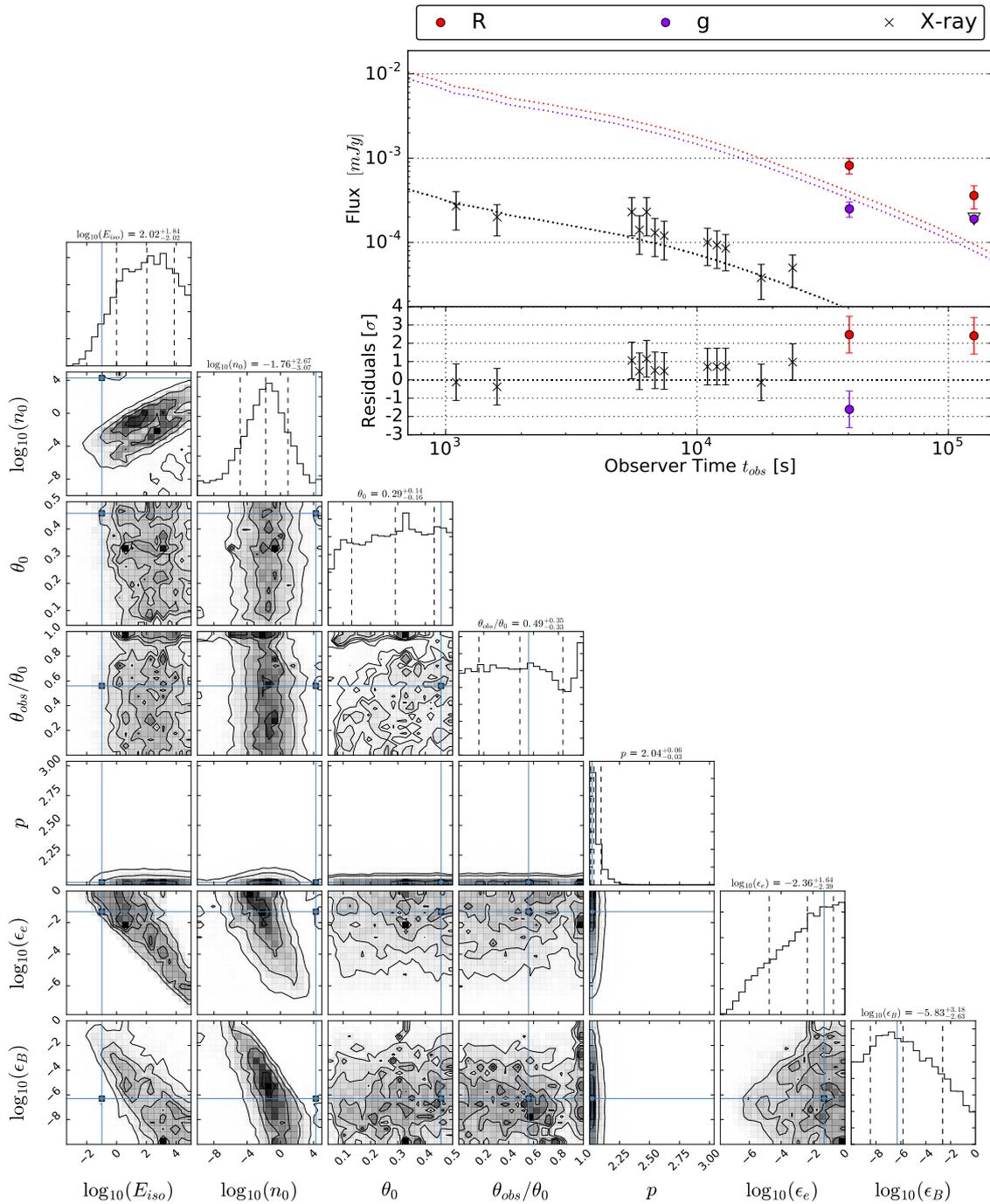
Figure A.15.: Best walker light curve and PDF of GRB 070809A, with a χ^2/DoF = 2.9. The redshift is $z = 0.473$. The g band upper limit is not taken into account. Upper limits from a late (6 month after the trigger) follow up by Perley et al. (2008) are not plotted but consistent with the model. The optical data is not modeled well. This fit is performed without involving host extinction. Kann et al. (2011) found a $A_V^{\mathrm{host}} = 1.45\,\mathrm{mag}$, but incorporating the host extinction did not improve the fit. I do consider this a good fit, but θ_0 and θ_{obs} is not constrained.
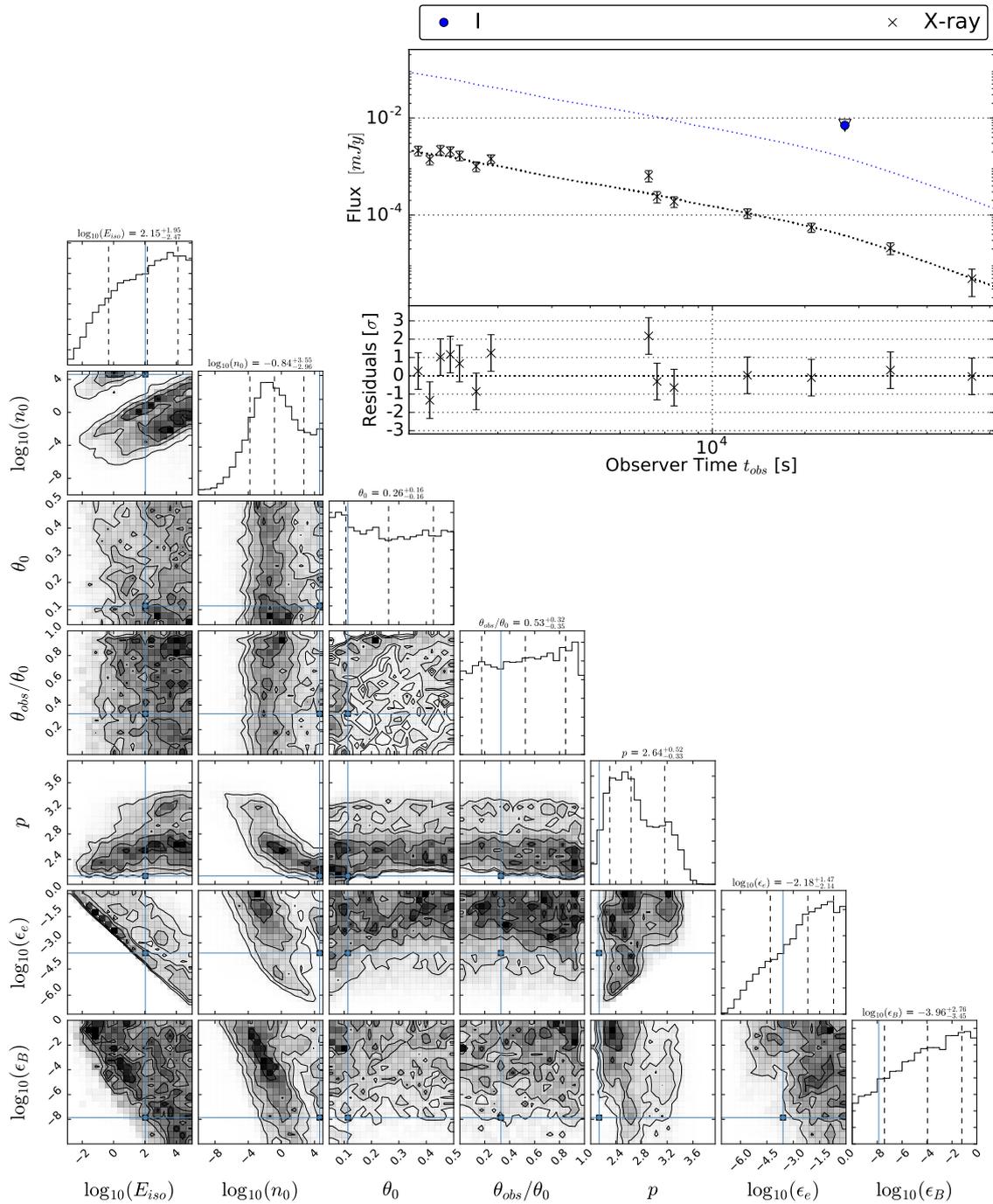
Figure A.16.: Best walker light curve and PDF of GRB 080426A, with a χ^2/DoF = 2.1. The redshift is assumed to be $z = 0.5$. The light curve is well described, but the parameters are barely constrained. I do consider this a good fit, but θ_0 and θ_{obs} are not well constrained.
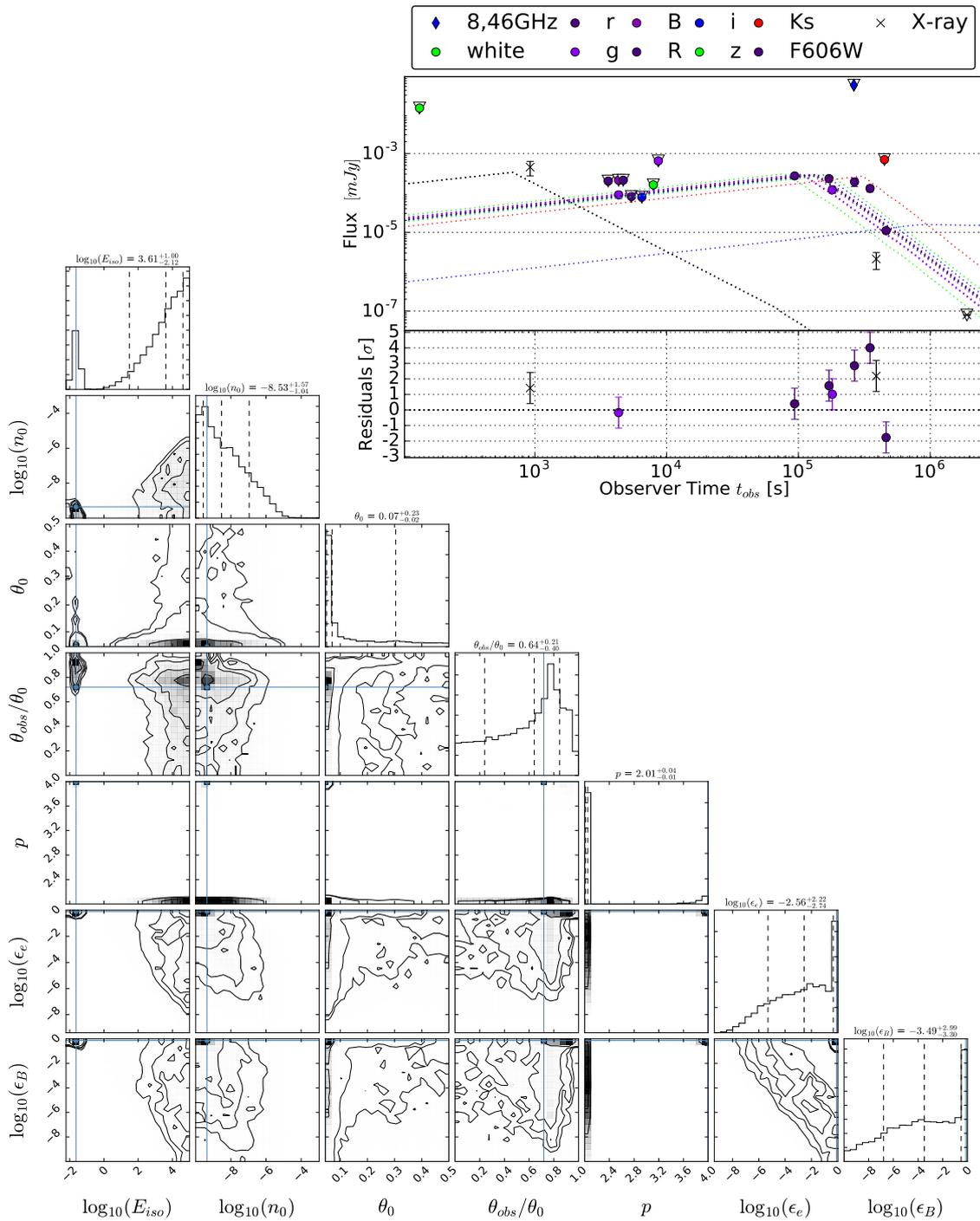
Figure A.17.: Best walker light curve and PDF of GRB 080503A, with a $\chi^2/\mathrm{DoF} = 37.7$. The redshift is assumed to be $z = 0.5$. There is an "island of high probability", with a suspiciously high p value, but the bulge of the PDF is well constrained towards a $p = 2.01^{+0.04}_{-0.01}$. The XRT spectrum has a photon index $\Gamma = 2.4$ (Evans et al. 2009). The assumption that $\nu_c < \nu_{\mathrm{X-ray}}$ implies a $p = 2.8$. Fixing $p = 2.8$ improves the $\chi^2/\mathrm{DoF} = 32.0$ (PDF see Fig. A.18). The assumption that $\nu_c > \nu_{\mathrm{X-ray}}$ implies a $p = 3.8$. Fixing $p = 3.8$ improves the $\chi^2/\mathrm{DoF} = 17.6$ (PDF see Fig. A.19). (Perley et al. 2009) claim that the late re-brightening in the X-ray (Chandra) and optical is unlikely to be the afterglow, while SCALEFIT explains it to be a late ν_m crossing.
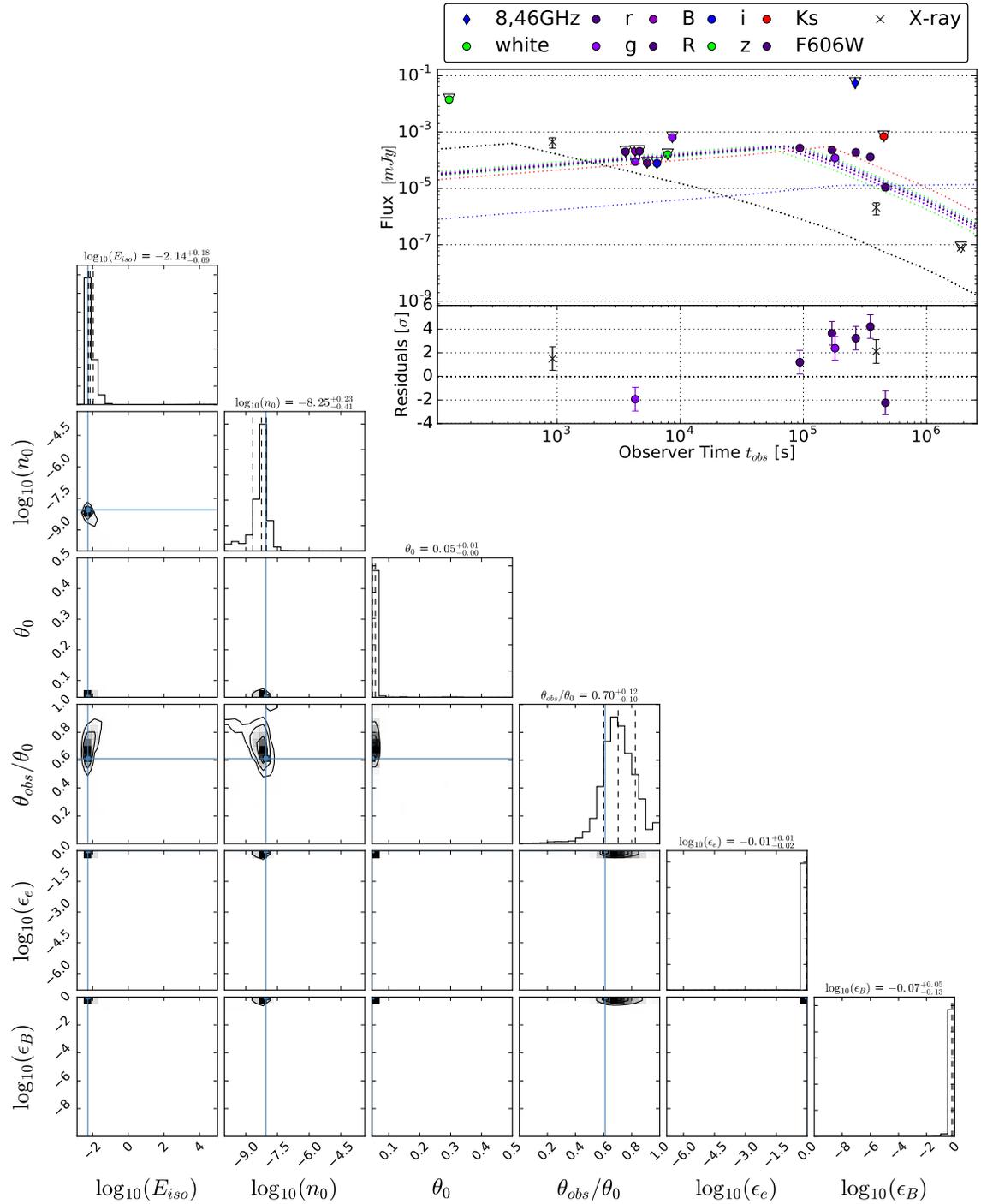
Figure A.18.: PDF of GRB 080503A with a fixed $p = 2.8$ and an improved $\chi^2/\text{DoF} = 32.0$.
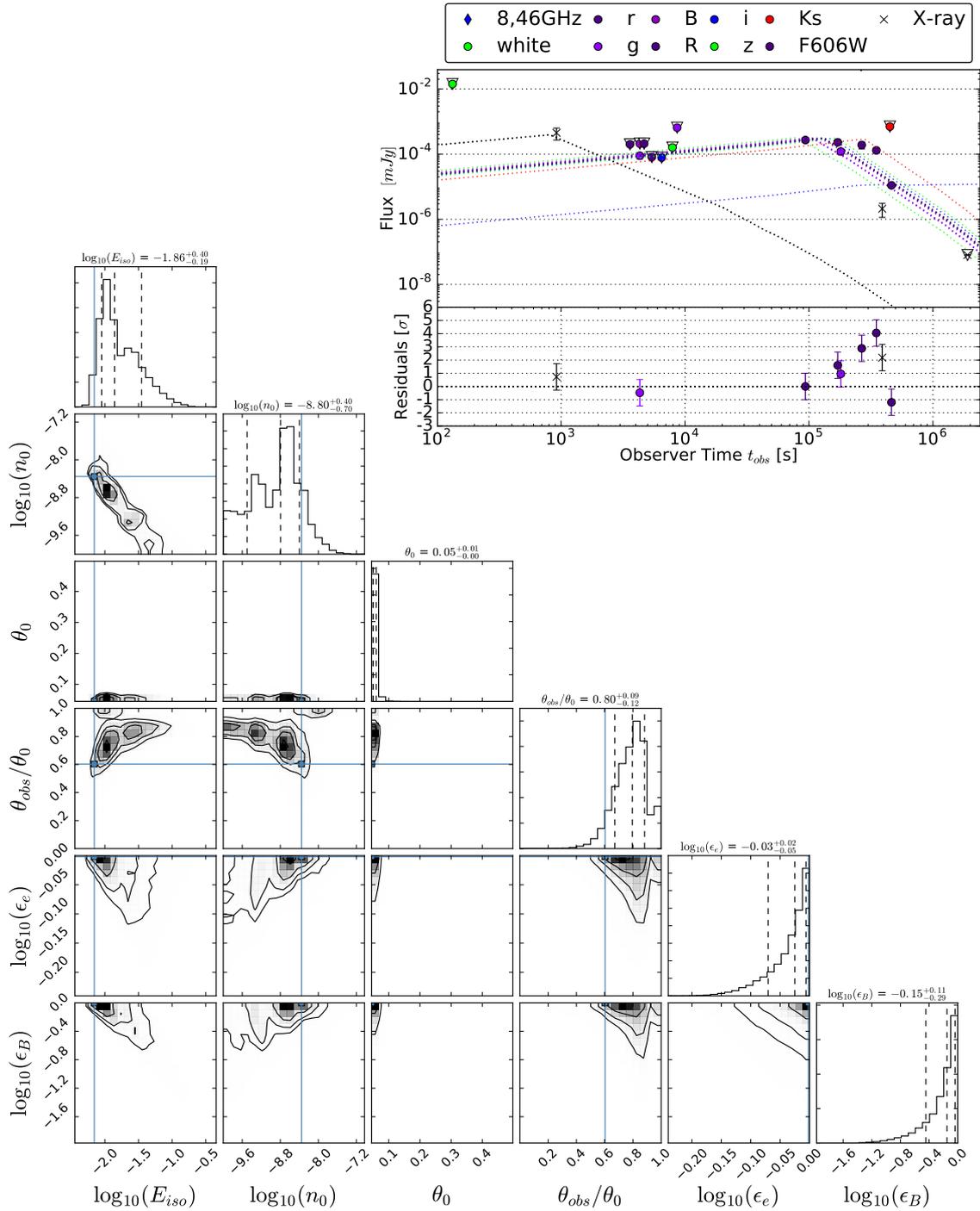
Figure A.19.: PDF of GRB 080503A with a fixed $p = 3.8$ and an improved $\chi^2/\mathrm{DoF} = 17.6$. I do consider this a good fit, and θ_0 and θ_{obs} are well constrained.
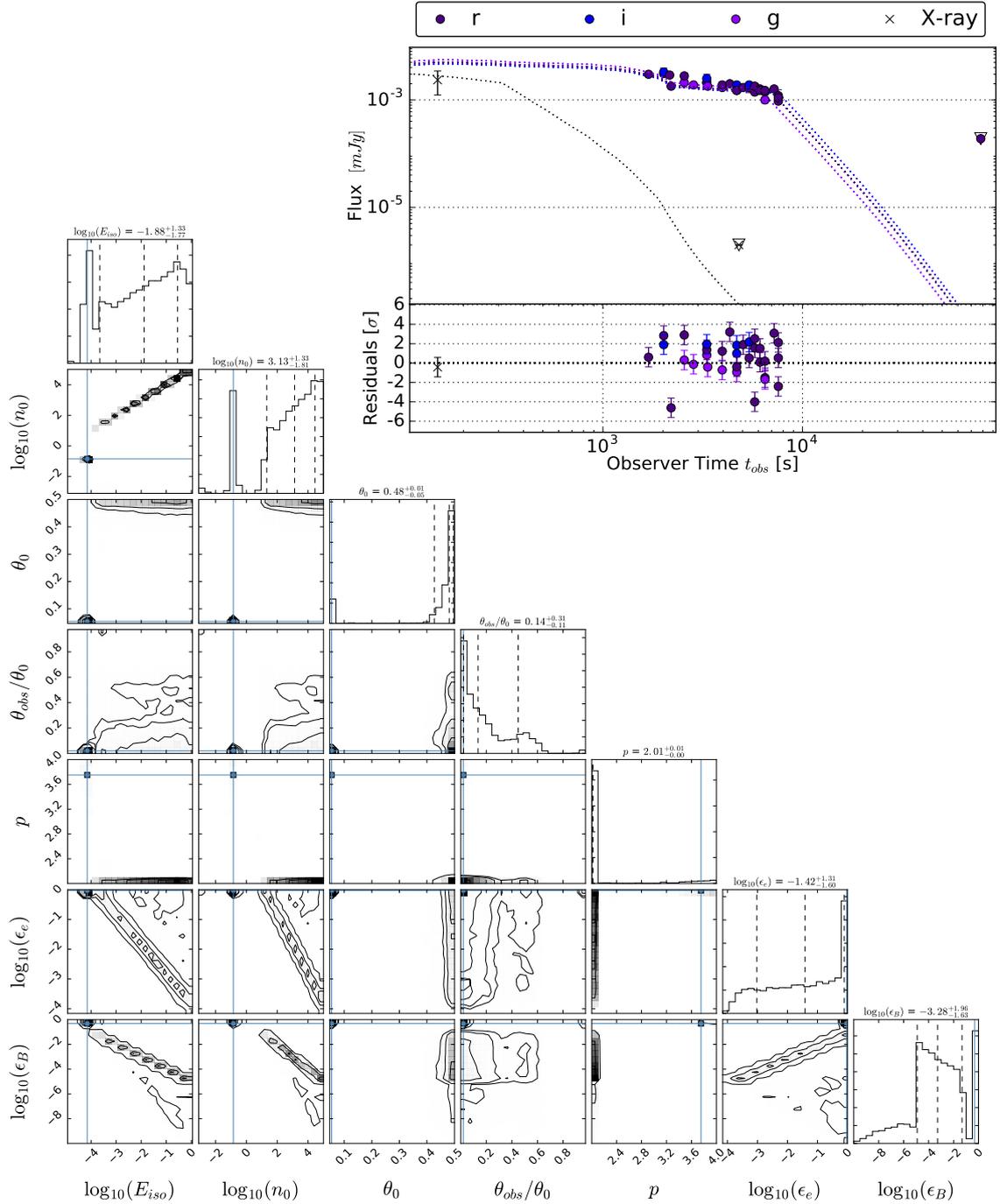
Figure A.20.: Best walker light curve and PDF of GRB 090305A, with a χ^2/DoF = 8.9. The redshift is assumed to be $z = 0.5$. Additionally to the data from Fong et al. (2015) we include an X-ray detection from Beardmore et al. (2009). According to my mode fit the X-ray break at $\sim 300\,\mathrm{s}$ and the optical break at $\sim 7000\,\mathrm{s}$ are ν_m crossings. Energy injection may be an alternative explanation, and will be subject of future studies. The achromatic break $\sim 2000\,\mathrm{s}$ is the transition from fast to slow cooling. There is an "island of high probability", with a suspiciously high p value, and which lays close to the expected degeneracies in e.g. the E_{iso} / n_0 plane. The the PDF is well constrained towards a $p = 2.012^{+0.014}_{-0.005}$. There is no XRT spectrum available to put additional constraints on p. θ_0, θ_{obs} and p are constrained. θ_0 is at the edge of the prior, which I interpret as a lower limit.
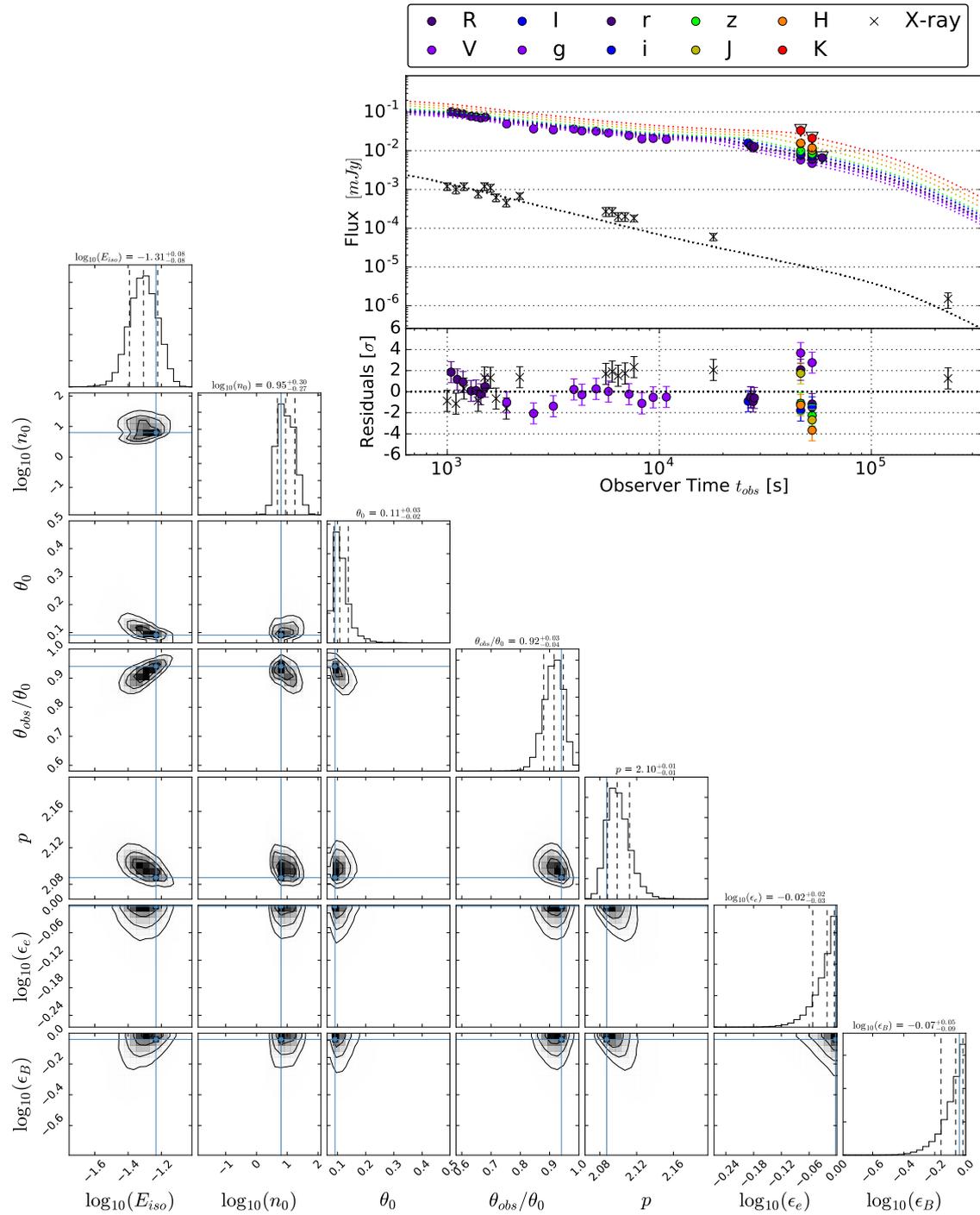
Figure A.21.: Best walker light curve and PDF of GRB 090426A, with a χ^2/DoF = 2.7. The redshift is $z = 2.609$. I do consider this a good fit, and θ_0, θ_{obs} and p are constrained.
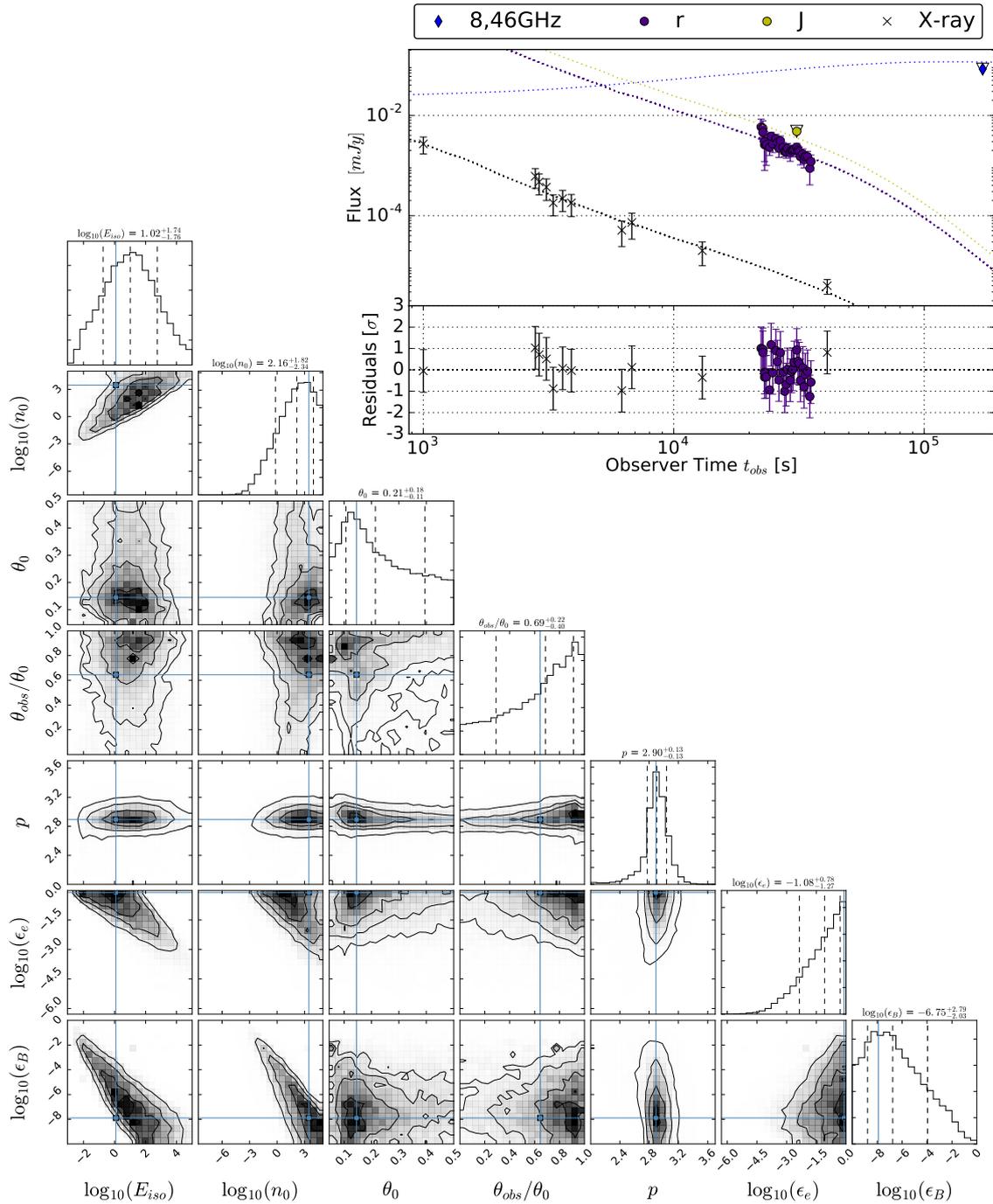
Figure A.22.: Best walker light curve and PDF of GRB 090510A, with a χ^2/DoF = 0.5. The redshift is $z = 0.903$. The upper limits have not been part of the fitting process, but the predicted light curve for the bands are consistent. I do consider this a good fit, and θ_0, θ_{obs} and p are constrained.
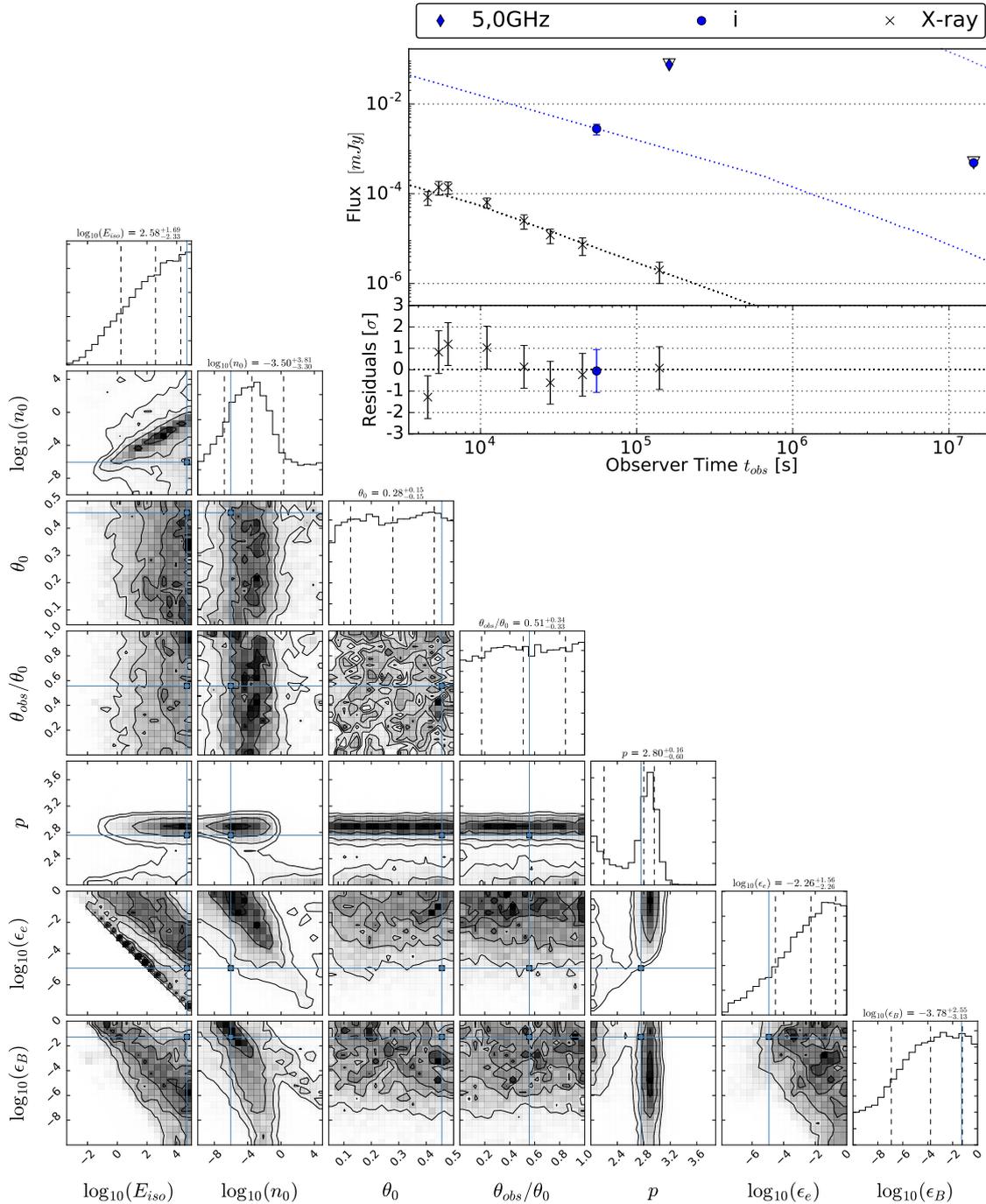
Figure A.23.: Best walker light curve and PDF of GRB 110112A, with a χ^2/DoF = 5.3. The redshift is assumed to be $z = 0.5$. The upper limits have not been part of the fitting process. I do consider this a good fit, but θ_0 and θ_{obs} are not constrained.
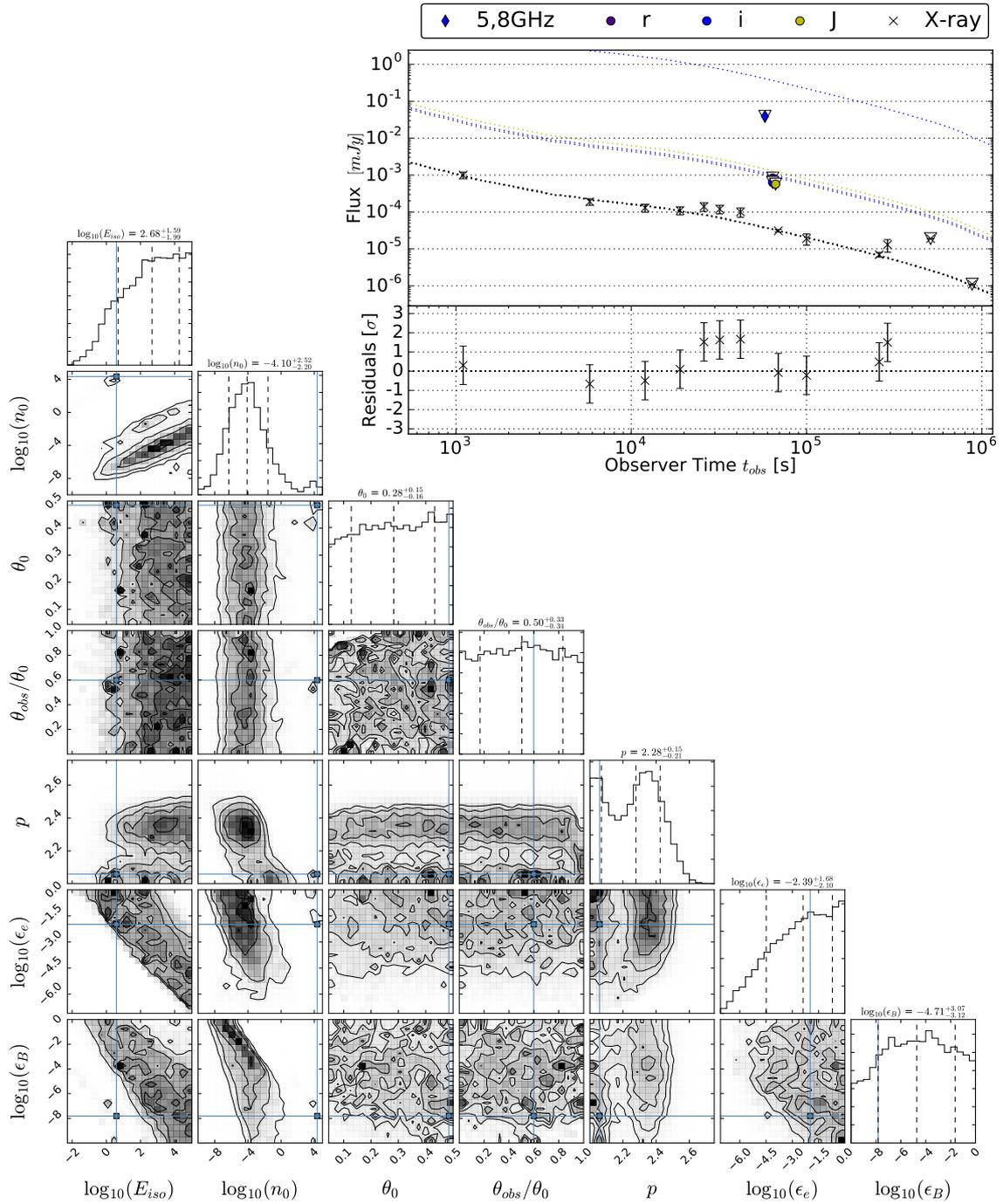
Figure A.24.: Best walker light curve and PDF of GRB 111020A, with a χ^2/DoF = 3.7. The redshift is assumed to be $z = 0.5$. The upper limits have not been part of the fitting process. I note, that I do not include host extinction as suggested by Fong et al. (2015). I do consider this a good fit, however θ_0, θ_{obs} and p are not well constrained.
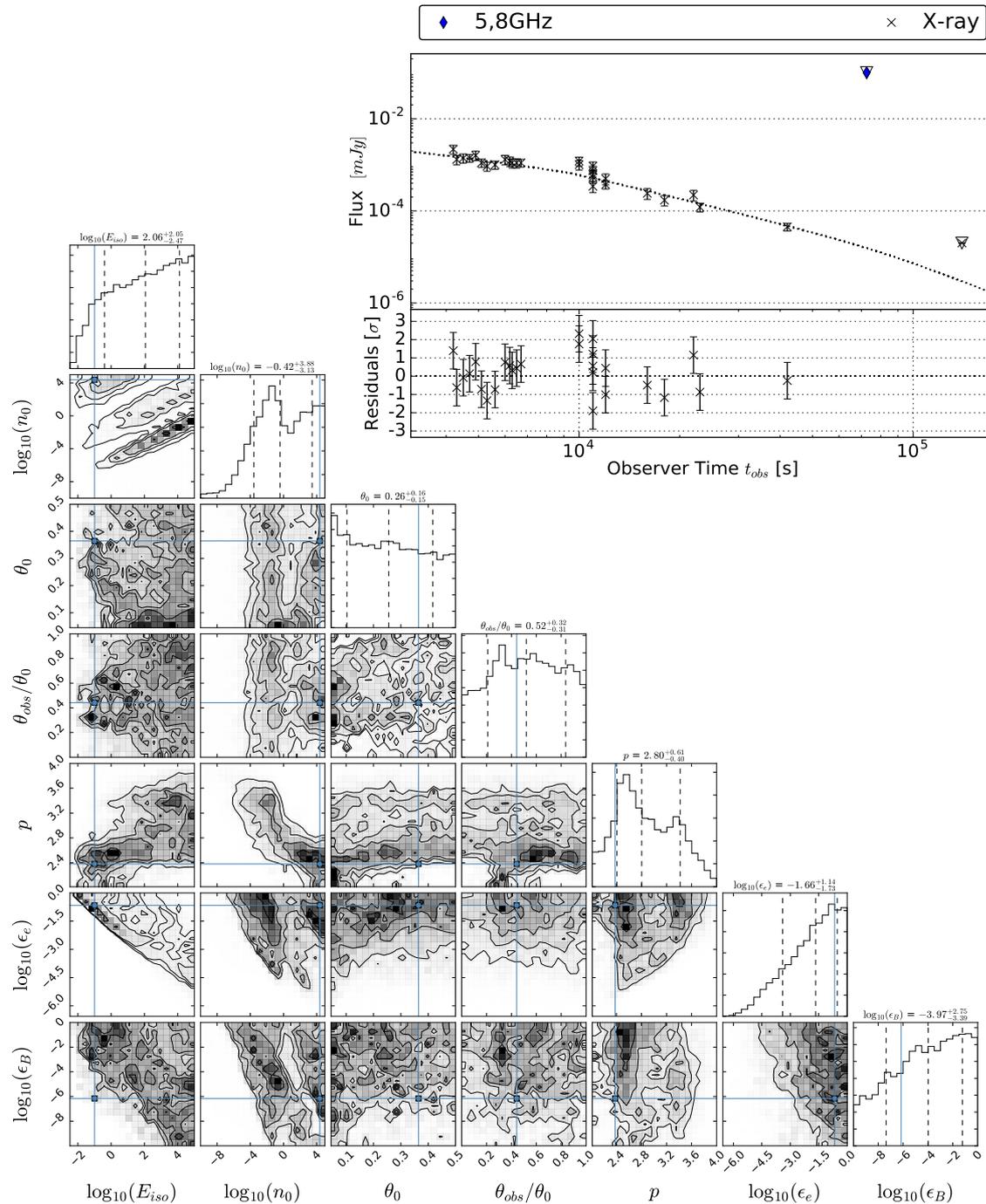
Figure A.25.: Best walker light curve and PDF of GRB 111121A, with a χ^2/DoF = 1.6. The redshift is asumed to be $z = 0.5$. The upper limits have not been part of the fitting process. I consider this a good fit, however θ_0 and θ_{obs} are not constrained.
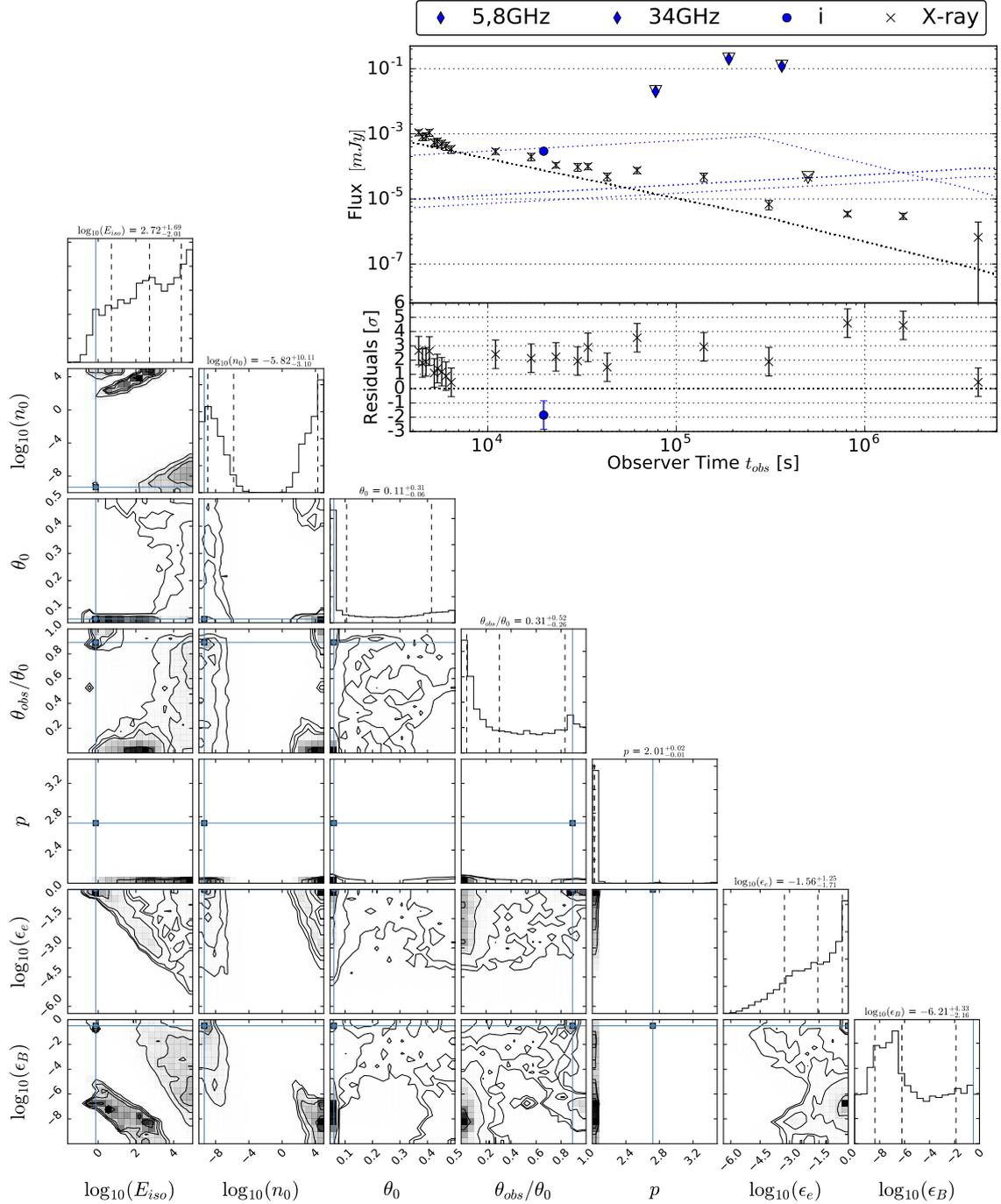
Figure A.26.: Best walker light curve and PDF of GRB 120804A, with a χ^2/DoF = 9.0. The upper limits have not been part of the fitting process. I additionally corrected for a rather high $A_V^{\mathrm{host}} = 2.5\,\mathrm{mag}$ (as suggested by Fong et al. (2015)) at a redshift z=0.81. Not incorporating the host extinction leads to a $\chi^2/\mathrm{DoF} = 24.05$. The first 5 X-ray data points seem not to lay on a power law with the rest, but omitting them does not improve the fit. There is an "island of high probability", with a suspiciously high p value, and which does not lie on the expected degeneracies in e.g. the E_{iso} / n_0 plane. This is probably a fragment of the fitting process. The bulge of the PDF is well constrained towards a $p = 2.01^{+0.02}_{-0.01}$, and is in agreement with the value for p from the XRT spectrum (assuming $\nu_c < \nu_{\mathrm{X-ray}}$). The XRT spectrum (integrated over the whole time range) has a photon index $\Gamma = 2.0$ (Evans et al. 2009) and implies a $p = 2.0$ (under the assumption that $\nu_c < \nu_{\mathrm{X-ray}}$). The model fails to reproduced the shape of the X-ray light curve. I do not consider this a good fit.
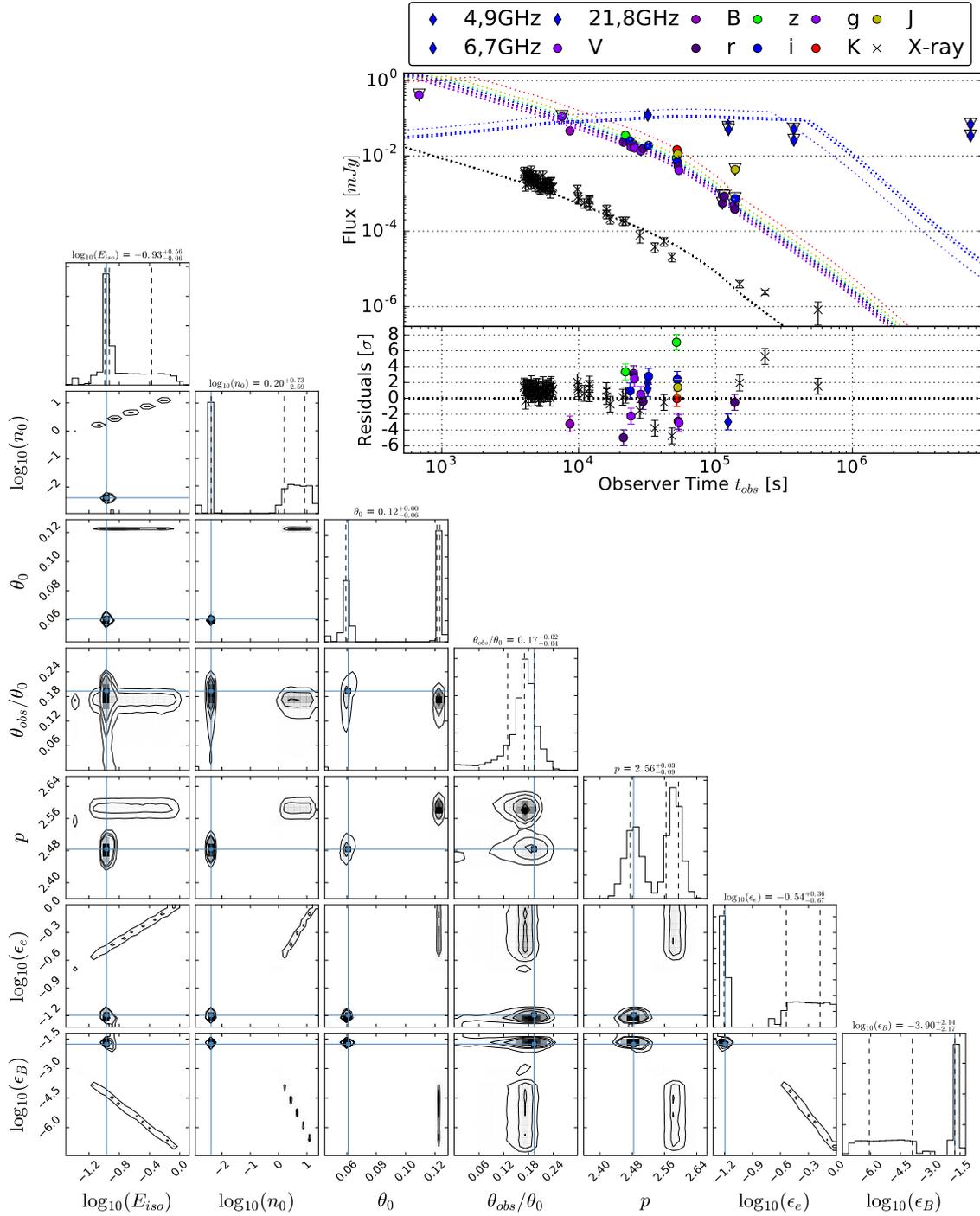
Figure A.27.: Best walker light curve and PDF of GRB 130603B. The upper limits have not been part of the fitting process. I additionally corrected for an $A_V^{\text{host}} = 1.2\,\text{mag}$ at a redshift $z = 0.356$. The PDF shows a multi-modality. I sample the two modes separately in Fig. A.28 and Fig. A.29. Both of the modes have the same χ^2/DoF. Interestingly they also have the same $\theta_{\text{obs}}/\theta_0$.
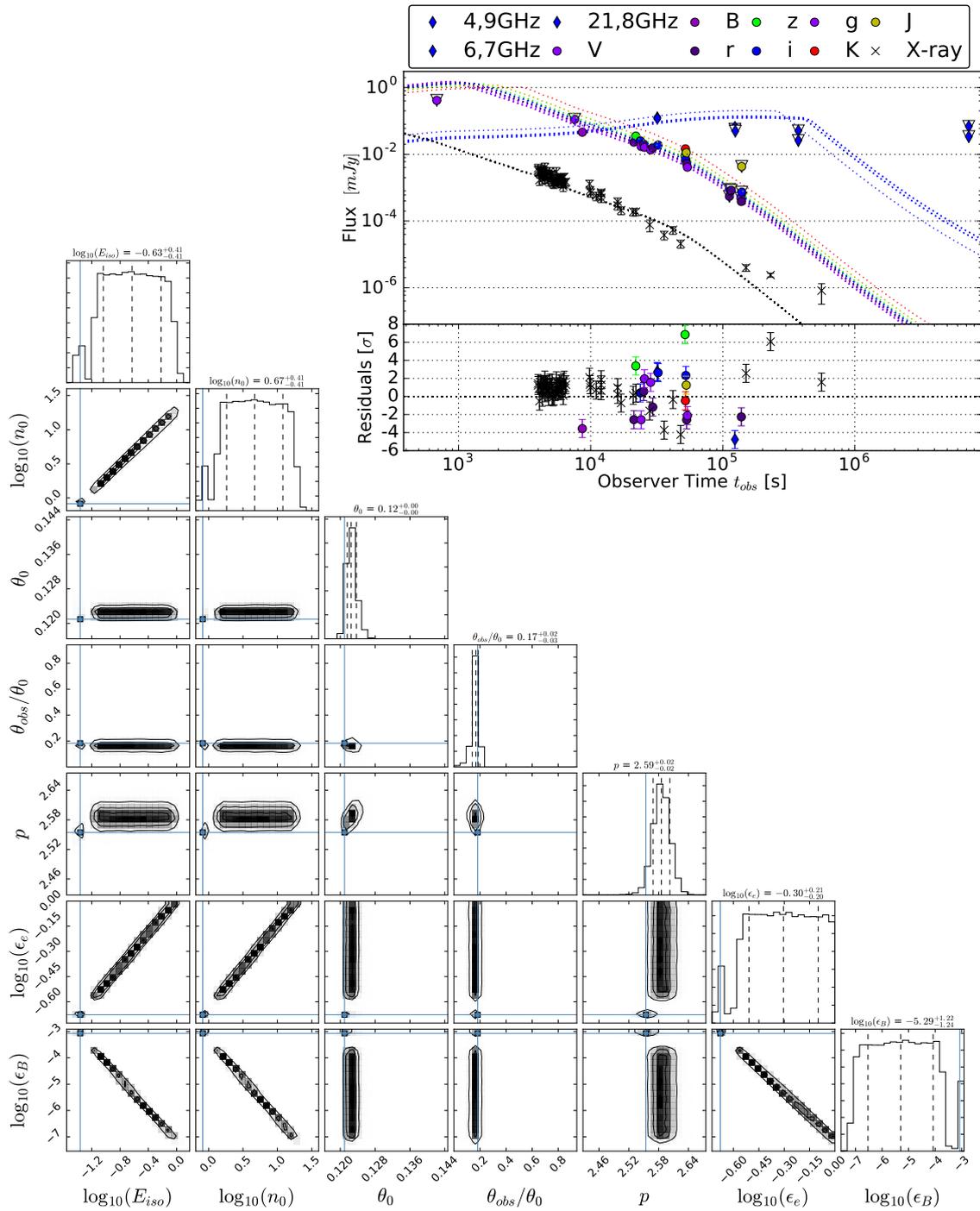
Figure A.28.: Mode I, around $\theta_0 = 0.12$ rad of the PDF of GRB 130603B, with a $\chi^2/\mathrm{DoF} = 4.3$. I additionally corrected for an $A_V^{\mathrm{host}} = 1.2\,\mathrm{mag}$ at a redshift $z = 0.356$. I do consider this a good fit, and θ_0, θ_{obs} and p are constrained.
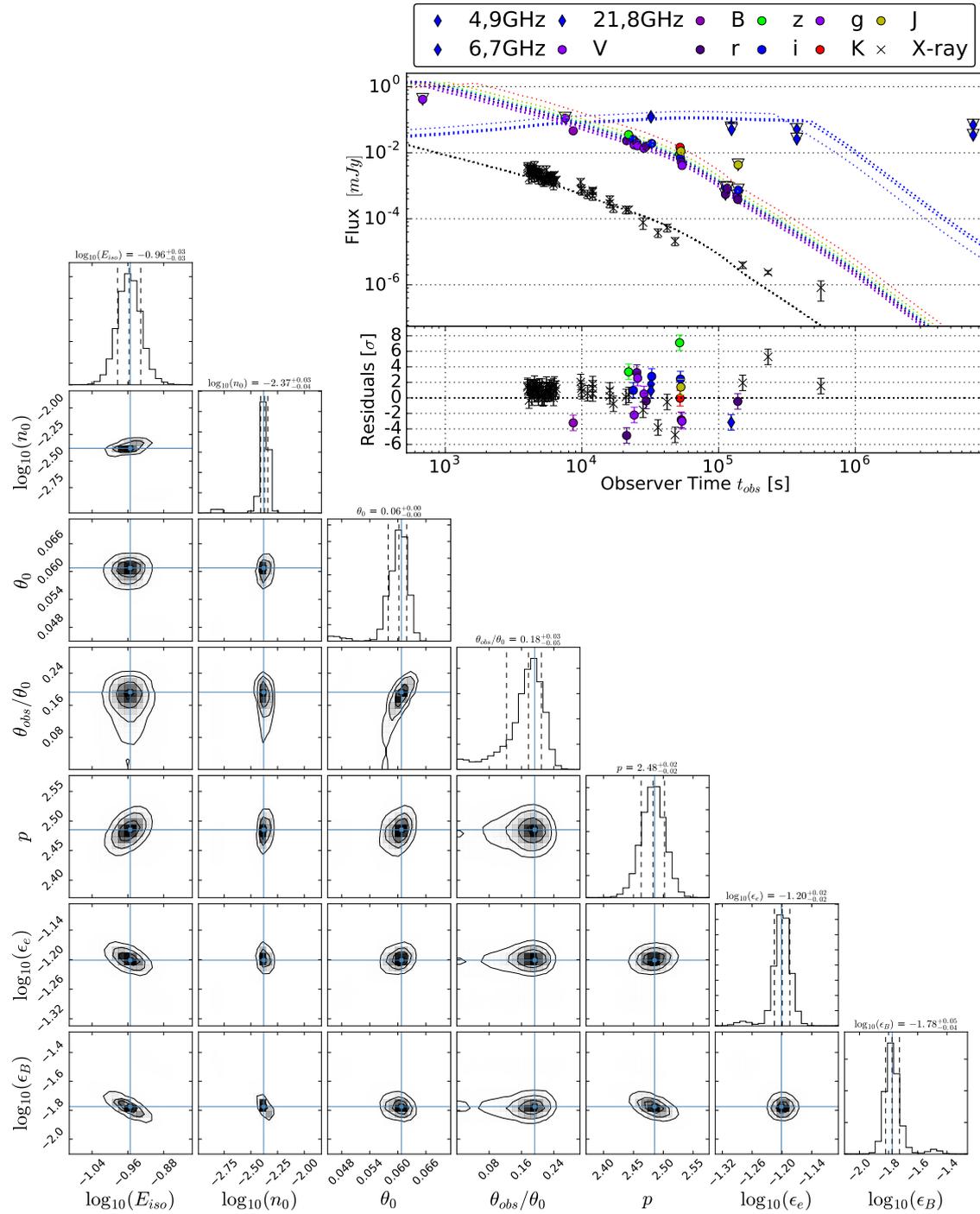
Figure A.29.: Mode II, around $\theta_0 = 0.06$ rad of the PDF of GRB 130603B, with a $\chi^2/\text{DoF} = 4.3$. I additionally corrected for an $A_V^{\text{host}} = 1.2$ mag at a redshift $z = 0.356$. I do consider this a good fit, and θ_0, θ_{obs} and p are constrained.
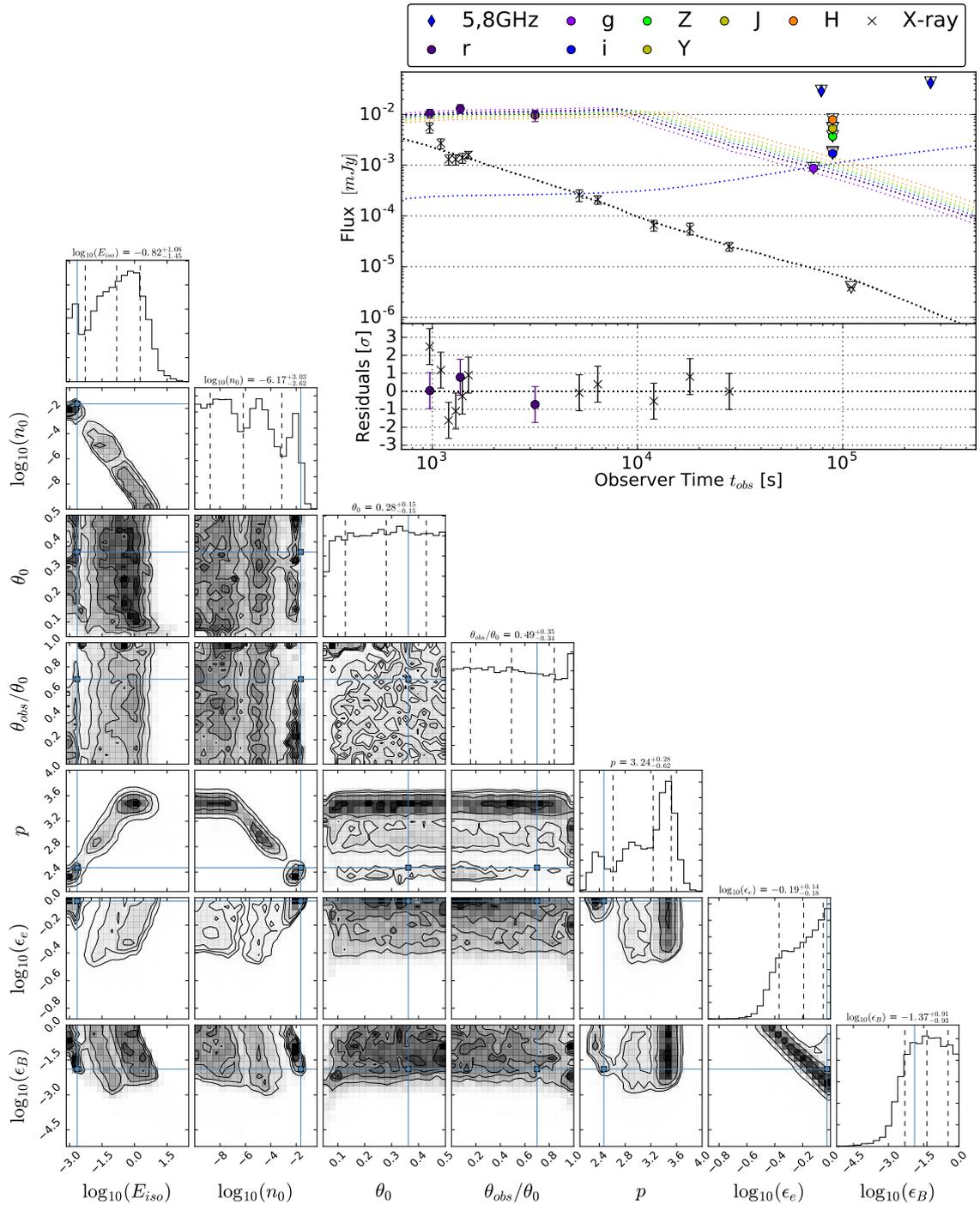
Figure A.30.: Best walker light curve and PDF of GRB 130912A, with a χ^2/DoF = 2.4. The redshift is assumed to be $z = 0.5$. The upper limits have not been part of the fitting process. I want to emphasize the p / E_{iso} plane and p / n_0 plane, where it becomes obvious that a PDF can have a complex form. The used model explains the flat optical light curve before $\sim 10^4$ s with a ν_m crossing. Energy injection may be an alternative explanation, and will be subject of future studies. I consider this a good fit, but θ_0 and θ_{obs} are not constrained.
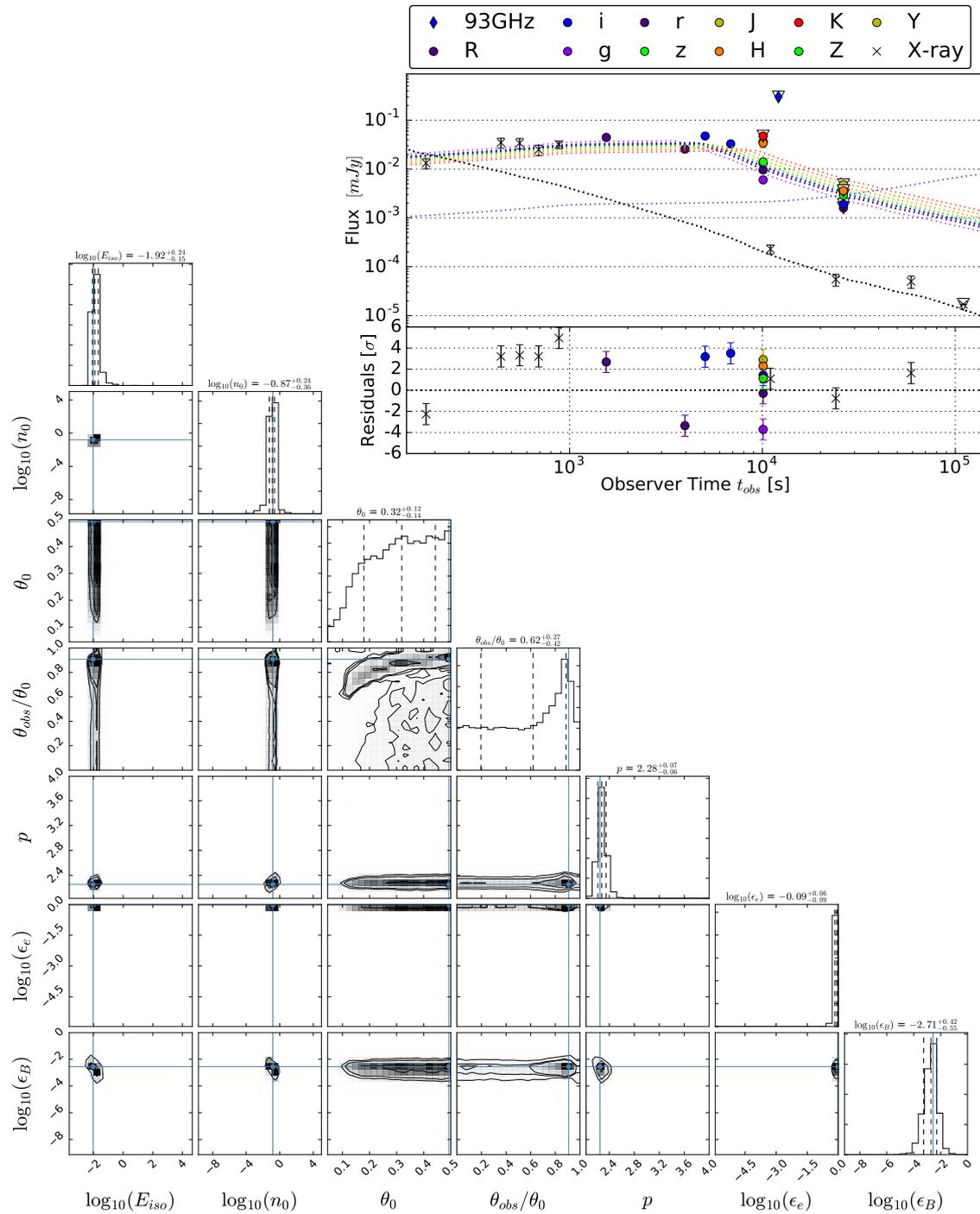
Figure A.31.: Best walker light curve and PDF of GRB 131004, with a $\chi^2/\mathrm{DoF} = 13.7$. The redshift is $z = 0.717$. The upper limits have not been part of the fitting process. The model fails to reproduce the temporal slope of the X-ray before 10^3 s . I do not consider this a good fit.
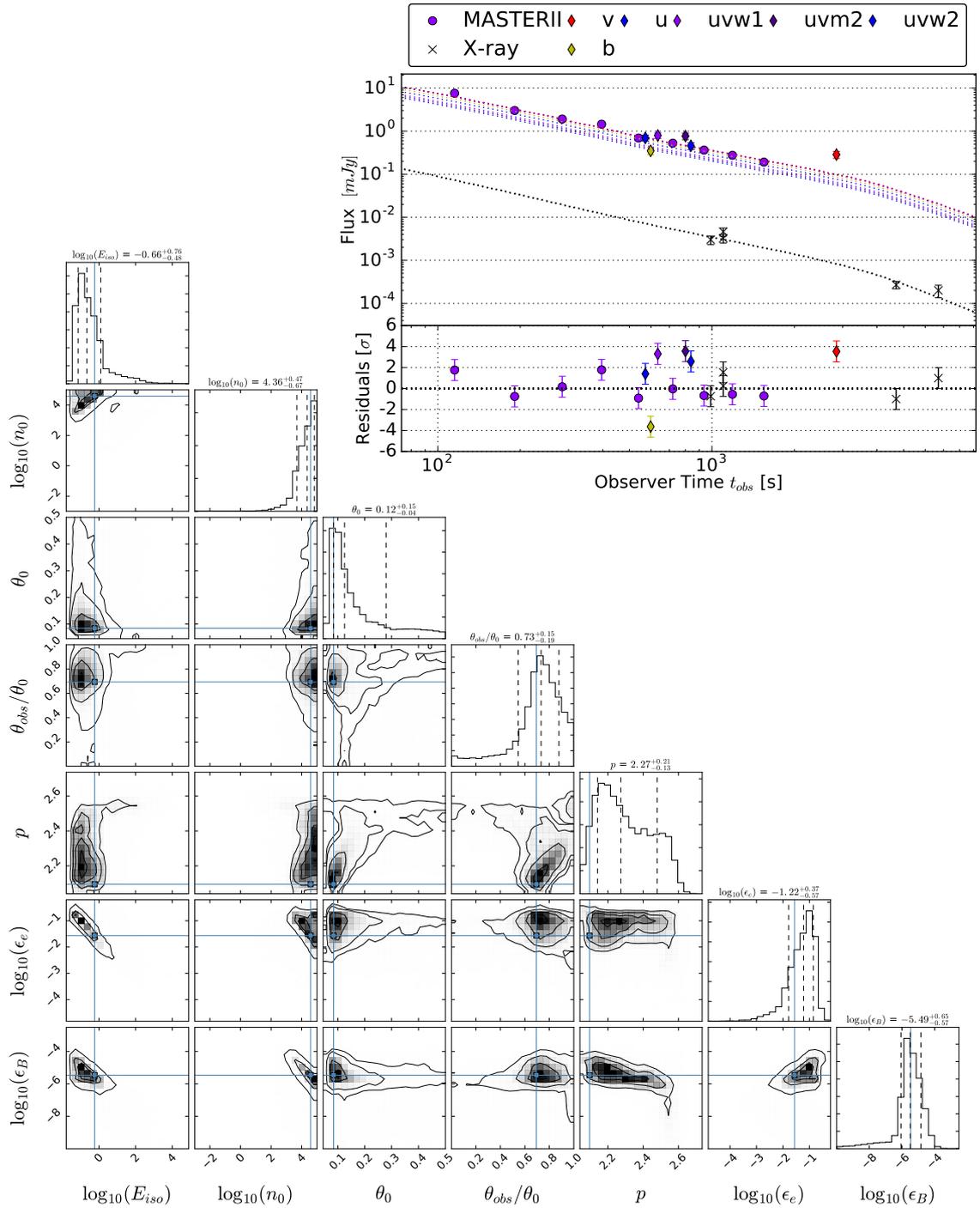
Figure A.32.: Best walker light curve and PDF of GRB 140129B, with a χ^2/DoF = 6.0. The redshift is assumed to be $z = 0.5$. The upper limits have not been part of the fitting process. The MASTER II has a white filter. Additionally to Fong et al. (2015) I include Swift/UVOT data from Swenson & Bernardini (2014), and I corrected them for galactic extinction (Schlegel et al. 1998). I consider this a good fit, and θ_0, θ_{obs} and p are constrained.
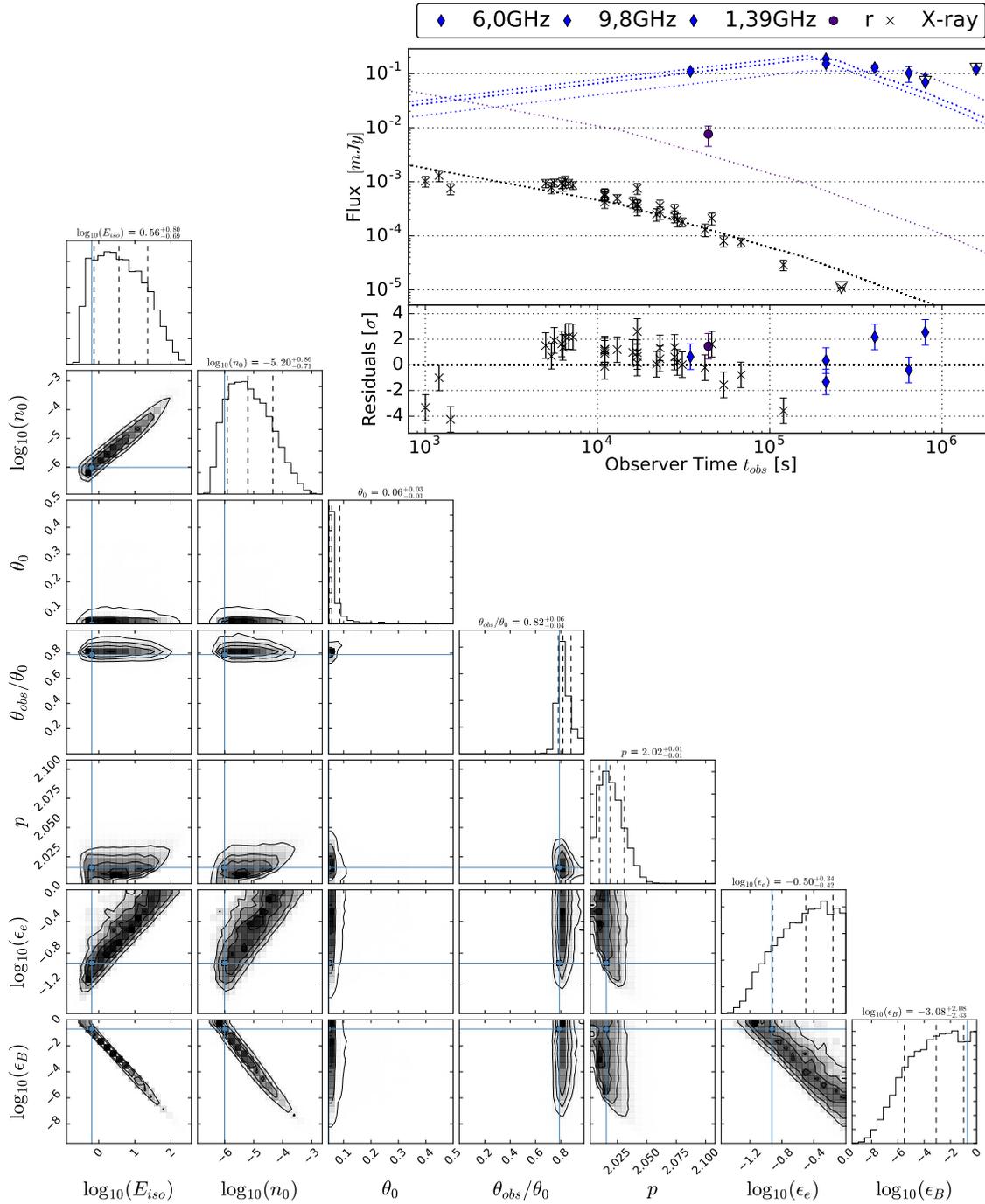
Figure A.33.: Best walker light curve and PDF of GRB 140903A, with a χ^2/DoF = 3.3. The redshift is $z = 0.351$. The upper limits have not been part of the fitting process. I consider this a good fit, and θ_0, θ_obs and p are constrained.
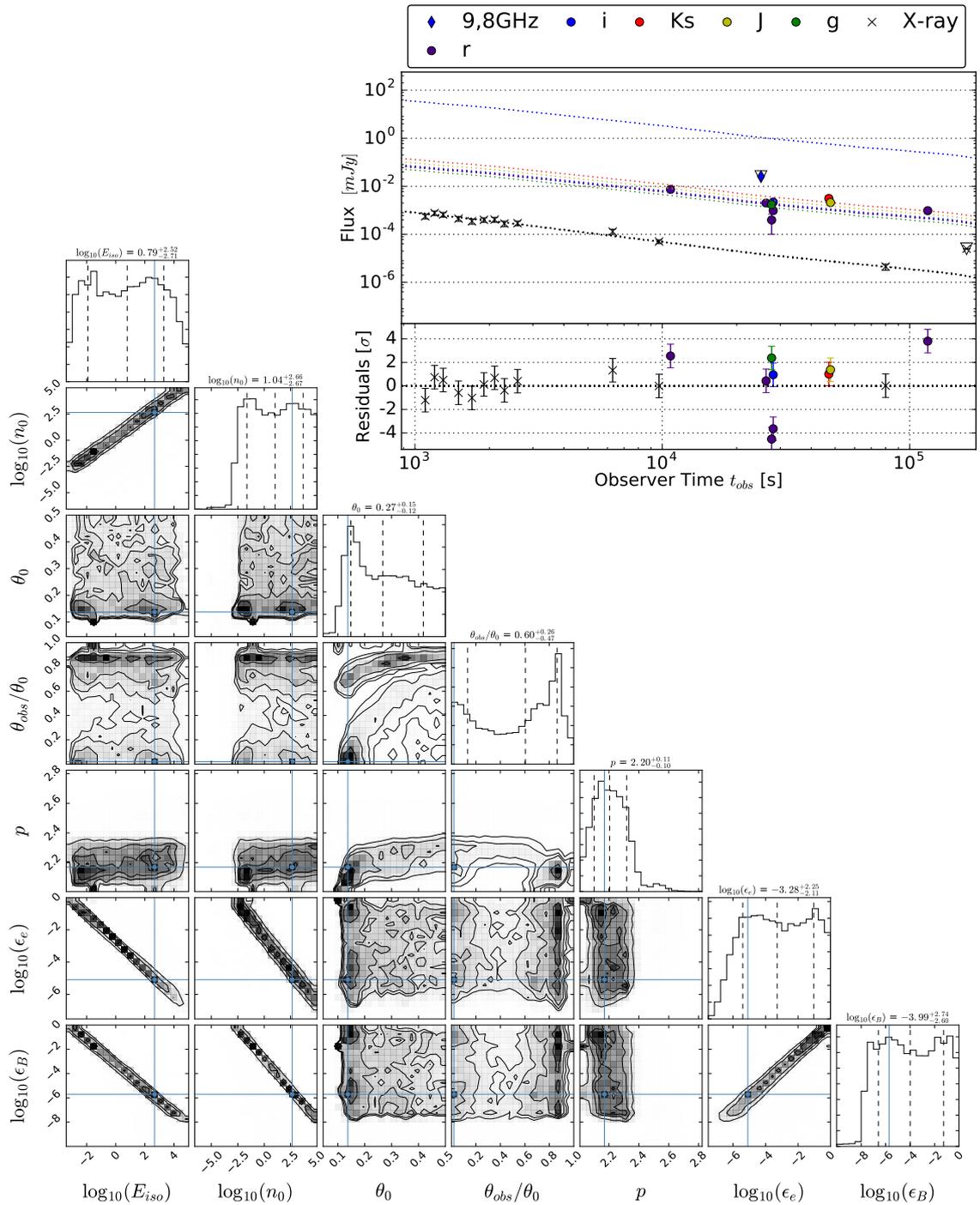
Figure A.34.: Best walker light curve and PDF of GRB 140930B, with a χ^2/DoF = 5.1. The redshift is assumed to be $z = 0.5$. The upper limits have not been part of the fitting process. Additionally to the data from Fong et al. (2015) I include so far unpublished GROND g and r band data. The r data points come from 3 different instruments: ACAM, GROND and MMTCam. The residual of those points are probably due to issues with the cross calibration between them. I consider this a good fit, and θ_0 and θ_{obs} are reasonably constrained.

APPENDIX B

ADDITIONAL DATA FOR CHAPTER 5

Table B.1.: All closure relations that are consistent with the data. The energy injection index q is given where needed.

CR	scenario	spectral regime	p	q
		X-ray before break		
1	ISM, slow cooling	$\nu_m < \nu < \nu_c$	$2.82^{+0.21}_{-0.13}$	0.46 ± 0.10
2	ISM, slow cooling	$\nu > \nu_c$	$1.82^{+0.21}_{-0.13}$	0.71 ± 0.17
4	ISM, fast cooling	$\nu > \nu_m$	$1.82^{+0.21}_{-0.13}$	0.71 ± 0.17
5	wind, slow cooling	$\nu_m < \nu < \nu_c$	$2.82^{+0.21}_{-0.13}$	-0.34 ± 0.12
6	wind, slow cooling	$\nu > \nu_c$	$1.82^{+0.21}_{-0.13}$	-1.39 ± 0.08
8	wind, fast cooling	$\nu > \nu_m$	$1.82^{+0.21}_{-0.13}$	0.71 ± 0.17
9	uniform jet (spreading), slow cooling	$\nu_m < \nu < \nu_c$	$2.82^{+0.21}_{-0.13}$	0.32 ± 0.05
10	uniform jet (spreading), slow cooling	$\nu > \nu_c$	$1.82^{+0.21}_{-0.13}$	-2.08 ± 0.32
11	ISM, uniform jet (nonspreading), slow cooling	$\nu_m < \nu < \nu_c$	$2.82^{+0.21}_{-0.13}$	0.10 ± 0.08
12	ISM, Uniform jet (nonspreading), slow cooling	$\nu > \nu_c$	$1.82^{+0.21}_{-0.13}$	0.14 ± 0.11
13	wind, uniform jet (nonspreading), slow cooling	$\nu_m < \nu < \nu_c$	$2.82^{+0.21}_{-0.13}$	-0.22 ± 0.08
14	wind, uniform jet (nonspreading), slow cooling	$\nu > \nu_c$	$1.82^{+0.21}_{-0.13}$	0.46 ± 0.10
		X-ray after break		
1	ISM, slow cooling	$\nu_m < \nu < \nu_c$	$2.82^{+0.21}_{-0.13}$	-
5	wind, slow cooling	$\nu_m < \nu < \nu_c$	$2.82^{+0.21}_{-0.13}$	-
6	wind, slow cooling	$\nu > \nu_c$	$1.82^{+0.21}_{-0.13}$	-0.26 ± 0.29
9	uniform jet (spreading), slow cooling	$\nu_m < \nu < \nu_c$	$2.82^{+0.21}_{-0.13}$	0.87 ± 0.14
11	ISM, uniform jet (nonspreading), slow cooling	$\nu_m < \nu < \nu_c$	$2.82^{+0.21}_{-0.13}$	0.74 ± 0.17
12	ISM, uniform jet (nonspreading), slow cooling	$\nu > \nu_c$	$1.82^{+0.21}_{-0.13}$	-
13	wind, uniform jet (nonspreading), slow cooling	$\nu_m < \nu < \nu_c$	$2.82^{+0.21}_{-0.13}$	0.52 ± 0.20
14	wind, uniform jet (nonspreading), slow cooling	$\nu > \nu_c$	$1.82^{+0.21}_{-0.13}$	-
		optical before break		
1	ISM, slow cooling	$\nu_m < \nu < \nu_c$	$1.82^{+0.21}_{-0.13}$	0.49 ± 0.11
2	ISM, slow cooling	$\nu > \nu_c$	$0.82^{+0.21}_{-0.13}$	0.84 ± 0.21
3	ISM, fast cooling	$\nu_c < \nu < \nu_m$	na^{+na}_{-na}	0.74 ± 0.08
4	ISM, fast cooling	$\nu > \nu_m$	$0.82^{+0.21}_{-0.13}$	0.84 ± 0.21
5	wind, slow cooling	$\nu_m < \nu < \nu_c$	$1.82^{+0.21}_{-0.13}$	-0.58 ± 0.11
6	wind, slow cooling	$\nu > \nu_c$	$0.82^{+0.21}_{-0.13}$	-2.00 ± 0.01
7	wind, fast cooling	$\nu_c < \nu < \nu_m$	na^{+na}_{-na}	0.58 ± 0.11
8	wind, fast cooling	$\nu > \nu_m$	$0.82^{+0.21}_{-0.13}$	0.84 ± 0.21
9	uniform jet (spreading), slow cooling	$\nu_m < \nu < \nu_c$	$1.82^{+0.21}_{-0.13}$	0.12 ± 0.03
10	uniform jet (spreading), slow cooling	$\nu > \nu_c$	$0.82^{+0.21}_{-0.13}$	-4.00 ± 0.04
11	ISM, uniform jet (nonspreading), slow cooling	$\nu_m < \nu < \nu_c$	$1.82^{+0.21}_{-0.13}$	0.06 ± 0.07
12	ISM, Uniform jet (nonspreading), slow cooling	$\nu > \nu_c$	$0.82^{+0.21}_{-0.13}$	0.10 ± 0.12
13	wind, uniform jet (nonspreading), slow cooling	$\nu_m < \nu < \nu_c$	$1.82^{+0.21}_{-0.13}$	-0.34 ± 0.07
14	wind, uniform jet (nonspreading), slow cooling	$\nu > \nu_c$	$0.82^{+0.21}_{-0.13}$	0.49 ± 0.11
		optical after break		
6	wind, slow cooling	$\nu > \nu_c$	$0.82^{+0.21}_{-0.13}$	0.02 ± 0.16
11	ISM, uniform jet (nonspreading), slow cooling	$\nu_m < \nu < \nu_c$	$1.82^{+0.21}_{-0.13}$	-
13	wind, uniform jet (nonspreading), slow cooling	$\nu_m < \nu < \nu_c$	$1.82^{+0.21}_{-0.13}$	0.84 ± 0.13

Table B.2.: AB magnitudes of comparison stars.
They do not include the systematical errors of the calibration:
$g = 0.03$ mag, $r = 0.03$ mag, $i = 0.04$ mag, $z = 0.04$ mag, $J = 0.05$ mag, $H = 0.05$ mag, $K = 0.07$ mag

#	RA	Dec.	g'	r'	i'	z'	J	H	K_s
I	152.315	-26.628	20.88 ± 0.02	19.96 ± 0.01	19.46 ± 0.01	19.19 ± 0.01	17.72 ± 0.02	17.05 ± 0.03	16.50 ± 0.07
II	152.297	-26.628	22.40 ± 0.06	21.58 ± 0.03	21.26 ± 0.04	21.10 ± 0.05	19.82 ± 0.15	18.98 ± 0.11	na
III	152.299	-26.635	na	21.10 ± 0.01	19.91 ± 0.01	19.39 ± 0.01	18.08 ± 0.03	17.43 ± 0.03	17.25 ± 0.14

Table B.3.: Photometry of GRB 150424A. Upper limits are flagged with "UL"

Time	Time error	mag	mag error	band	instrument
57903	2312	21.76	0.04	g'	GROND
62645	2325	21.90	0.03	g'	GROND
67277	2220	21.99	0.04	g'	GROND
156123	4528	23.32	0.10	g'	GROND
238900	5428	23.6	UL	g'	GROND
323218	2930	24.5	UL	g'	GROND
411767	5450	24.9	UL	g'	GROND
582978	3189	23.4	UL	g'	GROND
670665	5245	23.9	UL	g'	GROND
842737	4961	24.2	UL	g'	GROND
57903	2312	21.55	0.03	r'	GROND
62645	2325	21.60	0.03	r'	GROND
67277	2220	21.80	0.03	r'	GROND
156582	4986	23.08	0.07	r'	GROND
238900	5428	24.4	UL	r'	GROND
323218	2930	23.92	0.22	r'	GROND
411767	5450	25.0	UL	r'	GROND
582978	3189	23.9	UL	r'	GROND
670891	5471	24.1	UL	r'	GROND
842962	5186	24.5	UL	r'	GROND
57903	2312	21.45	0.05	i'	GROND
62645	2325	21.44	0.04	i'	GROND
67374	2316	21.58	0.05	i'	GROND
156582	4986	23.03	0.13	i'	GROND
238900	5428	23.9	UL	i'	GROND
323218	2930	24.1	UL	i'	GROND
411767	5450	24.6	UL	i'	GROND
582978	3189	23.6	UL	i'	GROND
670891	5471	23.8	UL	i'	GROND
842962	5186	24.3	UL	i'	GROND
57903	2312	21.29	0.06	z'	GROND
62645	2325	21.40	0.05	z'	GROND
67374	2316	21.52	0.06	z'	GROND
156355	4760	22.62	0.12	z'	GROND
238900	5428	23.6	UL	z'	GROND

Table B.3.: Continued.

Time	Time error	AB mag	mag error	band	instrument
323218	2930	23.8	UL	z'	GROND
411767	5450	24.4	UL	z'	GROND
582978	3189	23.3	UL	z'	GROND
670891	5471	23.0	UL	z'	GROND
842962	5186	24.0	UL	z'	GROND
57929	2338	20.98	0.19	J	GROND
62670	2351	21.22	0.19	J	GROND
67399	2343	21.38	0.23	J	GROND
156606	5011	22.1	UL	J	GROND
238924	5452	22.0	UL	J	GROND
323331	3043	21.9	UL	J	GROND
411791	5475	22.4	UL	J	GROND
670915	5494	22.1	UL	J	GROND
842987	5211	22.4	UL	J	GROND
156606	5011	21.6	UL	H	GROND
238924	5452	21.6	UL	H	GROND
323331	3043	21.5	UL	H	GROND
411791	5475	22.0	UL	H	GROND
670915	5494	21.6	UL	H	GROND
842987	5211	21.7	UL	H	GROND
156834	5239	20.5	UL	Ks	GROND
238924	5452	20.0	UL	Ks	GROND
323242	2954	19.9	UL	Ks	GROND
411791	5475	20.4	UL	Ks	GROND
670915	5494	20.5	UL	Ks	GROND
843441	5665	20.9	UL	Ks	GROND
436	123	21.3	UL	u	UVOT
2887	108	20.8	UL	u	UVOT
6396	98	20.56	0.23	u	UVOT
3404	329	20.91	0.17	u	UVOT
45591	433	21.3	UL	u	UVOT
99360	305	21.0	UL	u	UVOT
185608	300	20.8	UL	u	UVOT
795276	284	21.3	UL	u	UVOT
1394595	4354	22.1	UL	u	UVOT
664	19	18.9	UL	b	UVOT

Table B.3.: Continued.

Time	Time error	AB mag	mag error	band	instrument
5884	197	20.42	0.25	b	UVOT
3634	216	20.9	UL	b	UVOT
16166	443	20.5	UL	b	UVOT
16166	443	21.0	UL	b	UVOT
129408	590	20.7	UL	b	UVOT
82	5	17.5	UL	v	UVOT
738	19	18.0	UL	v	UVOT
4347	98	19.1	UL	v	UVOT
5782	98	19.6	UL	v	UVOT
3261	216	19.8	UL	v	UVOT
12078	295	19.9	UL	v	UVOT
20295	589	20.1	UL	v	UVOT
34741	442	19.9	UL	v	UVOT
160892	588	19.9	UL	v	UVOT
2773	108	20.9	UL	uvw1	UVOT
17934	329	21.27	0.19	uvw1	UVOT
42244	560	22.2	UL	uvw1	UVOT
92657	358	22.1	UL	uvw1	UVOT
177963	461	21.8	UL	uvw1	UVOT
746677	1086	22.4	UL	uvw1	UVOT
1310529	5447	22.6	UL	uvw1	UVOT
714	19	19.7	UL	uvw2	UVOT
3349	106	21.2	UL	uvw2	UVOT
3146	126	21.9	UL	uvw2	UVOT
11320	443	21.65	0.17	uvw2	UVOT
29251	1618	21.89	0.10	uvw2	UVOT
129298	554	22.6	UL	uvw2	UVOT
215616	640	22.5	UL	uvw2	UVOT
431143	3532	23.1	UL	uvw2	UVOT
1295417	6031	23.2	UL	uvw2	UVOT
762	19	19.1	UL	uvm2	UVOT
5269	197	21.2	UL	uvm2	UVOT
3376	206	21.7	UL	uvm2	UVOT
72406	470	21.9	UL	uvm2	UVOT
173186	1105	22.3	UL	uvm2	UVOT
516450	2747	22.5	UL	uvm2	UVOT

Table B.3.: Continued.

Time	Time error	AB mag	mag error	band	instrument
1224527	5590	22.4	UL	uvm2	UVOT
174	74	21.30	0.23	white	UVOT
601	10	20.7	UL	white	UVOT
890	83	20.94	0.16	white	UVOT
5371	98	20.96	0.15	white	UVOT
8481	418	20.93	0.08	white	UVOT
10563	295	20.87	0.09	white	UVOT
16926	295	21.09	0.10	white	UVOT
32126	1053	21.02	0.06	white	UVOT
292642	1707	22.8	UL	white	UVOT
303903	1184	22.7	UL	white	UVOT
314852	534	22.2	UL	white	UVOT
335542	427	22.3	UL	white	UVOT
358922	1178	22.6	UL	white	UVOT
576743	2047	24.96	0.25	HST125W	HST
800368	2197	25.53	0.26	HST125W	HST
1203117	811	26.01	0.26	HST125W	HST
579662	811	24.73	0.25	HST160W	HST
580609	75	24.55	0.25	HST160W	HST
803437	811	25.26	0.25	HST160W	HST
1206264	2274	25.57	0.26	HST160W	HST
573431	1092	26.03	0.26	HST606W	HST
796906	1092	26.25	0.26	HST606W	HST
5604	180	20.77	0.03	g	LRIS
5616	180	20.66	0.04	R	LRIS

APPENDIX C

CONSTANTS AND UNITS

C.1. Constants

Name	Symbol	CGS units		
		number	exp	unit
speed of light	c	2.99792458	10^{+10}	cm s^{-1}
Planck constant	h	6.6262	10^{-27}	erg s
Thomson cross section	σ_T	6.6524	10^{-25}	cm ^{2}
electron charge	e	4.8032068	10^{-10}	erg$^{1/2}$ cm $^{1/2}$
proton mass	m_p	1.672623	10^{-24}	g
electron mass	m_e	9.1093897	10^{-28}	g
Pi	π	3.14159265		

C.2. Conversions

- $F_\nu[\mu\text{Jy}] = 10^{29 - \frac{M_{AB} + 48.6}{2.5}}$

- $1\text{erg} = 10^{-7}\text{J} = 6.2415 \times 10^{11}\text{eV} = \frac{\text{g cm}^2}{\text{s}^2}$

C.3. Units

- Magnetic field $[B] = G = \frac{g^{1/2}}{\text{cm}^{1/2}\text{s}} = \sqrt{\frac{\text{erg}}{\text{cm}^3}}$

- Moment of Inertia $[I] = \text{g cm}^2$

- Luminosity $[L] = \frac{\text{erg}}{\text{s}}$

- Monochromatic flux $[Jy] = 10^{-23}\frac{\text{erg}}{\text{cm}^2\,\text{s}\,\text{Hz}}$

APPENDIX D

ABBREVIATIONS

AGN Active Galactic Nucleus

BM Blandford McKee

CBM compact binary merger

CGS Centimetre Gram Second

EE Extended Emission

GCN Gamma-ray Coordinates Network

GRB γ-ray burst

GW Gravitational Wave

HST Hubble Space Telescope

IGM Inter Galactic Medium

ISM inter stellar medium

LMC Large Magellanic Cloud

MCMC Monte Carlo Markov Chain

MW Milky Way

PDF Posterior Probability Distribution

SED spectral energy distribution

SMC Small Magellanic Cloud

XRT X-Ray Telescope

APPENDIX E

ACKNOWLEDGMENTS

I would like to thank my supervisor Jochen Greiner for giving me the opportunity to work on this thesis. Thanks Jochen for all the support and advice you gave me over the years!

Next, I want to thank Hendrik Van Eerten for making SCALEFIT available early on, and for all the scientific input and personal guidance he gave. Thanks Hendrik!

I also want to thank Lothar Oberauer for accepting again to be my second reviewer. Thank you Prof. Oberauer!

And of course I want to thank all my working mates from the MPE, the TLS, the CTU or wherever they maybe in the meantime: Julia Bodensteiner, Birgit Boller, Jan Bolmer, Michael Burgess, Janet Chen, Werner Collmar, Corentin Delvaux, Roland Diehl, Jonny Elliot, Robert Filgas, John Graham, Martha Lippich, Alexander Kann, Andreas von Kienlin, Sylvio Klose, Thomas Krühler, Paul Nandra, Ana Nicuesa, Arne Rau, Patricia Schady, Sebastian Schmidl, Tassilo Schweyer, Veronika Schubert, Helmut Steinle, Vlad Sudilovsky, Mohit Tanga, Karla Varela, Chris Wegg, Phil Wiseman, Rob Yates and Xiao-Ling Zhang. Thanks guys, for the company during lunch time, for having my back during remote shifts, for proof reading, your expertise, for laughing and suffering with me...

Many thanks also to all the SAs, DNOs, technicians, secretaries, cooks, maids, cleaning ladies and stewardesses, who made my observing trips, all other travels and daily life much more pleasant.

Auch möchte ich allen Freunden und meiner Familie für ihre Unterstützung danken, besonders meinen Eltern Elke und Albert, meiner Tante Irmi und meinem Onkel Gerd, und natürlich meinen Brüdern Markus und Miki.